

AD-A066 141

AIR FORCE FLIGHT DYNAMICS LAB WRIGHT-PATTERSON AFB OHIO
PREDICTION OF THE ANGULAR RESPONSE POWER SPECTRAL DENSITY OF AI--ETC(U)
DEC 78 J H LEE, M W OBAL, D L BROWN

F/G 1/3

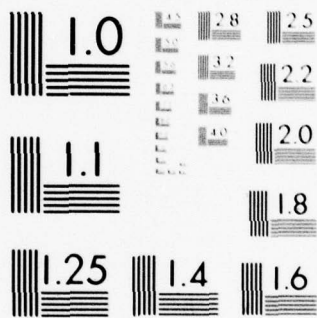
UNCLASSIFIED

AFFDL-TR-78-188

NL

1 OF 2
AD
A066141





MICROCOPY RESOLUTION TEST CHART
NATIONAL BUREAU OF STANDARDS-1963-A

AFFDL-TR-78-188

LEVEL II

2

AD A0 661 41

PREDICTION OF THE ANGULAR RESPONSE POWER SPECTRAL DENSITY OF AIRCRAFT STRUCTURES

*FIELD TEST & EVALUATION BRANCH
STRUCTURAL MECHANICS DIVISION*

DECEMBER 1978

TECHNICAL REPORT AFFDL-TR-78-188
Final Report for Period January 1976 - June 1978

DDC
MAR 21 1979
C

DDC FILE COPY

Approved for public release; distribution unlimited.

AIR FORCE FLIGHT DYNAMICS LABORATORY
AIR FORCE WRIGHT AERONAUTICAL LABORATORIES
AIR FORCE SYSTEMS COMMAND
WRIGHT-PATTERSON AIR FORCE BASE, OHIO 45433

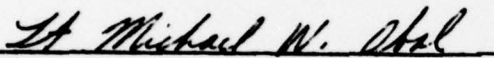
79 03 19 040

NOTICE

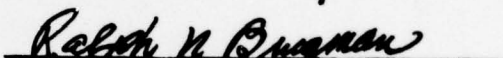
When Government drawings, specifications, or other data are used for any purpose other than in connection with a definitely related Government procurement operation, the United States Government thereby incurs no responsibility nor any obligation whatsoever; and the fact that the government may have formulated, furnished, or in any way supplied the said drawings, specifications, or other data, is not to be regarded by implication or otherwise as in any manner licensing the holder or any other person or corporation, or conveying any rights or permission to manufacture, use, or sell any patented invention that may in any way be related thereto.

This report has been reviewed by the Information Office (OI) and is releasable to the National Technical Information Service (NTIS). At NTIS, it will be available to the general public, including foreign nations.

This technical report has been reviewed and is approved for publication.

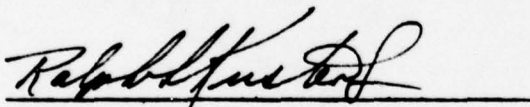


LT MICHAEL W. OBAL
Project Engineer



RALPH N. BINGMAN
Technical Manager

FOR THE COMMANDER



RALPH L. KUSTER, JR., Colonel, USAF
Chief, Structural Mechanics Division

"If your address has changed, if you wish to be removed from our mailing list, or if the addressee is no longer employed by your organization please notify AFFDL-FBR/FBG, W-PAFB, OH 45433 to help us maintain a current mailing list".

Copies of this report should not be returned unless return is required by security considerations, contractual obligations, or notice on a specific document.

UNCLASSIFIED

SECURITY CLASSIFICATION OF THIS PAGE (When Data Entered)

REPORT DOCUMENTATION PAGE		READ INSTRUCTIONS BEFORE COMPLETING FORM
1. REPORT NUMBER 14 AFFDL-TR-78-188	2. GOVT ACCESSION NO.	3. RECIPIENT'S CATALOG NUMBER
4. TITLE (and Subtitle) 6 Prediction of the Angular Response Power Spectral Density of Aircraft Structures.	5. TYPE OF REPORT & PERIOD COVERED 9 Final Report. Jan 1976 - June 1978.	6. PERFORMING ORG. REPORT NUMBER
7. AUTHOR(S) 10 Jon H./Lee, Michael W./Obal Dansen L./Brown	8. CONTRACT OR GRANT NUMBER(S)	
9. PERFORMING ORGANIZATION NAME AND ADDRESS Field Test and Evaluation Branch Air Force Flight Dynamics Laboratory Wright-Patterson Air Force Base, Ohio 45433	10. PROGRAM ELEMENT, PROJECT, TASK AREA & WORK UNIT NUMBERS 16 24010410 17 04	
11. CONTROLLING OFFICE NAME AND ADDRESS Same as above 12 97 p.	12. REPORT DATE 11 Dec 1978	13. NUMBER OF PAGES
14. MONITORING AGENCY NAME & ADDRESS (if different from Controlling Office)	15. SECURITY CLASS. (of this report) UNCLASSIFIED	15a. DECLASSIFICATION DOWNGRADING SCHEDULE
16. DISTRIBUTION STATEMENT (of this Report) Approved for public release; distribution unlimited.		
17. DISTRIBUTION STATEMENT (of the abstract entered in Block 20, if different from Report)		
18. SUPPLEMENTARY NOTES		
19. KEY WORDS (Continue on reverse side if necessary and identify by block number) Aircraft Angular Vibration Nastran Vibration Simulation Angular Vibration Prediction Aircraft Vibration Flight Tests Random Vibration		
20. ABSTRACT (Continue on reverse side if necessary and identify by block number) The design of airborne electro-optical systems requires the knowledge of angular vibration as well as linear vibration of aircraft structures. Rather than predicting the angular vibration subject to aerodynamic and acoustic excitations, an attempt is made here to relate the angular vibration directly to the linear vibration response. With the Bernoulli-Euler beam used as a theoretical model, a relationship has been derived between the linear and angular vibration power spectral density functions. Based on this relationship		

UNCLASSIFIED

SECURITY CLASSIFICATION OF THIS PAGE(When Data Entered)

together with the angular root-mean-squared vibration amplitude as previously predicted by Lee and Whaley (AFFDL-TR-76-56, AF Flight Dynamics Laboratory, Wright-Patterson AFB, Ohio), it is now possible to predict the angular power spectral density and a length scale associated with the angular measurement technique. Tested on the typical flight test data of RF-4C and F-15 fighters, CH-3E helicopter, and B-52 bomber, the predicted angular power spectral density lies within a ± 10 db band about the measurement. Though crude, such a prediction is useful in the preliminary design stage in that one can quickly estimate the angular vibration environment prior to fabrication. 

within

$\pm n -$

UNCLASSIFIED

SECURITY CLASSIFICATION OF THIS PAGE(When Data Entered)

FOREWORD

This work was performed by personnel of the Analysis and Optimization Branch (AFFDL/FBR) and the Field Test and Evaluation Branch (AFFDL/FBG) of the Structural Mechanics Division, Air Force Flight Dynamics Laboratory, Wright-Patterson Air Force Base, Ohio. This study was conducted in support of Project 2401, "Structural Mechanics," Task 240104, "Vibration Prediction and Control, Measurement and Analysis," Work Unit 24010410 "Aircraft Linear and Angular Vibration Prediction."

The research described in this report was conducted by Lt Michael Obal, responsible officer, Dr. Jon Lee and Dansen L. Brown, over the period of January 1976 to June 1978.

This report was submitted by the authors during August 1978.

ACCESSION for	
NTIS	Wire Section <input checked="" type="checkbox"/>
DDC	Buf Section <input type="checkbox"/>
UNCLASSIFIED	
CLASSIFICATION	
BY	
DISPATCH/TITLE/AN	ADVISORY INDEX
DI	SPECIAL
A	

TABLE OF CONTENTS

SECTION		Page
I	INTRODUCTION	1
II	THEORETICAL ANALYSIS	5
	1. Linear and Angular Response PSDs	5
	2. Relationship Between the Linear and Angular Response PSDs	9
	3. Power-Form Representation of the Angular PSD	12
III	BEAM EXPERIMENT	13
IV	AIRCRAFT FLIGHT TEST DATA	15
V	OVERALL ASSESSMENT OF THE PREDICTION SCHEME	23
	REFERENCES	25
APPENDIX A	BEAM EXPERIMENT	38
	REFERENCES	75
APPENDIX B	THE DETERMINATION OF STRUCTURAL DAMPING CONSTANTS	76
APPENDIX C	THE NASTRAN FINITE-ELEMENT COMPUTER PROGRAM	79

PRECEDING PAGE BLANK

79 03 19 040

LIST OF ILLUSTRATIONS

<u>Figure No.</u>	<u>Title</u>	<u>Page</u>
1	Numerical Computation of Σ $E = 10^7 \text{ lb/in}^2$, $I = 1.855 \text{ in}^4$, $\rho = 0.131 \text{ lb/in}^3$ $A = 1.244 \text{ in}^2$, $L = 72 \text{ in}$, $\beta = \omega_1/20$	27
2a	Linear Power Spectral Density of the Test Beam at $X_1 = 25 \text{ in}$.	28
2b	Angular Power Spectral Density of the Test Beam at $X_1 = 25 \text{ in}$. and $X_2 = 29 \text{ in}$.	29
3a	Linear Power Spectral Density of the RF-4C Flight Test (Vertical)	30
3b	Angular Power Spectral Density of the RF-4C Flight Test (Pitch)	31
4a	Linear Power Spectral Density of the F-15 Flight Test (Lateral)	32
4b	Angular Power Spectral Density of the F-15 Flight Test (Roll)	33
5a	Linear Power Spectral Density of the CH-3E Flight Test (Lateral)	34
5b	Angular Power Spectral Density of the CH-3E Flight Test (Yaw)	35
6a	Linear Power Spectral Density of the B-52 Flight Test (Vertical)	36
6b	Angular Power Spectral Density of the B-52 Flight Test (Pitch)	37

<u>Figure No.</u>	<u>Title</u>	<u>Page</u>
A1	Beam Experimental Configuration	53
A2	Controlled Response Acceleration Power Spectral Density at the Midspan of the Test Beam	54
A3	Schematic of Instrumentation Setup	55
A4	Accelerometer and NASTRAN Model Node Locations	56
A5	Typical Forcing Power Spectral Density of the NASTRAN Model at the Midspan of the Beam	57
A6	Response Acceleration Power Spectral Density at the Midspan of the Beam	58
A7a	Linear Power Spectral Density of Test No. 1	59
A7b	Angular Power Spectral Density of Test No. 1, $\Delta X = 4$ in., $X_C = 19$ in.	60
A8a	Linear Power Spectral Density of Test No. 2	61
A8b	Angular Power Spectral Density of Test No. 2, $\Delta X = 4$ in., $X_C = 27$ in.	62
A8c	Angular Power Spectral Density of Test No. 3, $\Delta X = 6$ in., $X_C = 27$ in.	63
A8d	Angular Power Spectral Density of Test No. 4, $\Delta X = 8$ in., $X_C = 27$ in.	64
A8e	Angular Power Spectral Density of Test No. 5, $\Delta X = 10$ in., $X_C = 27$ in.	65
A8f	Angular Power Spectral Density of Test No. 6, $\Delta X = 12$ in., $X_C = 27$ in.	66
A9a	Linear Power Spectral Density of Test No. 7	67
A9b	Angular Power Spectral Density of Test No. 7, $\Delta X = 4$ in., $X_C = 32$ in.	68

<u>Figure No.</u>	<u>Title</u>	<u>Page</u>
A10a	Linear Power Spectral Density of Test No. 8	69
A10b	Angular Power Spectral Density of Test No. 8, $\Delta X = 4$ in., $X_C = 36$ in.	70
A11a	Linear Power Spectral Density of Test No. 9	71
A11b	Angular Power Spectral Density of Test No. 9, $\Delta X = 4$ in., $X_C = 50$ in.	72
A12	Digitally Differenced Angular Power Spectral Density of Test No. 2	73
A13	Comparison of Measured and NASTRAN Linear and Angular RMS Values	74
B1	Transfer Function Magnitude About the 2nd Mode of the Test I-Beam	77

LIST OF TABLES

TABLE	Page
1. Comparison of the Measured and Predicted Angular Vibration PSDs	19
A1. Summary of Test Results	44
A2. The Linear and Angular Vibration RMS Values	51
B1. Viscous Damping Coefficients	76
C1. Executive Control for Format 11, 0	80
C2. Input/Output Control	81
C3. Beam Model Parameters	82
C4. Forcing PSD Function Input	83
C5. Comparison of the NASTRAN and Experimental Resonance Frequencies	84

LIST OF SYMBOLS

A	Cross sectional area
C	Constant defined in Equation (21)
c_1	Constant factor of the accelerometer noise power spectral density
D	Constant factor of the linear response power spectral density
E	Modulus of elasticity
$e_i(t), e(t)$	Noise
F_1, F_2	Lower and upper frequency limits
$f(x,t)$	Excitation force per unit mass of the beam
f	Frequency
f_n	Resonance frequency of the n-th mode
f^*	High frequency limit
$g(t)$	Temporal part of $f(x,t)$
$G_{gg}(\omega)$	Power spectral density of the random process $g(t)$
$G_{\theta_{\Delta} \theta_{\Delta}}(f)$	Reference angular power spectral density
$H_n(\omega)$	Modal frequency-response
$h_n(t)$	Modal impulse-response
I	Moment of inertia
I_{nk}	Defined by Equation (11)
K	Constant defined in Equation (13)
k	Power exponent
L	Beam length
$q(x)$	Spatial part of $f(x,t)$
q_n	Modal coefficients of $q(x)$

$R_{gg}(\tau)$	Correlation of the random process $g(t)$
S/N	Signal-to-noise ratio
t	Time
x	Spatial coordinate
x_c	Center location
$y(x,t)$	Transverse displacement
$y_i(t)$	Transverse displacement at x_i
y_n	Modal coefficients of $y(x,t)$
< >	Statistical average

Greeks

β	Viscous damping constant
Δx	Separation distance
δ_{nk}	Kronecker delta
$\theta(x,t)$	Angular deflection
$\theta_{\Delta}(t)$	Discrete angular deflection
ρ	Beam density
Σ	The curly bracket { } term in Equation (19)
τ	Difference time
ω	Radian frequency
ω_n	Resonance radian frequency of the n-th mode

Subscripts

rms	Root-mean-squared amplitude averaged over the beam
n, k	Modal index

1, 2 Accelerometer No. 1 and No. 2

Superscripts

^ True value
 ℓ Low frequency range
h High frequency range

SECTION I

INTRODUCTION

The design of airborne electro-optical systems requires the knowledge of angular vibration as well as linear vibration of aircraft structures. Just as the linear vibration involves displacements in three coordinate axes, the angular vibration addresses itself to the rotary mode of internal bending about each of the three axes. In one dimension, for instance, if linear vibration refers to the transverse deflection, the pitching motion expressed by the local slope of linear (transverse) displacement would represent the corresponding angular vibration. Theoretically, it is possible to formulate the angular vibratory response of aircraft structures subject to aerodynamic and acoustic random excitations. Although modern computer structural analyses such as the NASTRAN may be implemented, they are at present limited to the low frequency range of vibration of, particularly, a complex structure. To cope with the high frequency range vibration, it is expedient to relate the angular vibration directly to the linear vibration response. This was the approach of Reference 1. Using the Bernoulli-Euler beam as a theoretical model, a simple qualitative relationship was obtained between the linear root-mean-squared (rms) amplitude y_{rms} and angular rms amplitude θ_{rms} (Equation (27) in Reference 1)

$$\theta_{rms} = 1.17 (\pi/L) y_{rms}, \quad (1)$$

where L is the beam length. An alternate relation was also derived in terms of the discrete angular deflection which is defined by the ratio of the difference of transverse displacements $y_2(t)$ and $y_1(t)$ at x_2 and x_1 , respectively, to the separation distance $\Delta x = x_2 - x_1$; namely

$$\theta_{\Delta}(t) = [y_2(t) - y_1(t)] / \Delta x. \quad (2)$$

Here the y's are measured by using accelerometers. The use of the discrete or differential angle $\theta_{\Delta}(t)$ is dictated by the practical requirement that at present there is no inexpensive off-the-shelf type angular deflection transducer with sufficiently high frequency response. By a parallel derivation, the relationship involving $(\theta_{\Delta})_{rms}$ and y_{rms} which is counterpart to (1) becomes

$$(\theta_{\Delta})_{rms} = (\sqrt{2} / \Delta x) y_{rms}. \quad (3)$$

It must be pointed out that relations (1) and (3) are independent of the local coordinates and end conditions. Note that relation (3) depends only on the separation distance. This came about because θ_{rms} and $(\theta_{\Delta})_{rms}$ and y_{rms} are the rms amplitudes averaged over the beam. The beam-averaging originally introduced in Reference 1 is based on the assumption that response statistics should not vary significantly from one point to another on a complex structure under the temporally and spatially homogeneous random excitations. The consequence of beam-averaging is the loss of detailed spatial information. This then enables us to apply the linear-angular rms amplitude relations, (1) and (3), to any structures as a qualitative relation, provided L or Δx can be specified depending on the type of angular measurement technique employed.

Based on limited vibration data available at the writing of Reference 1, it was concluded that by relations (1) and (3) the angular rms value can be predicted within $\pm 20\%$ of the measurement. Since then, some more linear

and angular vibration data have been obtained from the flight tests of RF-4C and F-15 fighters, CH-3E helicopter, and B-52 bomber (References 2 - 5). This therefore enables us to re-evaluate the prediction capability of relations (1) and (3) in light of the additional vibration test data. Moreover, it is now possible to move a step further and predict the spectral shape of the angular power spectral density (psd) function, which is the main objective of this report.

Following the same line of arguments as in Reference 1, a general relationship has been derived between the linear and angular response psd's, which states that the linear psd falls off faster than the angular by the power exponent of one (Section II). This linear-angular psd relation was first tested on a simply supported beam excited randomly at the midspan in such a manner that the acceleration response psd was constant over 40 - 3200 Hz. Consequently, the linear displacement psd has the power-form of f^{-4} . It was then found that the angular psd obeys the power-form of f^{-3} , as predicted, over the same frequency range (Section III).

Encouraged by the success on test beam, an attempt was made to predict the spectral shape and magnitude level of the angular psd of typical flight tests of RF-4C and F-15 fighters, CH-3E helicopter, and B-52 bomber (Section IV). After splitting the linear vibration psd into the low and high frequency ranges, the angular vibration psd has been predicted in two separate frequency ranges. First, the spectral shape of angular psd's can be predicted accurately in the high frequency range for all test cases, but not always so in the low frequency range. Second, an accurate prediction of the magnitude level is difficult to attain in that it requires the correct spectral shape and rms

amplitude of angular vibration. Nevertheless, as an overall performance it was found that the predicted angular psd lies within a ± 10 db band about the measurement for all test cases (Section V). Though crude, such a prediction is useful in the preliminary design stage of electro-optical systems, whereby one can quickly estimate the angular vibration environment based on the linear vibration psd and a length scale associated with the angular measurement technique.

SECTION II

THEORETICAL ANALYSIS

We shall derive in this section a simple relationship between the linear and angular psd's which is counterpart to the rms amplitude relation (1). Although, as in Reference 1, the Bernoulli-Euler beam will be used as a theoretical model, it turns out that the psd relationship derived here is applicable to actual flight test data (Section IV).

We begin with the Bernoulli-Euler beam equation

$$\frac{\partial^2 y}{\partial t^2} + 2\beta \frac{\partial y}{\partial t} + \frac{EI}{\rho A} \frac{\partial^4 y}{\partial x^4} = f(x,t), \quad (4)$$

where ρA is the mass per unit length of the beam, β is the viscous damping constant, EI is the flexural rigidity, and $f(x,t)$ is the excitation force per unit mass of the beam. To facilitate the analysis, split the forcing function into the spatial part ($q(x)$) and temporal part ($g(t)$);

$$f(x, t) = q(x) g(t). \quad (5)$$

The stochastic dynamics of the beam can be formulated based on Equations (4) and (5) (References 6 and 7); the appropriate extension to angular vibration has been carried out in Reference 1.

1. Linear and Angular Response PSD's

Theoretically, it is convenient to consider the simply supported beam of length L because the undamped normal modes are $\sin(n\pi x/L)$. On the other

hand, a simply supported beam is not as experimentally easy to simulate as ones with fixed and free end conditions. In any event, the simply supported end condition is inconsequential because it turns out that the predicted spectral shape of angular psd is independent of a particular end condition within the present formulation. The spatial behavior of $y(x,t)$ and $q(x)$ can be expressed by the normal modes

$$y(x,t) = \sum_{n=1}^{\infty} y_n(t) \sin(n\pi x/L), \quad q(x) = \sum_{n=1}^{\infty} q_n \sin(n\pi x/L). \quad (6)$$

The solution of $y_n(t)$ will be obtained in terms of the modal impulse-response

$$h_n(t) = [(\exp(-\beta t) / \sqrt{\omega_n^2 - \beta^2}) \sin(t \sqrt{\omega_n^2 - \beta^2})], \text{ where}$$

$$\omega_n^2 = (n\pi/L)^4 EI/\rho A. \quad (7)$$

The transverse deflection subject to the zero initial displacement and velocity is

$$y(x,t) = \sum_{n=1}^{\infty} \sin(n\pi x/L) q_n \int_0^t h_n(\tau) g(t-\tau) d\tau. \quad (8)$$

For a small amplitude vibration, the angular deflection may be approximated by the local derivative; $\theta(x,t) = dy/dx$,

$$\theta(x,t) = (\pi/L) \sum_{n=1}^{\infty} n \cos(n\pi x/L) q_n \int_0^t h_n(\tau) g(t-\tau) d\tau. \quad (9)$$

Under the assumption that $g(t)$ and $q(x)$ are statistically independent and that $g(t)$ is a stationary process, the variances of y and θ are (Equations (10) and (12) in Reference 1)

$$\left. \begin{aligned} \langle y^2(x) \rangle &= \sum_{n,k=1}^{\infty} \sin(n\pi x/L) \sin(k\pi x/L) \langle q_n q_k \rangle I_{nk} \\ \langle \theta^2(x) \rangle &= (\pi/L)^2 \sum_{n,k=1}^{\infty} nk \cos(n\pi x/L) \cos(k\pi x/L) \langle q_n q_k \rangle I_{nk} \end{aligned} \right\} (10)$$

where $\langle \quad \rangle$ denotes statistical average. The I_{nk} reflects both the system characteristics and excitation force

$$I_{nk} = (1/4\pi) \int_{-\infty}^{\infty} H_n(\omega) H_k^*(\omega) G_{gg}(\omega) d\omega, \quad (11)$$

where $H_n(\omega) = (\omega_n^2 - \omega^2 + i2B\omega)^{-1}$ is the modal frequency response, and $*$ denotes the complex conjugate. Further, $G_{gg}(\omega)$ is the forcing psd related to the correlation $R_{gg}(\tau) = \langle g(t + \tau)g(t) \rangle$ by the Fourier transform pair;

$$\left. \begin{aligned} R_{gg}(\tau) &= (1/4\pi) \int_{-\infty}^{\infty} G_{gg}(\omega) \exp(i\omega\tau) d\omega, \\ G_{gg}(\omega) &= 2 \int_{-\infty}^{\infty} R_{gg}(\tau) \exp(-i\omega\tau) d\tau. \end{aligned} \right\} (12)$$

The factor $(4\pi)^{-1}$ ensures that $R_{gg}(0) = \int_0^{\infty} G_{gg}(f) df$ with the substitution of $\omega = 2\pi f$. That is, the variance is the sum of spectral energies of a one-sided psd (Reference 8).

When the beam is assumed to be excited by the spatially random $q(x)$

with a Dirac-delta spatial correlation, Equation (10) becomes simplified greatly because of

$$\langle q_n q_k \rangle = K \delta_{nk}, \quad (13)$$

where K is a constant, and $\delta_{nk} = 1$ if $n = k$ and $= 0$ if $n \neq k$. It has been shown in Reference 1 that Equation (13) is approximately valid under the localized forcing of a slightly damped structure. As a consequence of Equation (13), Equation (10) reduces to a single sum

$$\left. \begin{aligned} \langle y^2(x) \rangle &= \sum_{n=1}^{\infty} \sin^2(n\pi x/L) K I_{nn}, \\ \langle \theta^2(x) \rangle &= (\pi/L)^2 \sum_{n=1}^{\infty} n^2 \cos^2(n\pi x/L) K I_{nn}. \end{aligned} \right\} (14)$$

Let us now express the variances in the spectral form

$$\langle y^2(x) \rangle = (1/4\pi) \int_{-\infty}^{\infty} G_{yy}(x, \omega) d\omega, \quad \langle \theta^2(x) \rangle = (1/4\pi) \int_{-\infty}^{\infty} G_{\theta\theta}(x, \omega) d\omega, \quad (15)$$

which are defined analogous to Equation (12). Inserting Equation (15) and $I_{nn} = (1/4\pi) \int_{-\infty}^{\infty} |H_n(\omega)|^2 G_{gg}(\omega) d\omega$ into Equation (14), one obtains by equating the integrands

$$\left. \begin{aligned} G_{yy}(x, \omega) &= \sum_{n=1}^{\infty} \sin^2(n\pi x/L) |H_n(\omega)|^2 K G_{gg}(\omega), \\ G_{\theta\theta}(x, \omega) &= (\pi/L)^2 \sum_{n=1}^{\infty} n^2 \cos^2(n\pi x/L) |H_n(\omega)|^2 K G_{gg}(\omega). \end{aligned} \right\} (16)$$

They are the linear and angular response psd's subject to the arbitrary but stationary forcing psd.

2. Relationship Between the Linear and Angular Response PSD's

To obtain the overall form of psd which is independent of the particular end condition (and hence the mode shape), Equation (16) will be averaged over the beam (Reference 1). Denoting the beam-averaged psd's by $G_{yy}(\omega) = L^{-1} \int_0^L G_{yy}(x, \omega) dx$ and $G_{\theta\theta}(\omega) = L^{-1} \int_0^L G_{\theta\theta}(x, \omega) dx$, Equation (16) gives rise to

$$\left. \begin{aligned} G_{yy}(\omega) &= \sum_{n=1}^{\infty} |H_n(\omega)|^2 (K/2) G_{gg}(\omega), \\ G_{\theta\theta}(\omega) &= (\pi/L)^2 \sum_{n=1}^{\infty} n^2 |H_n(\omega)|^2 (K/2) G_{gg}(\omega), \end{aligned} \right\} (17)$$

with the use of $L^{-1} \int_0^L \sin^2(n\pi x/L) dx = L^{-1} \int_0^L \cos^2(n\pi x/L) dx = 1/2$. By taking the ratio of Equation (17), we find that $G_{\theta\theta}(\omega)/G_{yy}(\omega)$ is independent of the forcing psd

$$\frac{G_{\theta\theta}(\omega)}{G_{yy}(\omega)} = (\pi/L)^2 \frac{\sum_{n=1}^{\infty} n^2 |H_n(\omega)|^2}{\sum_{n=1}^{\infty} |H_n(\omega)|^2}. \quad (18)$$

The analytical behavior of Equation (18) can be determined as follows;

We have $\omega_n = n^2 \omega_1$ from Equation (7). Therefore, inserting $n^2 = \omega_n / \omega_1$ into Equation (18) and writing out the summations in detail result in

$$\frac{G_{\theta\theta}(\omega)}{G_{yy}(\omega)} = (\pi/L)^2 (1/\omega_1) \left\{ \frac{\omega_1 |H_1(\omega)|^2 + \omega_2 |H_2(\omega)|^2 + \omega_3 |H_3(\omega)|^2 + \dots}{|H_1(\omega)|^2 + |H_2(\omega)|^2 + |H_3(\omega)|^2 + \dots} \right\}$$

(19)

Note that the dominant contribution of $|H_n(\omega)|^2 = [(\omega_n^2 - \omega^2)^2 + 4\beta^2 \omega^2]^{-1}$ is in a resonance frequency band around $\omega = \omega_n$. Therefore, when $\omega = \omega_1$ the curly bracket { } term of Equation (19) denoted by Σ is approximately equal to $\omega_1 |H_1(\omega)|^2 / |H_1(\omega)|^2 = \omega_1$. Similarly, for $\omega = \omega_2$ we have $\Sigma = \omega_2$, and in general $\Sigma = \omega_n$ for $\omega = \omega_n$. Hence, the loci of local maxima of Σ increase linearly as ω passes through the successive resonance frequencies. Since the density of resonance frequencies per octave frequency decade increases very rapidly, $\Sigma = \omega$ is a good approximation in the high frequency range as substantiated by the numerical computation of Figure 1. Using this approximation, Equation (19) in terms of the frequency becomes

$$G_{\theta\theta}(f)/G_{yy}(f) = (\pi^2/L^2 f_1) f, \quad (20)^*$$

which is the desired relationship between the linear and angular response psd's. The ratio $G_{\theta\theta}(f)/G_{yy}(f)$ consists of two parts, the scaling factor $(\pi^2/L^2 f_1)$ and the spectral shape in the power-form of f . Note that the scaling factor reflects the particular end condition and beam properties through the primary frequency f_1 . On the other hand, the spectral shape function is universal since it is completely independent of the end condition. This is, perhaps, not surprising because the frequency relation (7) is asymptotically valid for large n under different end conditions (Reference 9). Due to similarity in the modal formulations of beam and plate, one may expect the same shape function to be valid on a plate regardless of the boundary conditions. As a matter of fact, something more is possible. It will be shown in Section IV that the spectral shape relation is applicable to the high frequency part of the linear and angular psd's of typical aircraft flight test data.

Footnote *) A similar attempt has been made to predict the spectral shape of $G_{\theta\theta}(f)/G_{yy}(f)$ in Reference 10. However, there is a noticeable difference in the final results. Namely, Equation (7) of Reference 10 which is the counterpart of Equation (18) can be put in the form

$$G_{\theta\theta}(\omega)/G_{yy}(\omega) = (\pi/L)^2 \left| \sum_{n=1}^{\infty} n H_n(\omega) \sin(n\pi/2) \right|^2 / \left| \sum_{n=1}^{\infty} H_n(\omega) \sin(n\pi/2) \right|^2. \quad (+)$$

The derivation of Equation (+) is not justified. Apart from the factor $\sin(n\pi/2)$ which picks out only the odd terms in the summations, Equation (+) involves the sums of the complex H_n , whereas Equation (18) sums up the real $|H_n|$. The overall difference shows up when one compares Figure 1 with Figure 3 of Reference 10, which increases steadily with a slope of about $3/4$ up to 700 Hz and then falls off abruptly thereafter.

3. Power-Form Representation of the Angular PSD

Let us suppose that the linear psd has a simple power-form expression $G_{yy}(f) = Df^{-k}$, where D is a constant and k is the power exponent in the frequency range (F_1, F_2) . In view of Equation (20), the angular psd would then have the form

$$G_{\theta\theta}(f) = C f^{-k+1}, \quad (21)$$

where $C = (\pi^2/L^2 f_1^2)D$. For the aircraft application, it is difficult to estimate the constant factor C . This is because we do not know a priori the primary frequency of a locally dominant mode at the arbitrary aircraft location. For this reason, we shall propose an indirect means of determining the constant factor by way of the angular vibration amplitude predicted by Equations (1) and (3). Deviating from the original context (Reference 1), let us assume that relations (1) and (3) can be applied to the rms values computed over a frequency band as well as the entire frequency range. Then, by requiring the predicted θ_{rms}^2 over the frequency band of (F_1, F_2) be identical to $\int_{F_1}^{F_2} 2 G_{\theta\theta}(f) df$, we obtain

$$C = \frac{(2 - k) \theta_{rms}^2}{F_1^{-k+2} - F_2^{-k+2}}. \quad (22)$$

Equation (21) together with constant (22) represents a power-form representation in (F_1, F_2) , based on the power exponent k and the angular θ_{rms} predicted by the procedures of Reference 1.

SECTION III

BEAM EXPERIMENT

To verify Equation (21) on the very beam model that it was originally derived, a beam experiment was carried out to generate matching sets of linear and angular response psd's (Appendix A). A simply supported Aluminum I-beam of 72 in was randomly excited at the midspan in such a manner that a constant acceleration response psd was maintained at the midspan over 40 - 3200 Hz. Linear displacement psd's were obtained by BBN 501 accelerometers. The discrete angle $\theta_{\Delta}(t)$ was obtained by differencing the two accelerometer signals according to formula (2)

Having maintained a constant acceleration psd at the midspan, the linear psd's at various locations on the beam obey the power-form of f^{-4} over the entire frequency range. This is most evident in $G_{yy}(f)$ taken almost at the midspan, as shown in Figure A10a in Appendix A. Away from the midspan, the linear psd's become progressively more jagged, yet they can all be represented by the power-form of f^{-4} . We shall examine here a set of the linear $G_{yy}(f)$ and differential angular $G_{\theta_{\Delta}\theta_{\Delta}}(f)$ measured at $x_1 = 25$ in and $x_2 = 29$ in on the beam (and hence $\Delta x = 4$ in). They are given in Figures A8a and A8b in Appendix A, which have been reproduced here in Figures 2a and 2b, respectively.

A least-squares power-form fit to the linear psd of Figure 2a yields

$G_{yy} = 5.0 \times 10^{-3} f^{-4}$. Hence, the angular psd predicted by Equation (21) is $G_{\theta\theta} = (\pi^2/L^2 f_1^2) f G_{yy} = 1.4 \times 10^{-7} f^{-3}$. On the other hand, by applying a least-squares straight line fit to the angular psd of Figure 2b, we obtain

$G_{\theta\theta} = 1.0 \times 10^{-7} f^{-3}$ as the measurement. Although the predicted constant factor is 40% higher than the measurement, what is noteworthy is the overall spectral

shape of the angular psd that has correctly been predicted by the power-form of f^{-3} over the entire frequency range.

SECTION IV

AIRCRAFT FLIGHT TEST DATA

It has been found in Section III that relation (21) can predict the spectral shape of angular psd's of the test beam exactly over the entire frequency range, whereas the constant factor is predicted only approximately within 40% of the measurement. It must be noted that the 40% difference in constant factors amounts to a difference of less than 20% in the predicted and actual angular rms values, which is well within the prediction limit set forth in Reference 1. For the aircraft application, the constant factor will be determined by Equation (22) instead. It is then evident that an accurate prediction of θ_{rms} is prerequisite for determining the constant factor correctly. With this in mind, we shall examine here the viability of relation (21) as it is applied to the aircraft flight test data recently acquired by this laboratory. Recall that the linear psd (Figure 2a) of the experimental beam was represented satisfactorily by a single straight line in the log-log plot over the entire frequency range. In contrast, it has been observed that some of the linear psd's of aircraft flight tests (e.g., Figures 5a and 6a) can better be represented by more than one straight line. Although there is no theoretical guideline except that the frequency band should not be too small to violate the high modal density assumption for relation (20), it was decided to represent the linear psd by two straight lines over all frequency ranges but the high frequency tail corresponding to noise. Admittedly, the splitting of linear psd into two parts, namely, the low and high frequency ranges, respectively, is quite arbitrary, hence cannot be justified on theoretical grounds. In some cases (e.g., Figure 5a), the choice of the demarcation frequency is self-evident, whereas it is not so

in other cases (e.g., Figure 4a). In any event, we have here decided to represent all the linear psd's of aircraft flight tests by two straight lines as a matter of uniformity, but not of necessity. In other words, the prediction procedures to be outlined shortly does not depend on this particular mode of representation. Perhaps, the complete structural analysis of aircraft structures might suggest a demarcation frequency based on the modal density. However, until such information is available, the choice of demarcation frequency is more or less empirical; hence, no further attempt will be made to justify it. The prediction procedures for the angular psd are as follows;

- (i) The linear psd is first divided into the low and high frequency parts, as mentioned before.
- (ii) The linear psd in each frequency range is then approximated by a straight line in the log-log plot, $G_{yy}(f) = Df^{-k}$, using a least-squares fit. Of course, the straight lines in the low and high frequency ranges do not necessarily meet continuously at the demarcation frequency.
- (iii) The linear y_{rms} is now computed by integrating $G_{yy}(f)$ over the appropriate frequency range. To predict the angular θ_{rms} , either relation (1) or (3) is used depending on the type of angular measurement employed. In other words, Δx or L must be specified.
- (iv) Finally, in each frequency range the constant factor is determined by Equation (22).

In this section, we shall examine the typical flight test data of RF-4C and F-15 fighters, CH-3E helicopter, and B-52 bomber. For the RF-4C, F-15, and CH-3E tests, the angular psd was obtained by the differential accelerometer technique, hence the prediction scheme (3) is applicable. On the other hand,

the angular differentiating accelerometer was used to acquire the angular psd of B-52, so that the angular rms value will be predicted by Equation (1) with a suitably defined L, as will be discussed later.

RF-4C Fighter

Figure 3a is the vertical displacement $G_{yy}(f)$ taken at the left wing root of a RF-4C during 0.9 M cruise; the corresponding pitch $G_{\theta_{\Delta}\theta_{\Delta}}(f)$ with $\Delta x = 24$ in is shown in Figure 3b. (They are derived from Figures 23 and 150 of Reference 2.) Using this set of psd's as a typical example, we shall illustrate the procedures (i) - (iv). To begin with, (i) the linear $G_{yy}(f)$ is divided into the low frequency range of 10 - 50 Hz and the high frequency range of 50 - 1200 Hz. As mentioned before, the spectral tail beyond 1200 Hz will be ignored, since it contains very little spectral energy. (ii) In each frequency range, the linear psd is represented by a straight line as shown in Figure 3a. The analytical expressions are $G_{yy}^{\ell} = 6.0 \times 10^{-3} f^{-4}$ and $G_{yy}^h = 1.3 \times 10^{-2} f^{-3.5}$, where the superscripts ℓ and h refer to the low and high frequency ranges, respectively. (iii) The linear rms values are $y_{rms}^{\ell} = 0.14 \times 10^{-2}$ in and $y_{rms}^h = 0.54 \times 10^{-3}$ in. Hence, using Equation (3) under $\Delta x = 24$ in, the predicted angular rms values are $(\theta_{\Delta})_{rms}^{\ell} = 0.83 \times 10^{-4}$ rad and $(\theta_{\Delta})_{rms}^h = 0.32 \times 10^{-4}$ rad. (iv) Finally, the computed constant factors by Equation (22) are $C^{\ell} = 1.4 \times 10^{-6}$ and $C^h = 5.4 \times 10^{-7}$.

Therefore, the predicted angular psd is

$$G_{\theta_{\Delta}\theta_{\Delta}}^{\ell}(f) = 1.4 \times 10^{-6} f^{-3}, \quad G_{\theta_{\Delta}\theta_{\Delta}}^h(f) = 5.4 \times 10^{-7} f^{-2.5}. \quad (23)$$

For comparison, the angular psd in Figure 3b fitted by a least-squares procedure yields

$$G_{\theta_{\Delta}\theta_{\Delta}}^{\ell}(f) = 1.4 \times 10^{-4} f^{-4.3}, \quad G_{\theta_{\Delta}\theta_{\Delta}}^h(f) = 7.0 \times 10^{-7} f^{-2.5}. \quad (24)$$

All the relevant data are summarized in Table I, and the predicted psd is compared with the actual in Figure 3b. It must be noted that both the constant factor and power exponent have been predicted quite accurately in the high frequency range. In the low frequency range, however, the predicted power exponent is considerably smaller than the actual.

F-15 Fighter

Recently, this laboratory has received some preliminary flight test data of the linear accelerometers mounted on a bulkhead (fuselage station No. 509) near the forward upper pallet attachment points of a F-15 (Reference 3).

Table I. Comparison of the measured and predicted angular vibration PSD's

Accelerate	PF - 4C		7 - 15		CH - 2E		B - 52	
	10 - 50	50 - 1200	4 - 20	20 - 200	4 - 15	15 - 220	10 - 70	70 - 500
Frequency (Hz)								
$G_{yy}(f)$	$6.0 \times 10^{-3} f^{-4}$	$1.3 \times 10^{-2} f^{-3.5}$	$9.0 \times 10^{-4} f^{-3.4}$	$1.2 \times 10^{-3} f^{-4}$	$2.8 \times 10^{-3} f^{-3.5}$	$3.2 f^{-6.2}$	$3.0 \times 10^{-5} f^{-4.4}$	$6.5 \times 10^{-5} f^{-2.7}$
Measured $G_{\theta\theta}(f)$	$1.4 \times 10^{-4} f^{-4.3}$	$7.0 \times 10^{-7} f^{-2.5}$	$2.2 \times 10^{-5} f^{-3.6}$	$8.0 \times 10^{-8} f^{-3}$	$3.5 \times 10^{-8} f^{-2}$	$2.0 \times 10^{-4} f^{-5}$	$4.0 \times 10^{-7} f^{-3.3}$	$1.2 \times 10^{-8} f^{-1.7}$
Predicted $G_{\theta\theta}(f)$	$1.4 \times 10^{-6} f^{-3}$	$5.4 \times 10^{-7} f^{-2.5}$	$3.4 \times 10^{-7} f^{-2.4}$	$9.7 \times 10^{-8} f^{-3}$	$2.3 \times 10^{-7} f^{-2.5}$	$1.1 \times 10^{-4} f^{-5.2}$	$5.6 \times 10^{-6} f^{-3.4}$	$1.3 \times 10^{-9} f^{-1.7}$
$\gamma_{rms} (in)$	1.4×10^{-3}	5.4×10^{-4}	3.6×10^{-3}	2.2×10^{-4}	5.2×10^{-3}	6.8×10^{-4}	1.9×10^{-3}	1.6×10^{-4}
Measured $\theta_{rms} (rad)$	1.5×10^{-4}	3.6×10^{-5}	1.5×10^{-4}	1.0×10^{-5}	3.0×10^{-5}	3.2×10^{-5}	2.9×10^{-5}	2.5×10^{-5}
Predicted $\theta_{rms} (rad)$	8.3×10^{-5}	3.2×10^{-5}	1.8×10^{-4}	1.1×10^{-5}	1.3×10^{-4}	1.7×10^{-5}	9.6×10^{-5}	8.4×10^{-6}

Figure 4a is the lateral displacement psd during 0.9 M flight under light buffeting; Figure 4b is the corresponding roll psd derived from the two vertically displaced accelerometers under $\Delta x = 28.9$ in. Here, we divide the linear $G_{yy}(f)$ into the low frequency range of 4 - 20 Hz and the high frequency range of 20 - 200Hz, as shown in Figure 4a. The relevant results are summarized in Table I. In the high frequency range, there is little difference in the predicted and measured $G_{\theta_{\Delta}\theta_{\Delta}}^h$ as shown in Figure 4b. As in the case of RF-4C, prediction of the power exponent is again low for the low frequency part of the angular psd.

CH-3E Helicopter

To extend the prediction scheme to yet another situation, we have presented in Figure 5 the linear and discrete angular psd's of a CH-3E helicopter during 40 knots flight with zero degree of roll. Figure 5a is the lateral displacement psd taken at the rear ramp; the corresponding yaw psd measured by linear accelerometers under $\Delta x = 56.5$ in is shown in Figure 5b. (They are derived from Figures 18 and 25 of Reference 4.) Unlike Figures 3 and 4, the linear and angular psd's of CH-3E have a series of spikes corresponding to the discrete-frequency vibration induced by the main and tail rotor blades. Overlooking such spikes, we shall formally apply the prediction procedures by splitting the linear $G_{yy}(f)$ into the low frequency range of 4 - 15 Hz and the high frequency range of 15 - 220 Hz. The predicted angular psd is summarized in Table I and compared in Figure 5b with the measurement. The power exponents have been predicted satisfactorily in both the low and high frequency ranges. On the other hand, the predicted

magnitude levels deviate from the measurement almost by plus and minus 6 db (based on $10 \times \log[\text{measured psd level}/\text{predicted psd level}]$) in the low and high frequency ranges, respectively. This may be attributed to the uncertainty in rms values when the psd's are infested by spikes representing discrete-frequency rotor resonances.

B-52 Bomber

Lastly, we shall examine a typical set of linear and angular psd's of the B-52 flight test during initial take-off. Figure 6a is the vertical displacement psd taken at the forward end of an armor storage compartment near the bulkhead, fuselage station No. 1853; Figure 6b is the corresponding angular psd of pitch component fluctuations measured by an angular differentiation accelerometer (ADA). (They are derived from Figures 68 and 73 of Reference 5.) After splitting the linear psd into the low frequency range of 10 - 70 Hz and the high frequency range of 70 - 500 Hz, the prediction procedures have been repeated but with the angular rms value predicted by Equation (1) under $L = 72$ in. which is the linear dimension of the test platform. From the results compiled in Table I and depicted in Figure 6b, one finds that the spectral shape has been predicted accurately for both $G_{\theta\theta}^L$ and $G_{\theta\theta}^h$. In contrast, the predicted constant factors are off almost by ± 10 db. Although this cannot be explained away in certainty, it is suspected that the angular psd measurement by an ADA transducer is not trustworthy. In particular, the angular psd (Figure 6b) shows much higher spectral energy buildup in the high frequency range than any of the discrete angular psd's of RF-4C, F-15, and CH-3E. Other angular psd's of the B-52 test exhibit a similar spectral energy buildup, as has already been observed in another flight test which also employed the ADA transducer (Reference 11).

Whether this peculiarity is simply a quirk of the ADA or a genuine structural behavior is yet to be resolved.

In summary, the angular psd of the typical flight tests of RF-4C, F-15, CH-3E, and B-52 has been predicted with a varying degree of success. First, the spectral shape of angular psd can be predicted quite accurately in the high frequency range, but not always so in the low frequency range. This is in a way expected because the linear-angular psd relation (20) is an asymptotic expression valid for the high frequency range. Second, it is difficult to accurately predict the magnitude level of angular psd in that the correct power exponent and rms amplitude of the angular vibration must be available. Last but not least, it must be pointed out that the prediction procedures are subject to the numerical variations of 0.1 in the power exponent and 10% in the magnitude level. This is due to the uncertainty in estimating the power exponent and constant factor of a straight line representation of the psd data.

SECTION V

OVERALL ASSESSMENT OF THE PREDICTION SCHEME

The angular psd prediction has been carried out in two steps. In the first step, the exponent $(1-k)$ of power-form expression (21) is estimated. The power exponent has been predicted very accurately for the high frequency range of angular psd's. On the other hand, the predicted exponent deviates from the actual as much as 1.3 in the low frequency range. This is, however, not unexpected because the linear-angular psd relationship derived here is an asymptotic expression valid for the high frequency.

The second step involves estimating the constant factor by Equation (22) based on the power exponent k and angular rms θ_{rms} . Deviating from the original derivation in Reference 1, it was assumed that relations (1) and (3) can be applied to the rms values computed over a limited frequency band as well as the entire frequency range. This assumption, however, appears to be a weak link. In the B-52 case, for instance, the predicted θ_{rms}^h underestimates the actual value by threefold, whereas the predicted θ_{rms} over the entire frequency range is within 50% of the measurement. Note, however, that this prediction accuracy is worse than the $\pm 20\%$ limit claimed for the total θ_{rms} in Reference 1.

Of course, the overall assessment of the prediction scheme must take into account both the power exponent and constant factor. From Figures 2b, 3b, 4b, and 5b, it is concluded that in both the low and high frequency ranges the predicted angular psd lies within ± 10 db of the measurement. Though crude, the prediction scheme will be useful in the preliminary design stage of electro-optical systems because it can provide a quick assessment of the angular vibration environment prior to fabrication. To build up further

confidence, we hope to test the prediction scheme on some new flight test data as they soon become available to us, perhaps, with the purpose of establishing certain confidence intervals.

In retrospect, the major thrust of this report was to propose a simple formula to predict the angular vibration psd of aircraft structures using the least amount of information, i.e., the linear psd and a length scale (Δx or L). Consequently, the prediction capability is limited. The overall performance, however, is quite encouraging in that the present work is just an exploratory attempt of first order. Clearly, the more information is utilized, the closer one should be able to predict the angular psd. Of course, the numerical structural analysis of an aircraft could yield the detailed angular vibration characterizations at every point on the aircraft structure, subject to arbitrary aerodynamic and acoustic random excitations. Unfortunately, this does not seem feasible at the present state-of-the-art of computer structural analysis.

REFERENCES

1. Lee, J. and Whaley, P. W., Prediction of the Angular Vibration of Aircraft Structures, AFFDL-TR-76-56, AF Flight Dynamics Laboratory, Wright-Patterson AFB, Ohio, June 1976; also Journal of Sound and Vibration, Vol. 49, 541 - 549, December 1976.
2. Whaley, P. W. and Hall, K. S., Test Report on Vibration and Acoustic Survey of the RF-4C for Vibration Transmission Studies, AFFDL/FBG/77-8, AF Flight Dynamics Laboratory, Wright-Patterson AFB, Ohio, November 1977.
3. Newberry, C. H. and et al., F-15 Pressure and Vibration Loads Measurement Program - Flight Test Plan, Contract No. F29601-77-C-0096, McDonnell Aircraft Co., St. Louis, Missouri, September 1977.
4. Whaley, P. W. and Bolds, P. G., Test Report on Vibration Survey of the CH-3E Helicopter for the SAR-RETRAN Guidance Test Program, AFFDL/FBG/77-1, AF Flight Dynamics Laboratory, Wright-Patterson AFB, Ohio, May 1977.
5. Davis, W. R., Jr., Obal, M. W., Hall, K. S., and Brown, D. L., Test Report on B-52 Linear and Angular Flight Vibration Measurements, AFFDL/FBG/77-6, AF Flight Dynamics Laboratory, Wright-Patterson AFB, Ohio, September 1977.
6. Eringen, A. C., "Response of Beams and Plates to Random Loads," Journal of Appl. Mech., Vol. 24, 46-52, March 1957.
7. Bogdanoff, J. L. and Goldberg, J. E., "On the Bernoulli-Euler Beam Theory with Random Excitation," Journal of Aerospace Sci., Vol. 27, 371-376, May 1960.
8. Bendat, J. S. and Piersol, A. G., Random Data: Analysis and Measurement Procedures, Wiley-Interscience, New York, 1971.

9. Timoshenko, S., Young, D. H., and Weaver, W., Jr., Vibration Problems in Engineering, 4th Ed., John Wiley, New York, 1974.
10. Whaley, P. W. and Brown, D. L., Prediction of Angular Disturbances from Airframe Members to Airborne Electro-Optical Packages, Preprint of NEACON '78, Dayton, Ohio, 16-18 May, 1978.
11. Sher, L., Angular Vibration Effects on a Telescope System, AFWL-TR-72-202, AF Weapons Laboratory, Kirtland AFB, New Mexico, February 1973.

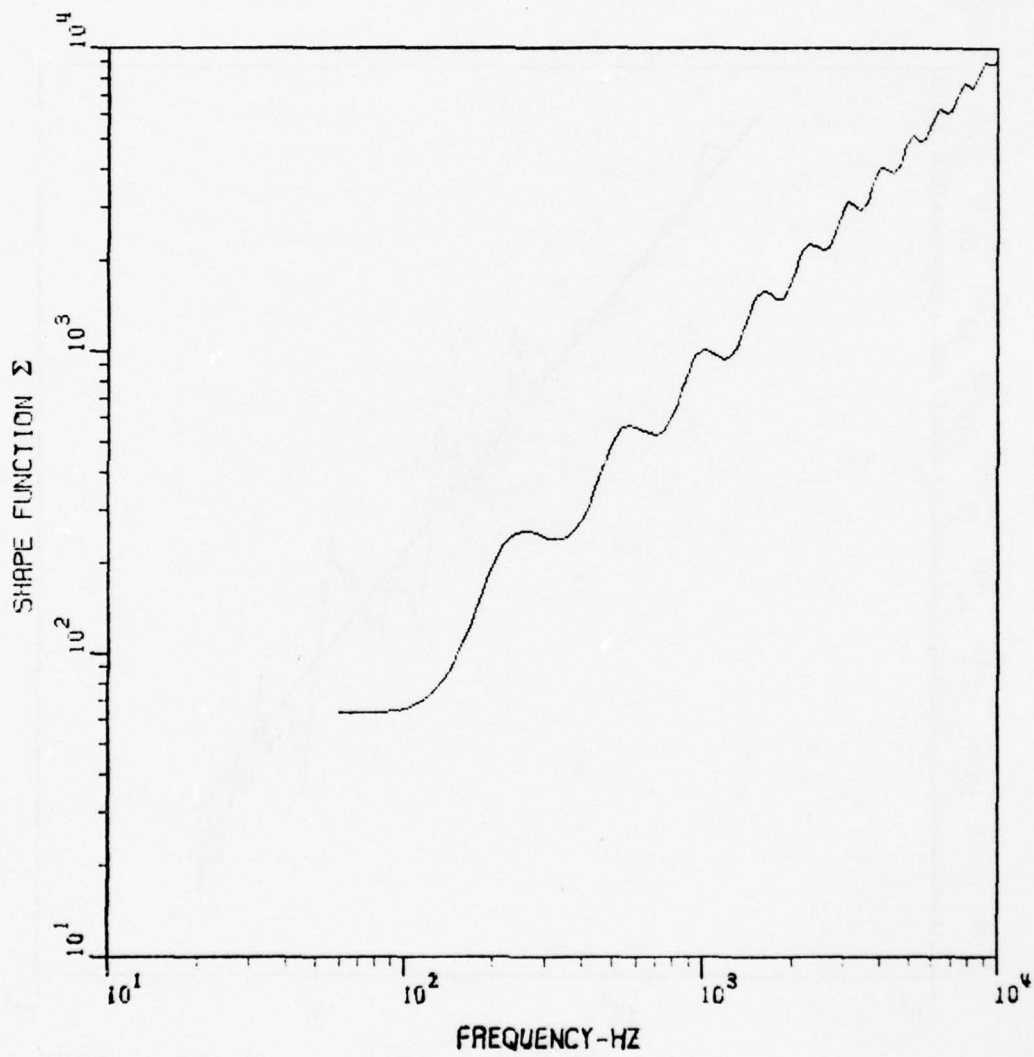


Figure 1. Numerical Computation of Σ ;
 $E = 10^7 \text{ lb/in}^2$, $I = 1.855 \text{ in}^4$, $\rho = 0.131 \text{ lb/in}^3$
 $A = 1.244 \text{ in}^2$, $L = 72 \text{ in}$, $\beta = \omega_1/20$

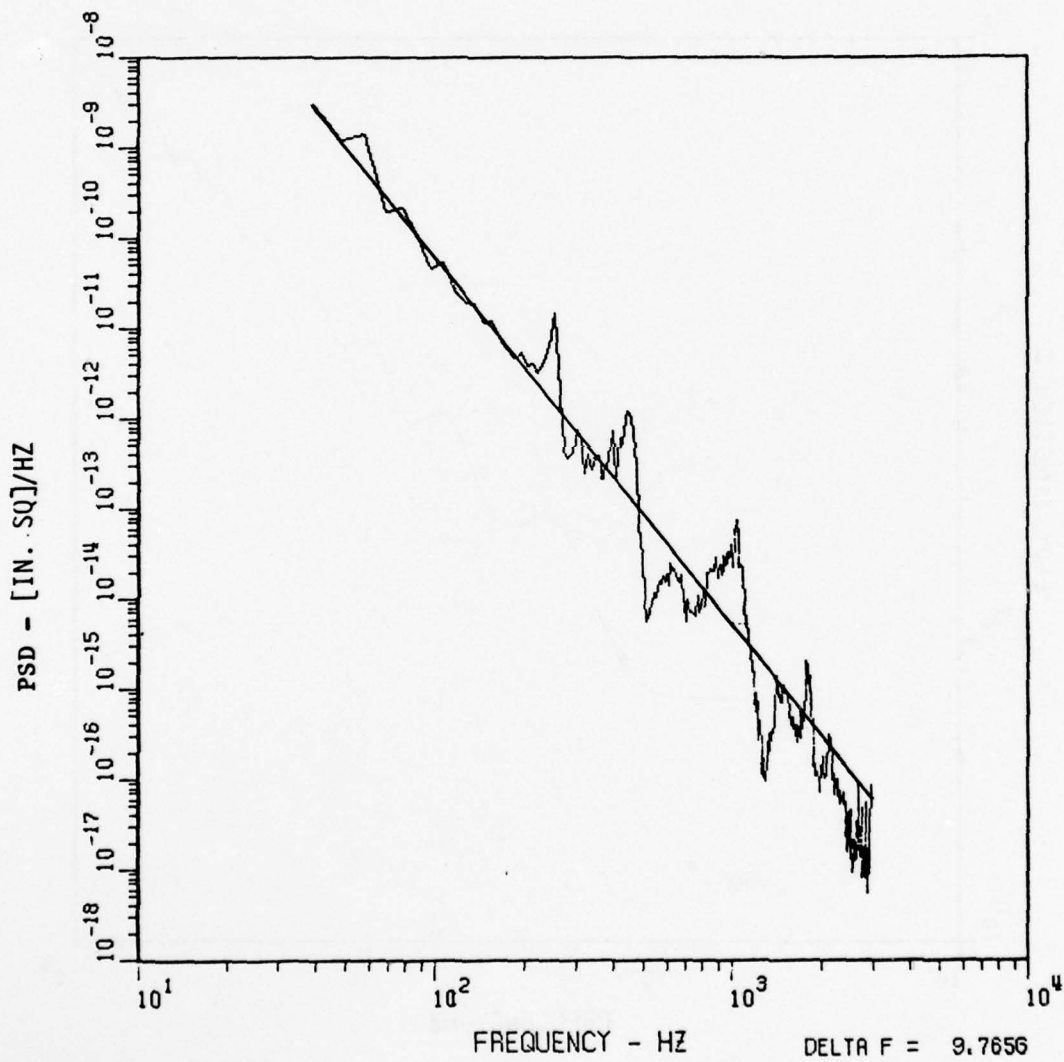


Figure 2a. Linear Power Spectral Density of the Test Beam at $X_1 = 25$ in.
 ——— Least-Squares Approximation; $5.0 \times 10^{-3} f^{-4}$

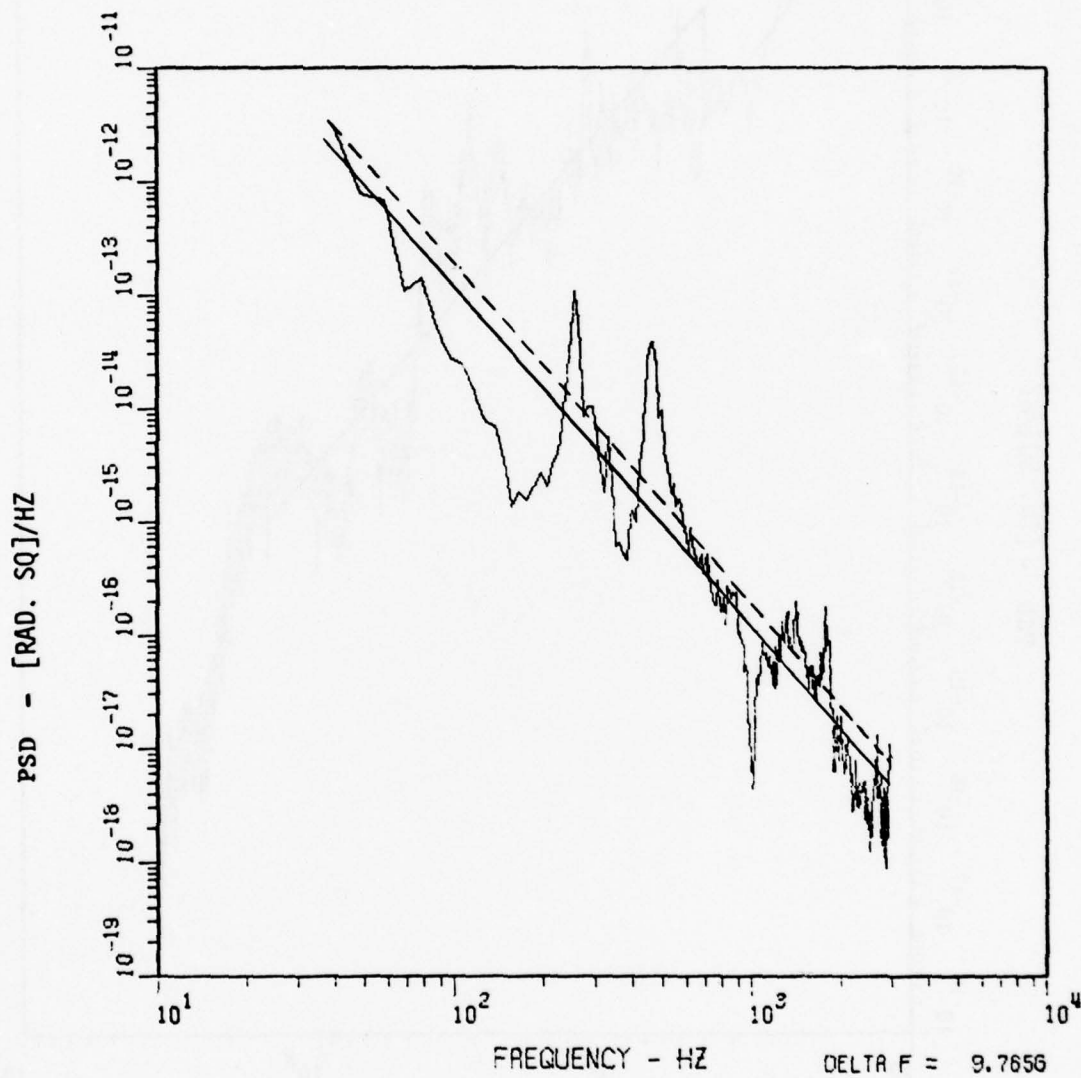


Figure 2b. Angular Power Spectral Density of the Test Beam at $X_1 = 25$ in. and $X_2 = 29$ in.

————— Least-Squares Approximation: $1.0 \times 10^{-7} f^{-3}$;
 - - - - - Prediction: $1.4 \times 10^{-7} f^{-3}$

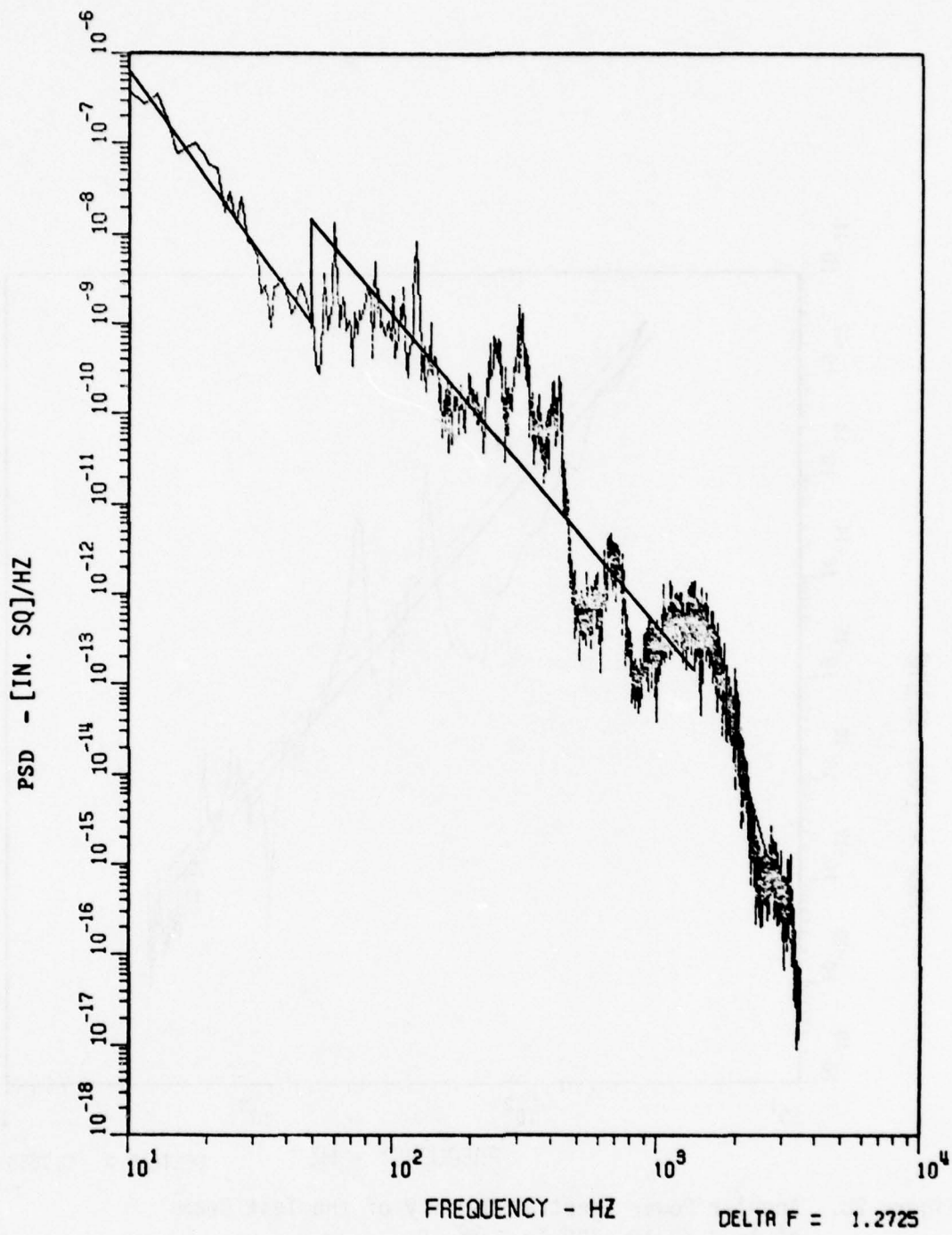


Figure 3a. Linear Power Spectral Density of the RF-4C Flight Test (Vertical)

— Least-Squares Approximation

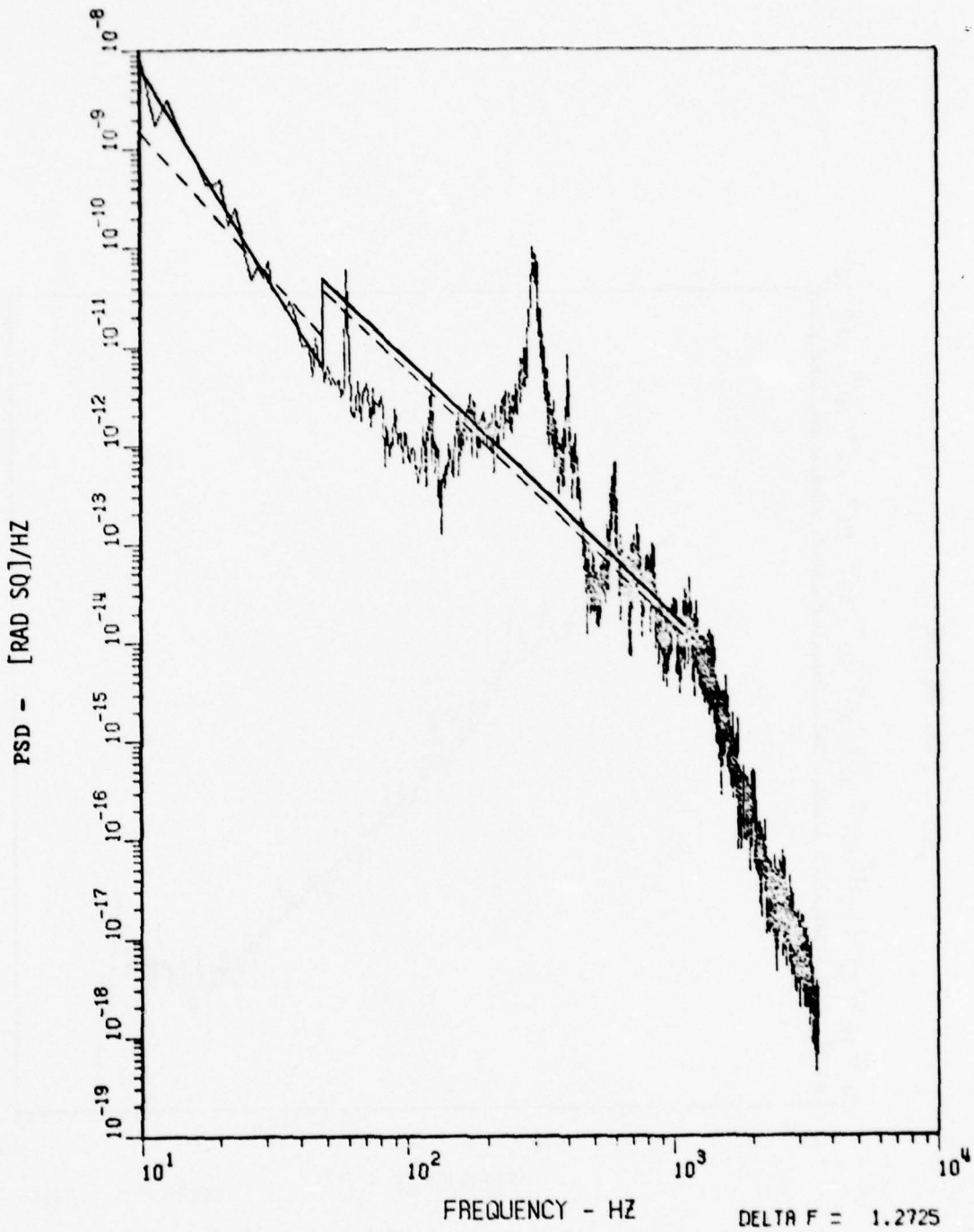


Figure 3b. Angular Power Spectral Density of the RF-4C Flight Test (Pitch)

————— Least-Squares, Approximation;
 - - - - - Prediction

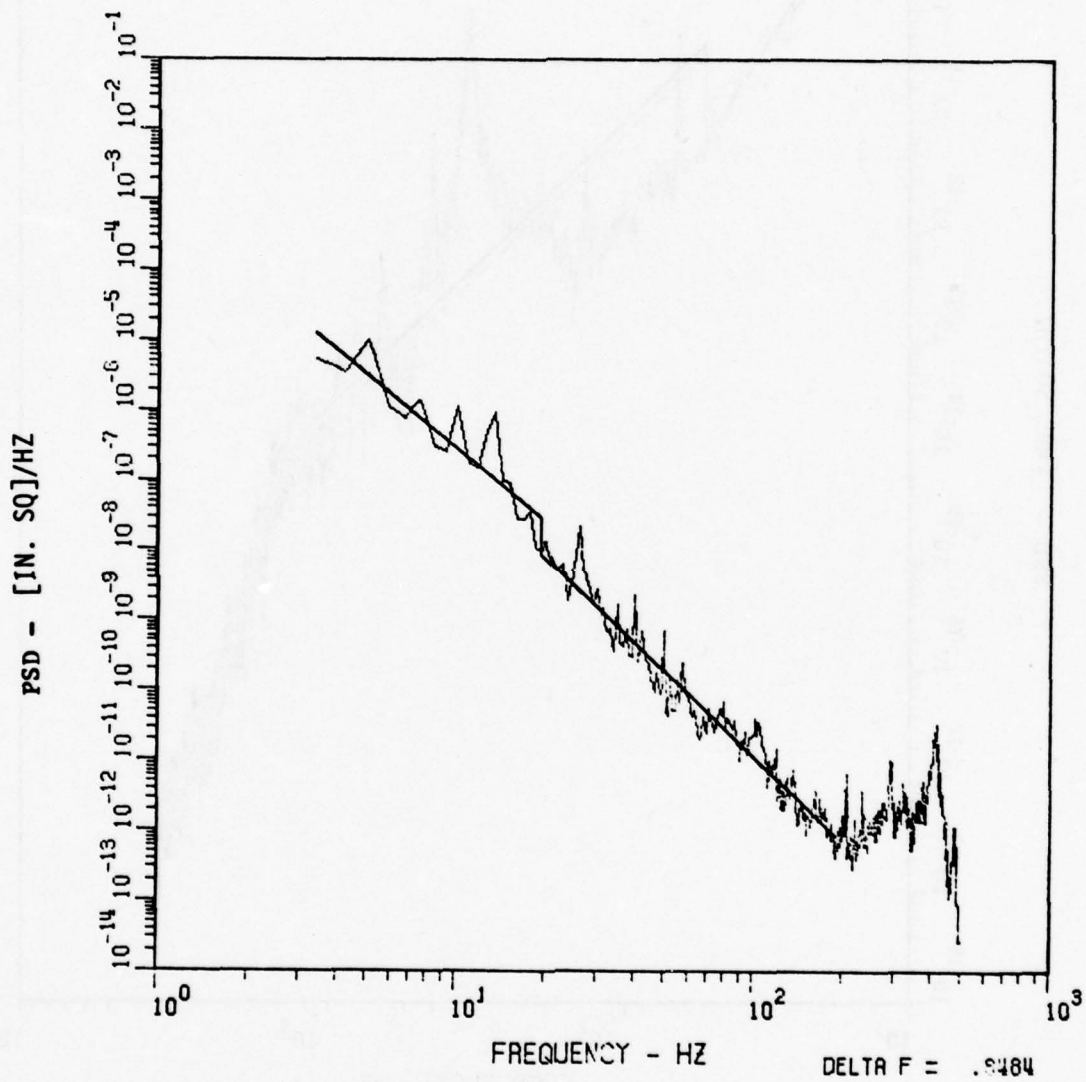


Figure 4a. Linear Power Spectral Density of the F-15 Flight Test (Lateral)

— Least-Squares Approximation

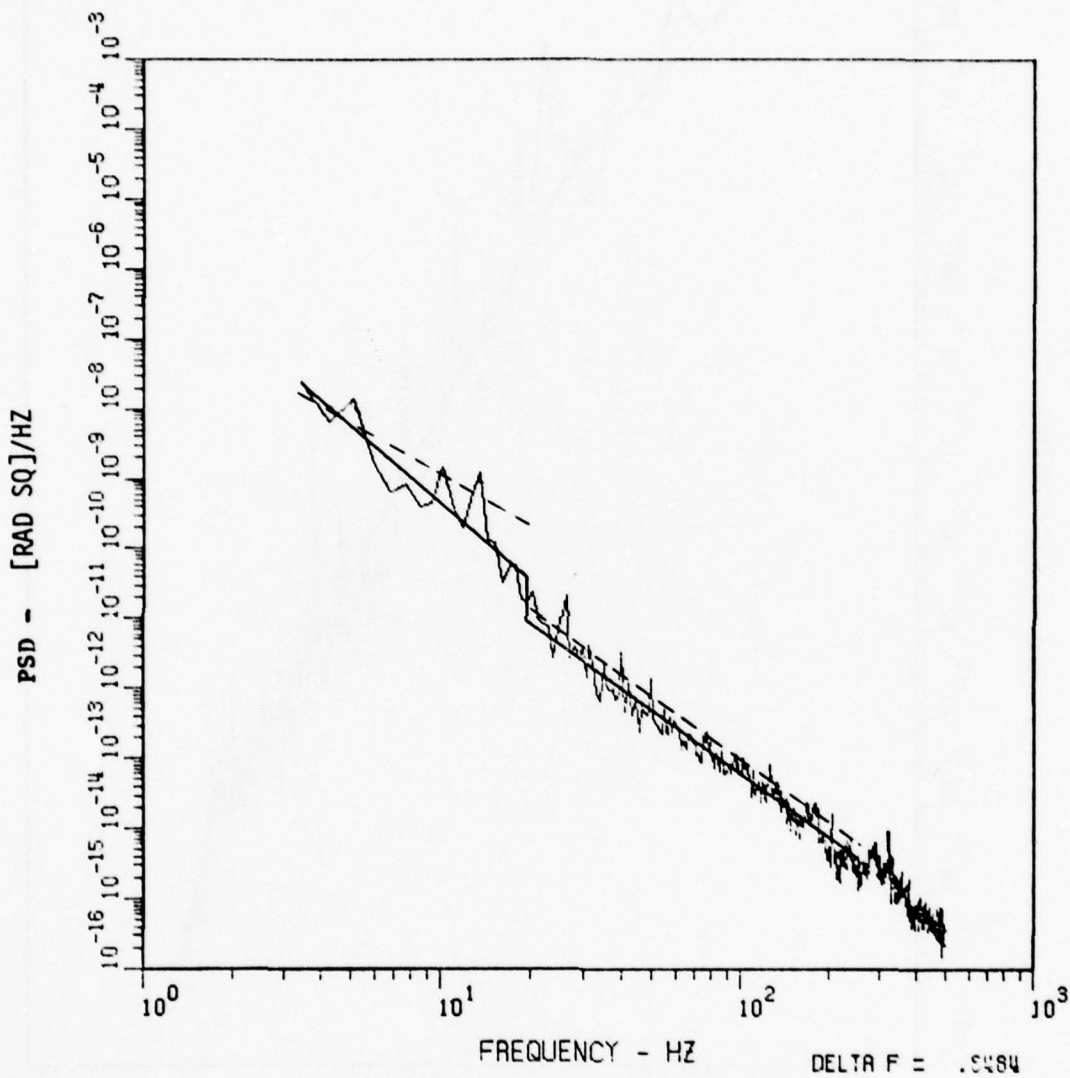


Figure 4b. Angular Power Spectral Density of the F-15 Flight Test (Roll)

- Least-Squares Approximation ;
- Prediction

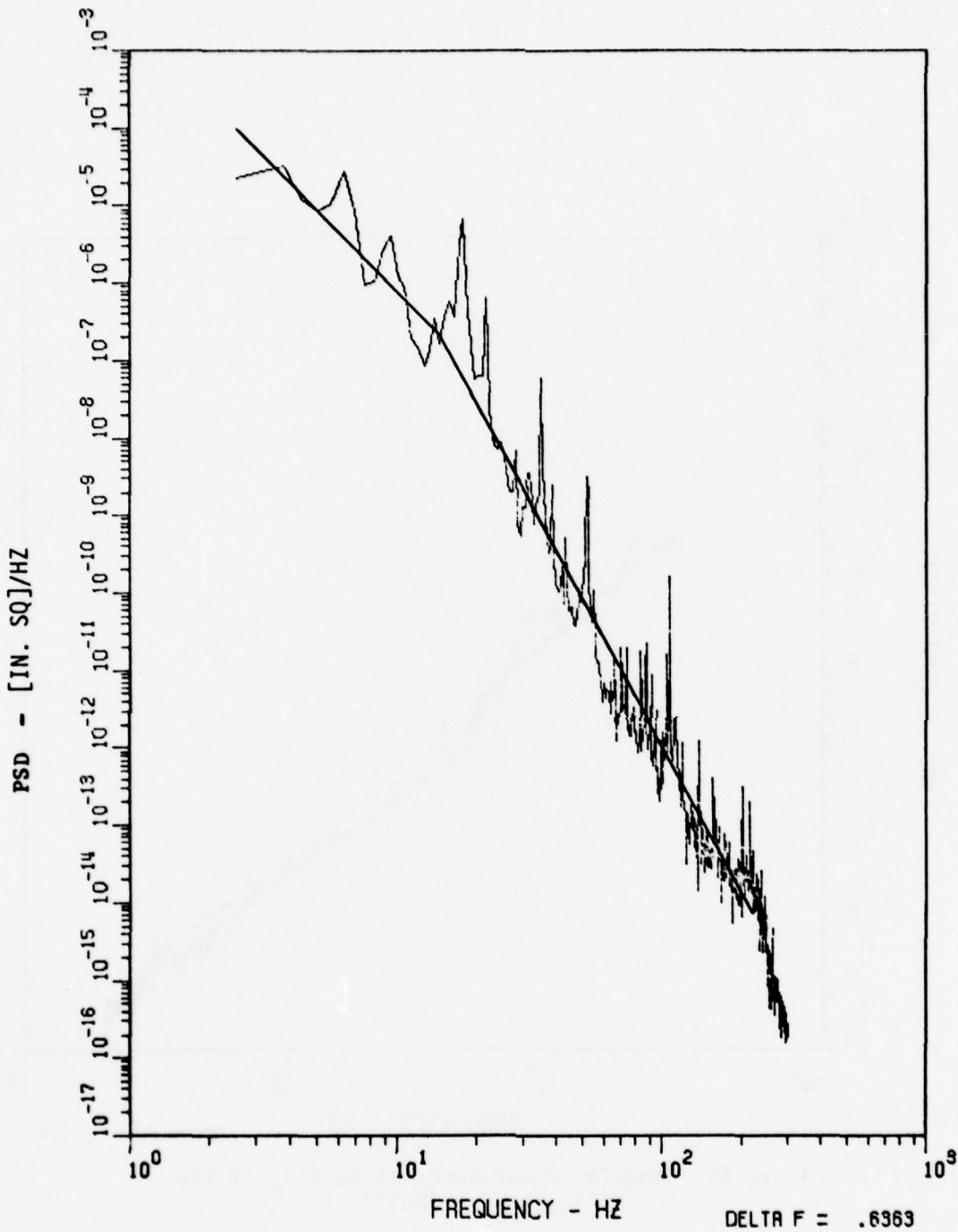


Figure 5a. Linear Power Spectral Density of the CH-3E Flight Test (Lateral)

— Least-Squares Approximation

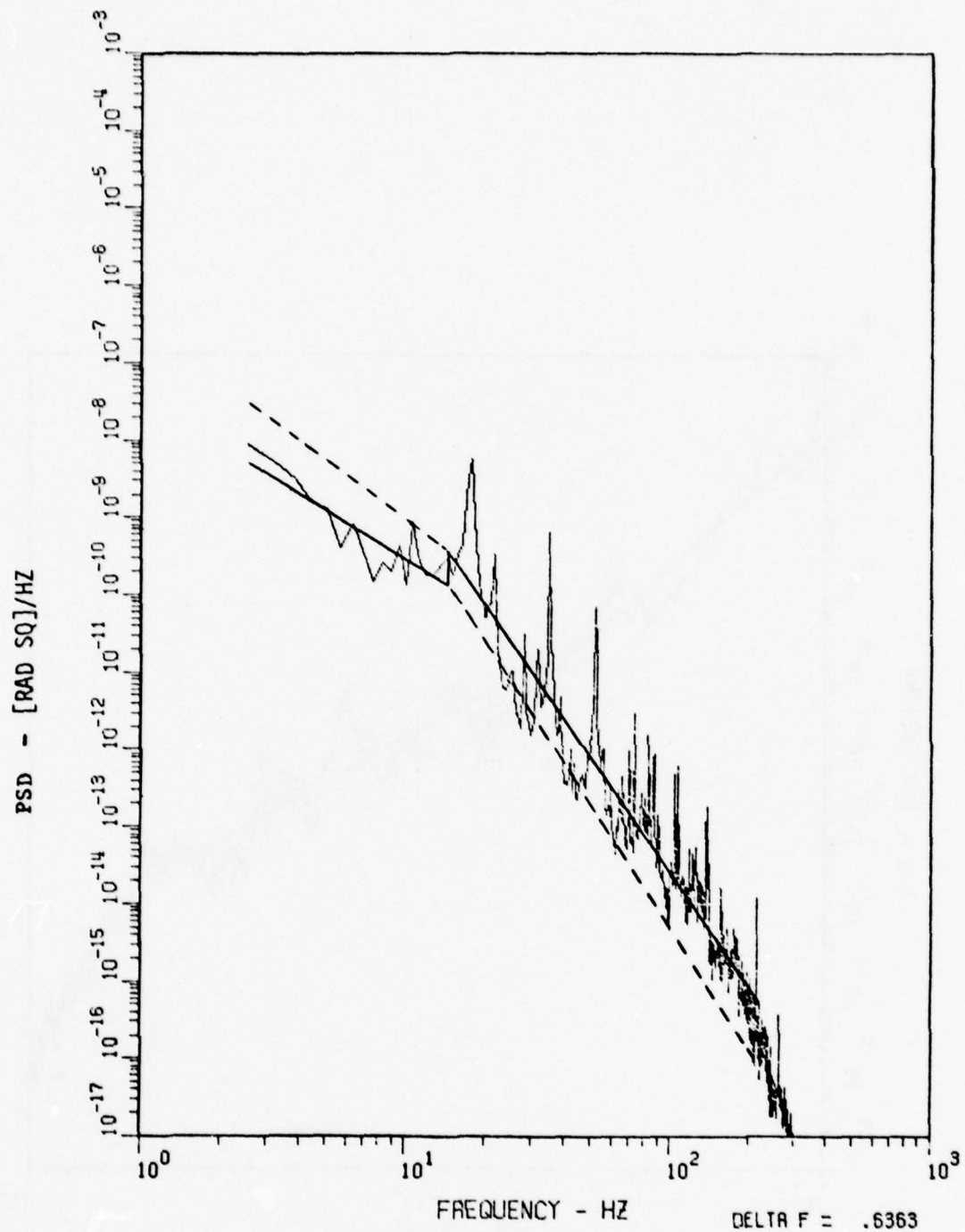


Figure 5b. Angular Power Spectral Density of the CH-3E Flight Test (Yaw)

- Least-Squares Approximation;
- Prediction

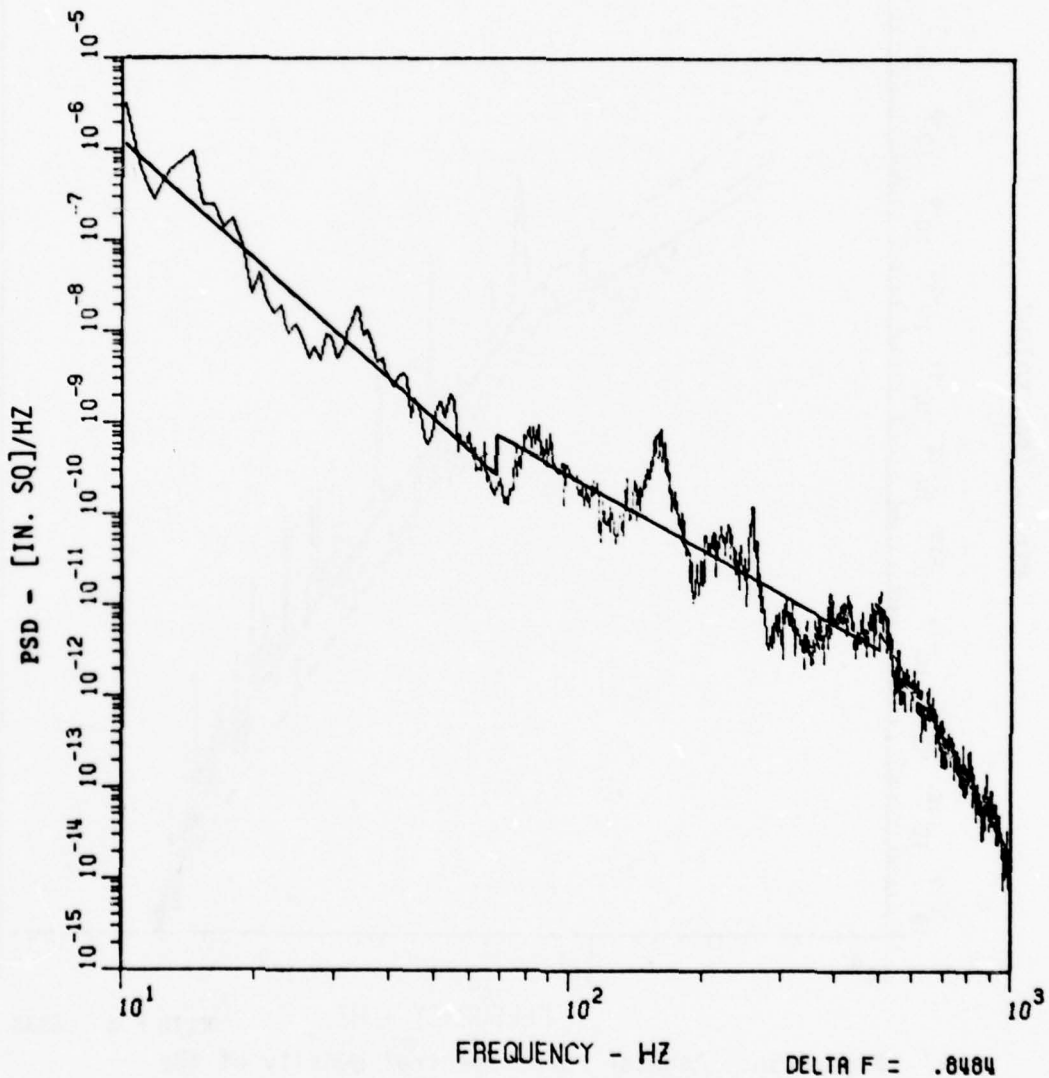


Figure 6a. Linear Power Spectral Density of the B-52 Flight Test (Vertical)

————— Least-Squares Approximation

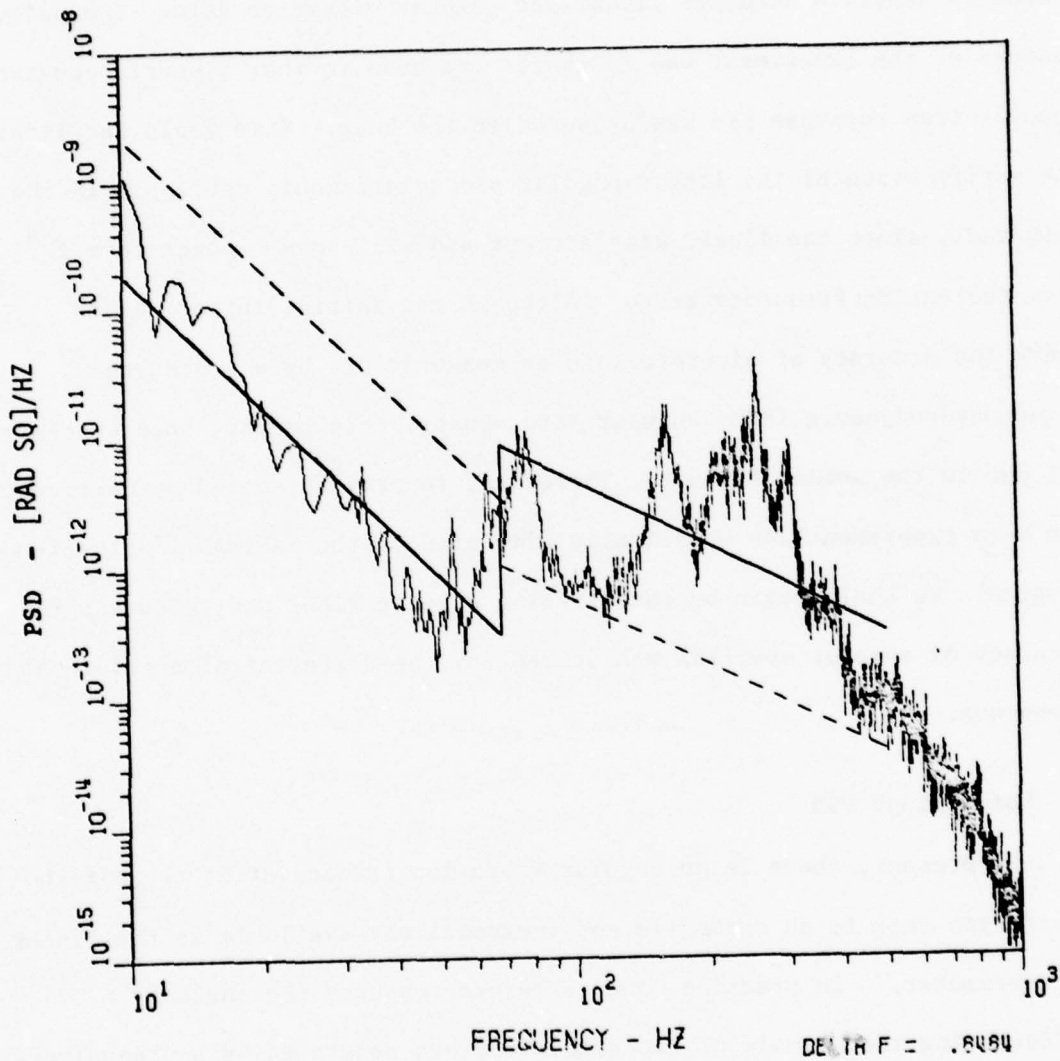


Figure 6b. Angular Power Spectral Density of the B-52 Flight Test (Pitch)

- Least-Squares Approximation ;
- Prediction

APPENDIX A
BEAM EXPERIMENT

This appendix describes the experiment of a simply supported Aluminum I-beam to generate accurate linear and angular vibration data. The unique feature of the experiment was to excite the beam so that a nearly constant acceleration response psd was produced on the beam. This would facilitate the verification of the linear-angular psd relationship developed in the main text, since the linear displacement psd will have power-form f^{-4} over the entire frequency range. Although the initial intent was to check the accuracy of discrete angular measurements by a prototype magnetohydrodynamic (MHD) angular rate sensor, this has not been successful due to the sensor failure. Therefore, to provide an independent check, the beam experiment was numerically simulated by the NASTRAN finite-element program. We shall begin by establishing a noise floor pad to assess the accuracy of angular spectral measurement by the differential accelerometer technique.

I. Noise Floor PSD

At present, there is no angular vibration transducer of the off-the-shelf type that is as versatile and **inexpensively available** as the linear accelerometer. In practice, one therefore measures the angle by differencing the signals of two accelerometers separated by a preassigned distance. In other words, approximate the true angle $\theta(x,t)$ by Equation (2) repeated here for reader's convenience

$$\theta_{\Delta}(t) = [y_2(t) - y_1(t)]/\Delta x, \quad (2)$$

where $y_1(t)$ and $y_2(t)$ are the transverse displacements at x_1 and x_2 , respectively, and $\Delta x = x_2 - x_1$ is the separation distance. Using the center location $x_c = (x_1 + x_2)/2$, we have $x_1 = x_c - \Delta x/2$ and $x_2 = x_c + \Delta x/2$; hence, the discrete or differential angle $\theta_\Delta(t)$ can be expressed in terms of x_c and Δx .

Formal manipulations of definition (2) will shed light on the limitation of discrete angular measurements. First, obtain the variance relationship

$$\langle \theta_\Delta^2(t) \rangle = \frac{1}{(\Delta x)^2} (\langle y_1^2(t) \rangle + \langle y_2^2(t) \rangle - 2\langle y_1(t)y_2(t) \rangle). \quad (23)$$

The right-hand side is poorly conditioned in that it will fall below the noise floor for $\langle y_1^2 \rangle = \langle y_2^2 \rangle = \langle y_1 y_2 \rangle$ as Δx becomes small. This therefore imposes a minimum Δx for the discrete angular measurement.

To analyze this, let us split $y_i(t)$ into the true signals $\hat{y}_i(t)$ and the noises $e_i(t)$ (for $i = 1$ and 2). Under the usual assumption that $e_i(t)$ are statistically independent of $y_i(t)$ and of each other, one finds that

$$\langle \theta_\Delta^2(t) \rangle = \langle \hat{\theta}_\Delta^2(t) \rangle + \frac{1}{(\Delta x)^2} (\langle e_1^2(t) \rangle + \langle e_2^2(t) \rangle), \quad (24)$$

where $\langle \hat{\theta}_\Delta^2(t) \rangle$ is given by Equation (23) in which the $y_i(t)$ are replaced by $\hat{y}_i(t)$. Further assuming $\langle e_1^2(t) \rangle = \langle e_2^2(t) \rangle = \langle e^2(t) \rangle$, Equation (24) reduces to

$$\langle \theta_\Delta^2(t) \rangle = \langle \hat{\theta}_\Delta^2(t) \rangle + \frac{2}{(\Delta x)^2} \langle e^2(t) \rangle, \quad (25)$$

and its psd analog is

$$G_{\theta_{\Delta}\theta_{\Delta}}(f) = G_{\hat{\theta}_{\Delta}\hat{\theta}_{\Delta}}(f) + \frac{2}{(\Delta x)^2} G_{ee}(f). \quad (26)$$

Because of the factor $(\Delta x)^{-2}$ in Equations (25) and (26), the signal-to-noise ratio would improve as Δx increases. Although this is desired, Δx cannot be increased indefinitely without deteriorating resolution (Reference A1). For better resolution, one must operate in the opposite range of small Δx . However, as Δx decreases signal may be overshadowed by the noise term which increases by the factor $(\Delta x)^{-2}$. This therefore sets a minimum Δx for the acceptable signal-to-noise.

Now, to establish a reference psd $\overline{G_{\theta_{\Delta}\theta_{\Delta}}}(f)$ corresponding to a prescribed signal-to-noise ratio (S/N), let the ratio $G_{\theta_{\Delta}\theta_{\Delta}}(f)/(2G_{ee}(f)/(\Delta x)^2)$ be $(S/N)^2$ (and not (S/N) because the psd refers to the spectral energy).

Then, by rearrangement

$$\overline{G_{\theta_{\Delta}\theta_{\Delta}}}(f) = \frac{2(S/N)^2}{(\Delta x)^2} G_{ee}(f). \quad (27)$$

Typically, the noise floor of accelerometers has a flat psd in the noise acceleration; hence the noise psd is $G_{ee}(f) = c_1 f^{-4}$, where c_1 is a constant to be determined later. In view of this, Equation (27) becomes

$$\overline{G_{\theta_{\Delta}\theta_{\Delta}}}(f) = \frac{2 c_1 (S/N)^2}{(\Delta x)^2} f^{-4}. \quad (28)$$

For a given (S/N), Equation (28) therefore defines a reference psd; angular spectral measurements falling below it should be rejected.

II. Experimental Beam Test

1. The Test Set-Up

A simply supported Aluminum I-beam was randomly excited at the midspan in such a manner that a constant acceleration response psd over 40-3200 Hz was maintained at the midspan. For the simply supported end condition, the beam was fastened to the supporting bases by a pin support mechanism consisting of precision needle bearings and high-temperature hardened steel shafts. The supporting bases consisting of a 12" high and 8" diameter solid Aluminum pedestal, were bolted to a massive vibration test table as shown in Figure A1. Although the rotation centers of bearings were not on the central bending axis of the beam, this would not result in significant inplane stresses because the transverse displacement was kept small during the experiment. The effective beam length between the bearing centers was 72 in.

A 25 lb. electrodynamic shaker (Ling Model 6C) was attached to the bottom flange at the midspan of the beam via a fusible link, thereby transmitting only the vertical force and no moments to the beam. To maintain a constant acceleration response psd at the midspan, the shaker power amplifier was monitored and controlled by a Time/Data **Vibration Control and Analysis** computer. This control computer compares the actual acceleration psd at the midspan with a prescribed one and then minimizes the difference. Figure A2 shows a typical acceleration psd that the control computer has maintained constant over 40 - 3200 Hz. The dotted lines represent a ± 6 db band about the control reference psd.

2. Test Procedures

Linear displacements were measured by BBN 501 accelerometers. The differential angle was obtained by electronically differencing the signals of two accelerometers and then dividing by the separation distance as indicated by Equation (2). Accelerometer signals were amplified by Intech amplifiers and recorded on FM tapes (15 ips, 27K Hz center frequency, and 5K Hz bandwidth). Only the even channels of a recorder (Honeywell 9600) were used to minimize the possible phase error introduced by the tape heads. Both the individual accelerometer and electronically differenced signals were recorded. Prior to data acquisition, the two accelerometers used for discrete angular measurements were balanced to ensure the phase and magnitude compatibility. This was done by applying 1g excitation at 60 Hz to both accelerometers placed on the 1g calibration table (B & K TY6106). After having amplified each accelerometer signal, their difference was displayed on an oscilloscope. A balance pot placed in line with one of the accelerometers before amplification was then adjusted until a null difference was obtained. In addition, the signal conditioning electronics was calibrated by recording a 1000 Hz sine wave at 40 db amplification on each channel. This amplification level was the one used in the experiment. Figure A3 is the schematic diagram of instrumentation set-up.

The test procedures may be summarized:

- (1) A prescribed acceleration psd over 40-3200 Hz was entered into the control computer system.

- (2) For the discrete angular measurement, two accelerometers were placed on the beam separated by a predetermined Δx at the location x_c . A MHD angular rate sensor was mounted at $x_c = 27''$. Although it failed to operate properly, it was kept in its place during the experiment.
- (3) The shaker feedback control system was activated. After a steady-state excitation had been attained, the accelerometer signals including the differenced signal were simultaneously recorded.

3. Summary of Test Results

All data were recovered through the FM playback equipment, filtered for anti-aliasing, and digitized onto digital magnetic tape via an ITI Analog-to-Digital converter. Psd's were computed with a 9.8 Hz bandwidth using the fast Fourier transform on a Raytheon 704 computer. The acceleration psd's are multiplied by the factor $(2\pi f)^{-4}$ to yield the corresponding displacement psd, which is permissible for a stationary random process.

For the first five tests, Δx was varied from 4 in to 12 in with a 2 in increment at $x_c = 27$ in. Four additional tests were then performed with $\Delta x = 4$ in but by varying x_c . They are designated by the test numbers in Table A1.

Test No	x_c (in)	Δx (in)	Linear $G_{y_1 y_1}(f)$ at $x_1 = x_c - \Delta x/2$	Angular $G_{\theta \Delta \theta}(f)$
1	19	4	Figure A7a	Figure A7b
2	27	4	Figure A8a	Figure A8b
3	27	6		Figure A8c
4	27	8		Figure A8d
5	27	10		Figure A8e
6	27	12		Figure A8f
7	32	4	Figure A9a	Figure A9b
8	36	4	Figure A10a	Figure A10b
9	50	4	Figure A11a	Figure A11b

Table A1. Summary of Test Results

The accelerometer locations defined in terms of the center location x_c and separation distance Δx are shown in Figure A4.

Included in this report are only some of the linear $G_{y_1 y_1}(f)$ at x_1 , since they are representative of the others. For the same reason, none of the linear $G_{y_2 y_2}(f)$ at $x_2 (= x_c + \Delta x/2)$ are explicitly shown here. Note that x_c of Test No. 1 is the farthest from the midspan. The x_c 's of Test Nos. 2, 7, and 8 get closer to the midspan, until x_c is the midspan for Test No. 8. The test results are first compared with the NASTRAN prediction in the next section and then discussed further in Section IV of this appendix.

III. Finite-Element Simulation of the Beam Experiment

As mentioned before, it was originally intended to check the accuracy of discrete angular measurements by a MHD angular rate sensor. However, this prototype sensor had failed during the experiment, hence it could not be used for comparison. To provide an independent check, it was therefore decided to simulate the beam experiment by a finite-element numerical method.

1. The NASTRAN Model

The Level 15 NASTRAN finite-element code was used to numerically simulate the experimental beam (References A2 and A3). The finite-element model which includes the attached masses of shaker armature and MHD sensor, consists of 15 NASTRAN CBAR elements, as shown in Figure A4. There are in all 30 degrees of freedom; 14 for the vertical modes and 16 for the rotational modes along the axes normal to the y- and x-coordinates. The end nodes were vertically constrained to represent the simply supported ends. The remaining node points correspond either to the accelerometer locations or the center locations for discrete angle. The distance between any adjacent nodes is less than 6", thus permitting excitation of at least the first six bending modes, so as to correctly represent the frequency range up to 3200 Hz. The shaker armature (0.79 lb.) and the MHD sensor with supporting brackets (1.18 lb.) were incorporated as a point mass into nodes No. 9 and No. 7, respectively. The appropriate material constants such as $E = 10^7 \text{ lb/in}^2$, $I = 1.855 \text{ in}^4$, $\rho = 0.131 \text{ lb/in}^3$, and $A = 1.244 \text{ in}^2$, and the structural damping constants (determined experimentally in Appendix B) were introduced into the NASTRAN program, a brief outline of which can be found in Appendix C.

2. The Forcing PSD

To simulate the experiment, it is necessary to reconstruct an equivalent forcing psd at the midspan that would have produced the constant acceleration response psd. Reference A4 describes how this can be done. First, the finite-element model is loaded at the midspan with a constant lg force over 40-3200Hz, and then the response acceleration psd is determined at the midspan. Clearly, the acceleration psd will not be flat, nor will it be of the same magnitude as the experiment. Therefore, the magnitude of the forcing psd in each frequency band must be adjusted so that the computed response acceleration of the NASTRAN model will match the experiment. Figure A5 is a typical forcing psd necessary to produce a constant acceleration response psd shown in Figure A6, in which the NASTRAN and experimental acceleration psd's are compared with good agreement.

3. Comparison of the NASTRAN results with Experimental Data

It is observed from Figures A7-A11 that NASTRAN can qualitatively predict the beam experiment, although some quantitative differences exist in the resonance frequency and its peak height. In general, the agreement between the NASTRAN result and experiment is much better for $G_{y_1 y_1}(f)$ than for $G_{\theta_{\Delta} \theta_{\Delta}}(f)$. This is not at all unexpected because differential angular measurements are vulnerable to the signal differencing error. Clearly, the worst comparison is observed in Figure A10 for the angular psd at the midspan; the NASTRAN $G_{\theta_{\Delta} \theta_{\Delta}}(f)$ is much lower than the experimental in the very low frequency range. This indicates that the experimental beam deviates from the simply supported end condition and midspan local excitation. According to the theoretical analysis (Equation 16), the angular psd is zero at the midspan because only the odd modes can survive

under the local midspan forcing. In reality, however, the spatial function is not exactly $\cos^2(n\pi x/L)$ due to the added masses of shaker armature and MHD sensor, which would certainly result in unsymmetric mode shapes. Nevertheless, the low level of $G_{\Delta\theta\Delta\theta}(f)$ predicted by NASTRAN appears to be consistent with the unsymmetric mode considerations.

VI. Discussion of the Experimental Results

The discrete angular signal was generated by instantaneously differencing the signals of two accelerometers separated by Δx . To detect balancing errors, the two accelerometer signals, replayed from FM tape, were digitally differenced to compute the differential angle. As anticipated, there is no difference in the two angular psd results. This is seen by comparing the angular psd of Figure A8b with Figure A12 which is the angular psd obtained by digitally differencing the recorded accelerometer signals. In this section, we shall first assess the accuracy of discrete angular measurements in terms of the noise floor psd and then examine the spatial variation of the linear and angular rms amplitudes.

1. Noise Floor PSD

The angular psd will be compared with the reference noise psd given by Equation (28). The constant c_1 in that equation can be evaluated as follows: The noise acceleration psd of BBN 501 accelerometer is flat over 5-25K Hz, with the total spectral energy of $2.25 \times 10^{-6} \text{ g}^2$. From the ordinate of the noise acceleration psd, $2.25 \times 10^{-6} \text{ g}^2 / 25,000 \text{ Hz}$ or $1.34 \times 10^{-5} (\text{in}/\text{sec}^2)^2 / \text{Hz}$, one finds that $c_1 = 1.34 \times 10^{-5} / (2\pi)^4 = 8.6 \times 10^{-9} \text{ in}^2 / \text{Hz}$. Inserting this into Equation (28) yields

$$\overline{G_{\Delta \theta \Delta \theta}}(f) = \frac{1.72 \times 10^{-8} (S/N)^2}{(\Delta x)^2} f^{-4}. \quad (29)$$

For $(S/N) = 10$ and 10^2 corresponding respectively to **10 db and 20 db**, the reference psd's are drawn in all figures for the angular psd (Figures A7b, A8b-A8f, A9b, A10b, and A11b). Since the accelerometer noise is but one of many noise sources, we shall consider

the $\overline{G_{\theta_{\Delta}\theta_{\Delta}}}(f)$ for (S/N) = 10 db as a total noise floor. Note that all angular psd's lie above the total noise floor in all frequency ranges; hence, the angular spectral measurements are accepted with sufficient confidence. An angular psd can, however, exceed the $\overline{G_{\theta_{\Delta}\theta_{\Delta}}}(f)$ for (S/N) = 20 db only in the high frequency range.

For the effect of variable Δx , let us examine the angular psd's in Figures A8b-A8f. It is seen that the angular psd moves up higher above the reference $\overline{G_{\theta_{\Delta}\theta_{\Delta}}}(f)$ as Δx increases. This means that we are more confident in the angular psd measurement as Δx becomes large. In particular, the angular psd for $\Delta x = 12$ in (Figure A8f) lies well above the $\overline{G_{\theta_{\Delta}\theta_{\Delta}}}(f)$ for (S/N) = 20 db. One cannot, however, increase Δx indefinitely. This is because for some higher-order normal modes there will occur more than one node between the two accelerometers, hence definition (2) becomes meaningless for such normal modes. A way of relating a maximum Δx with the upper frequency limit f^* has been suggested in Reference A1,

$$f^* = \frac{2\pi}{9(\Delta x)^2} \sqrt{\frac{EI}{\rho A}}$$

As seen from Figures A8b-A8f the upper frequency limit decreases from 9146 Hz to 1016 Hz as Δx increases from 4 in to 12 in.

2. The Linear and Angular Vibration RMS Amplitudes

For the overall measure of vibration energy, the psd's are integrated upwards from the frequency of 40 Hz to compute the rms values which are summarized in Table A2. The low frequency limit is well below the primary frequency and high enough to block out the background noise. In Columns I and II, the rms values of $y(x_1)$ and $y(x_2)$ are given for Test Nos. 1-8.

The arithmetic means of Columns I and II are shown in Column III, and the linear vibration rms amplitudes predicted by NASTRAN are given in Column IV. The values of Columns III and IV are plotted in Figure A13 as a function of x . Just as $\sin^2(\pi x/L)$ of the theoretical beam (Equation 14), one finds that the NASTRAN model predicts monotonically increasing linear rms values towards the midspan. Except the irrationally high value at $x = 27$ in, the experimental rms values also seem to increase towards the midspan.

Next, the experimental angular rms values are given in Column V, and the computed values by NASTRAN at the center location are shown in Column VI. Figure A13 compares the experimental $(\theta_{\Delta})_{\text{rms}}$ for $\Delta x = 4$ in with the NASTRAN results to show spatial distribution on the beam. Although $(\theta_{\Delta})_{\text{rms}}$ falls off towards the midspan, it does not become zero as theoretically predicted by Equation 14 under the localized midspan excitation. It has been shown that the beam-averaged $(\theta_{\Delta})_{\text{rms}}$ is related to the beam-averaged y_{rms} by (Equation 32 in Reference 1 of the main text)

$$(\theta_{\Delta})_{\text{rms}} = \left[\frac{2 \sin(\pi \Delta x / 2L)}{\Delta x} \right] y_{\text{rms}}. \quad (30)$$

Using the average of Column III, $y_{\text{rms}} = 0.19 \times 10^{-3}$, Equation (30) for $\Delta x = 4$ in gives $(\theta_{\Delta})_{\text{rms}} = 0.83 \times 10^{-5}$ rad. which is larger than the local measurements as shown in Figure A13.

Test No.	x_c (in)	I	II	III	IV	V	VI
		$(y_1)_{rms} \times 10^3$ (in)	$(y_2)_{rms} \times 10^3$ (in)	$\frac{(y_1)_{rms} + (y_2)_{rms}}{2}$ (in)	NASTRAN $(y)_{rms} \times 10^3$ (in)	$(\theta_{\Delta})_{rms} \times 10^5$ (rad)	NASTRAN $(\theta_{\Delta})_{rms} \times 10^5$ (rad)
1	19	0.188	0.155	0.172	0.170	0.759	0.692
2	27	0.219	0.202	0.211	0.20	0.62	0.616
3	27	0.23	0.206	0.218	-	0.654	-
4	27	0.187	0.165	0.176	-	0.483	-
5	27	0.225	0.188	0.207	-	0.516	-
6	27	0.193	0.156	0.175	-	0.478	-
7	32	0.193	0.178	0.186	0.201	0.491	0.401
8	36	0.188	0.181	0.185	0.212	0.328	0.220

Table A2. The Linear and Angular Vibration RMS Values.

V. Conclusions

To verify the relationship between the linear and angular response psd's, a simply supported beam was excited at the midspan to generate a constant psd of linear acceleration response on the beam. The overall consistency of linear and angular spectral measurements was demonstrated by numerically simulating the beam experiment with a NASTRAN finite-element model which has reproduced the spectral details with sufficient realism.

Some pertinent conclusions may be summarized as follows:

- (1) Angular spectral measurements are not affected by whether the accelerometer signals are instantaneously differenced at the time of data acquisition or digitally differenced later from the recorded signals. This, of course, presupposes the maintenance of amplitude and phase calibrations of the accelerometers.
- (2) The angular spectral measurements are well above a noise floor psd which is defined as ten times the noise floor of a typical accelerometer. Hence, the differential angular psd's are accepted with confidence.
- (3) From the local rms values of linear and angular vibration, it is inferred that the simply supported end condition and the localized midspan excitation are not observed by the experimental beam. Certainly, the added masses of shaker armature and MHD sensor further contribute to the divergence of experiment from the theoretical beam analyzed in Section II of the main text.

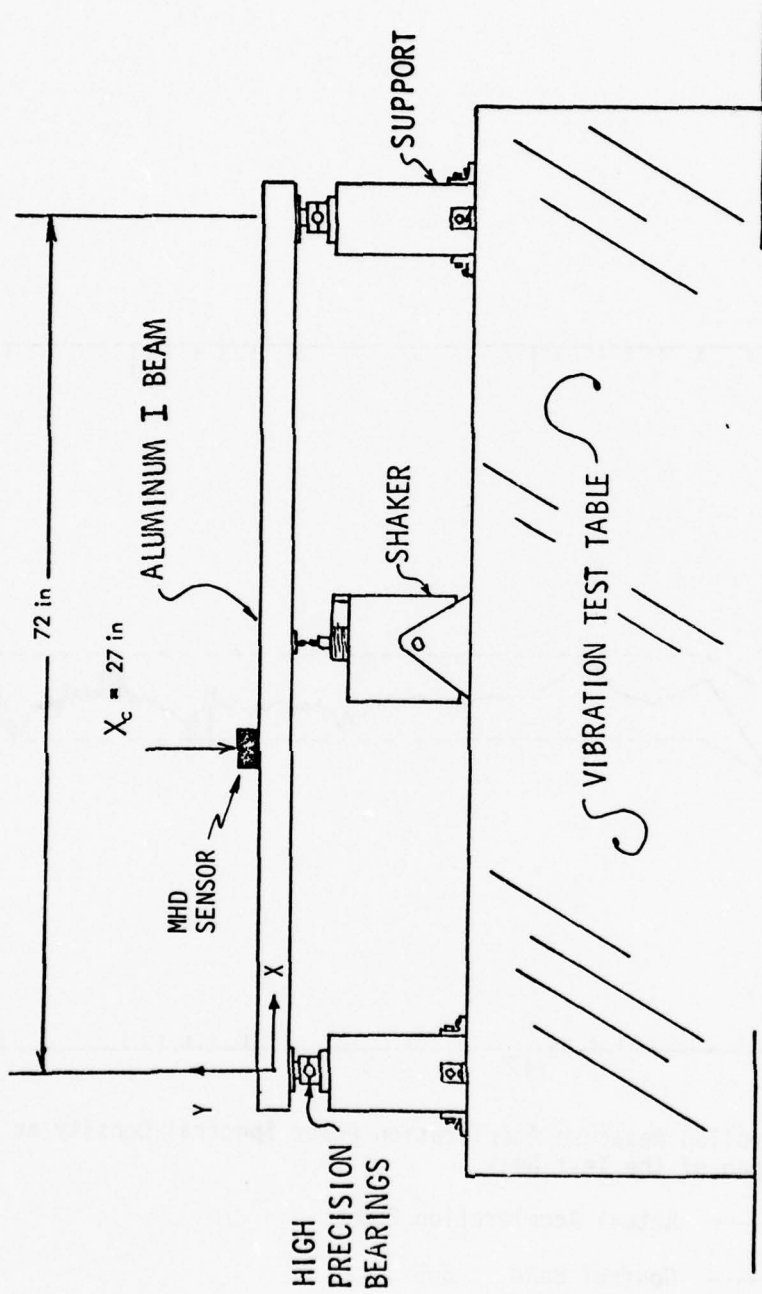


Figure A1. Beam Experimental Configuration

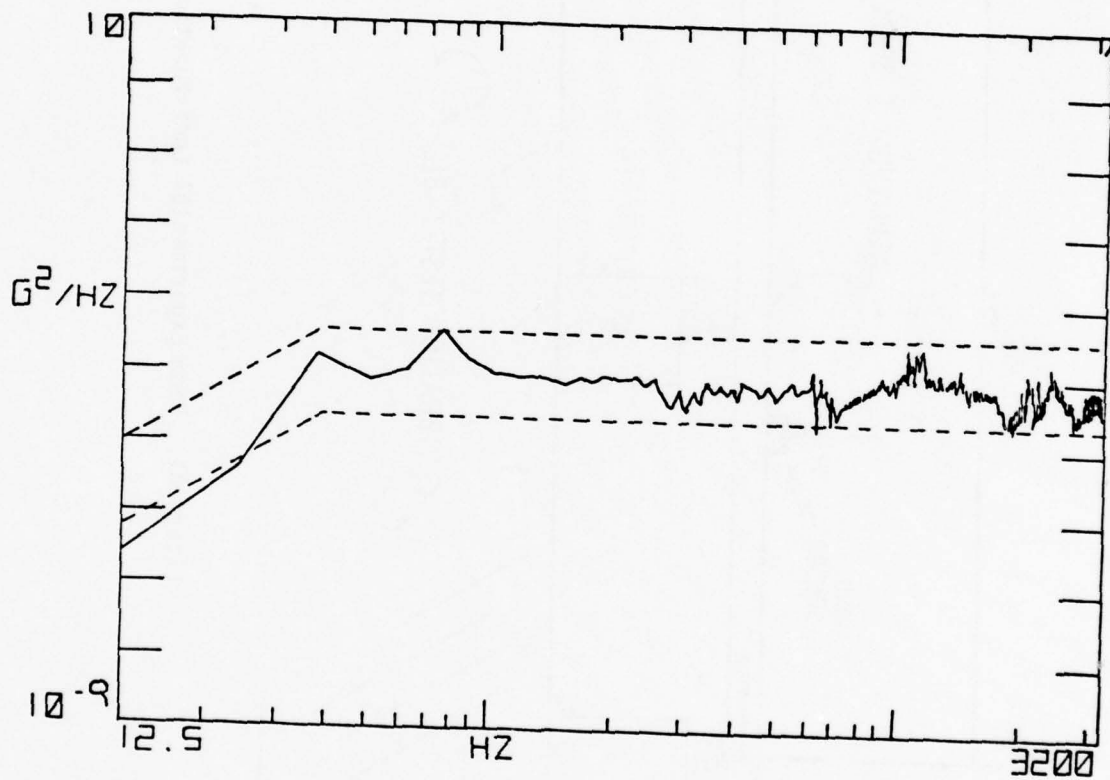


Figure A2. Controlled Response Acceleration Power Spectral Density at the Midspan of the Test Beam

— Actual Acceleration PSD ;
 - - - Control Band ± 6 dB

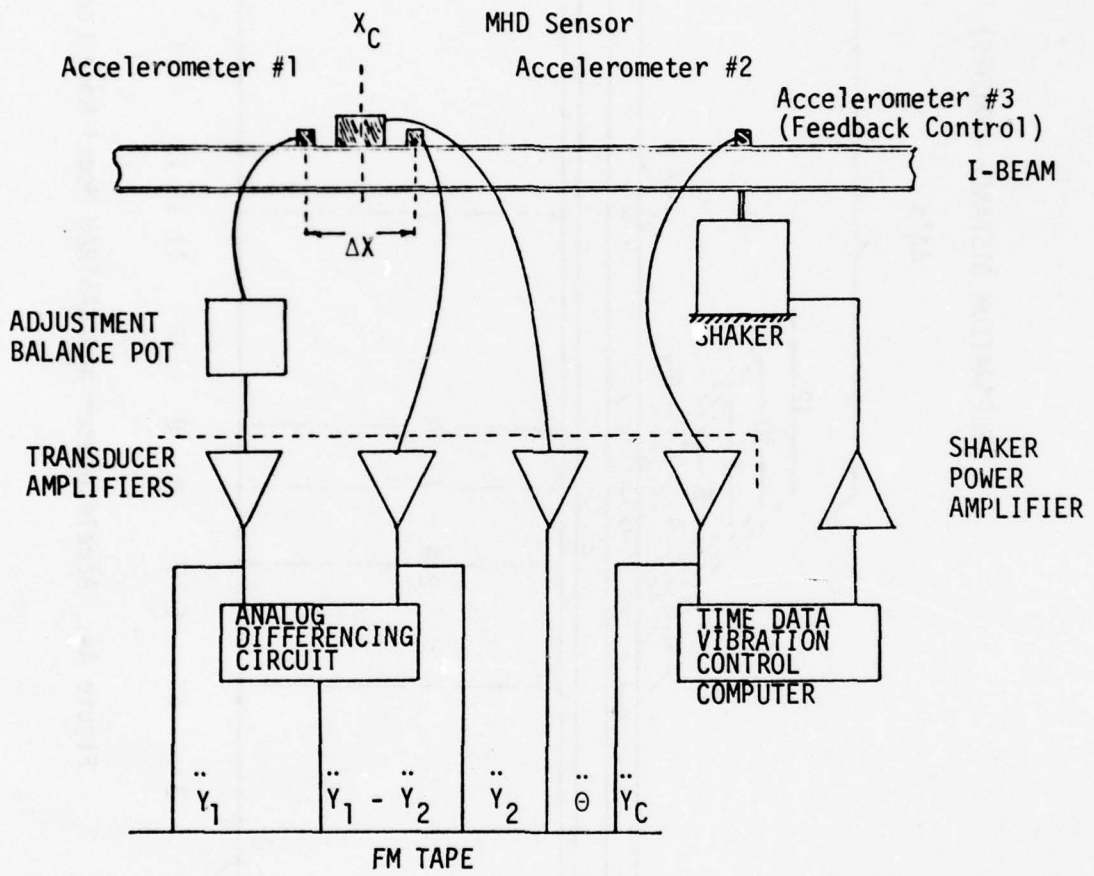
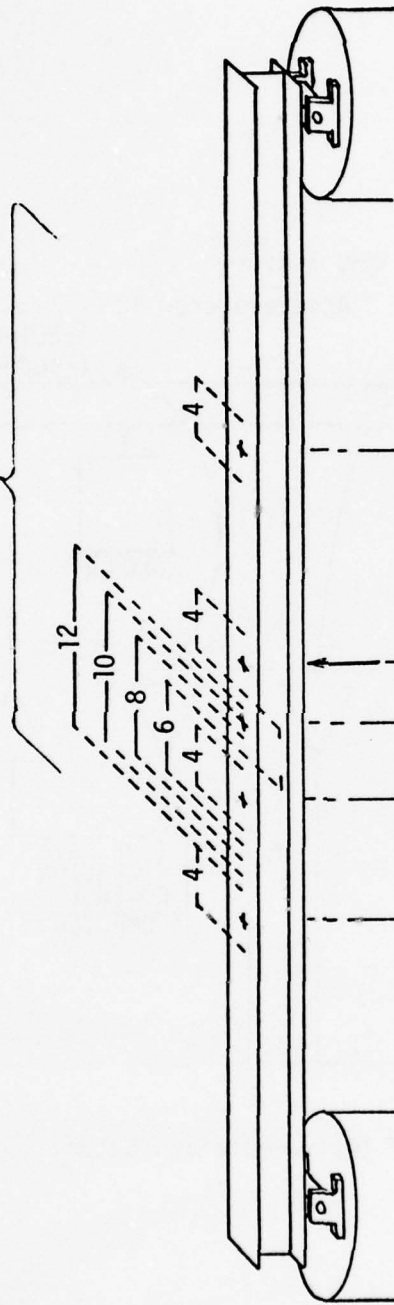


Figure A3. Schematic of Instrumentation Setup

SEPARATION DISTANCE (INCHES)

ΔX 's

I-BEAM TEST



TEST NUMBER

NASTRAN MODEL

NODE NUMBER

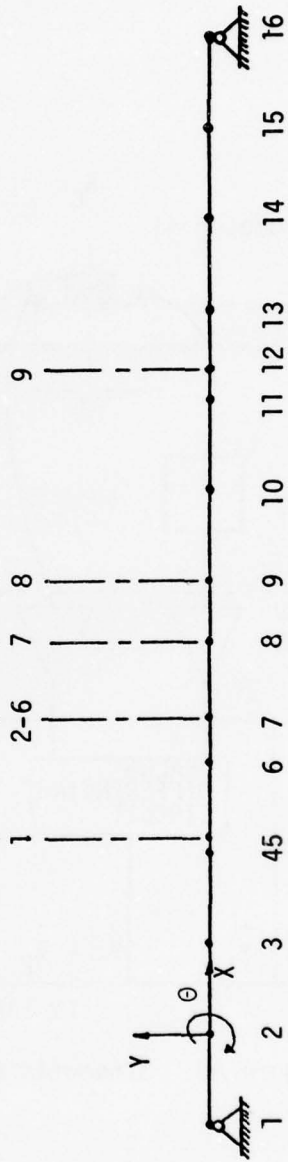


Figure A4. Accelerometer and NASTRAN Model 1 Node Locations

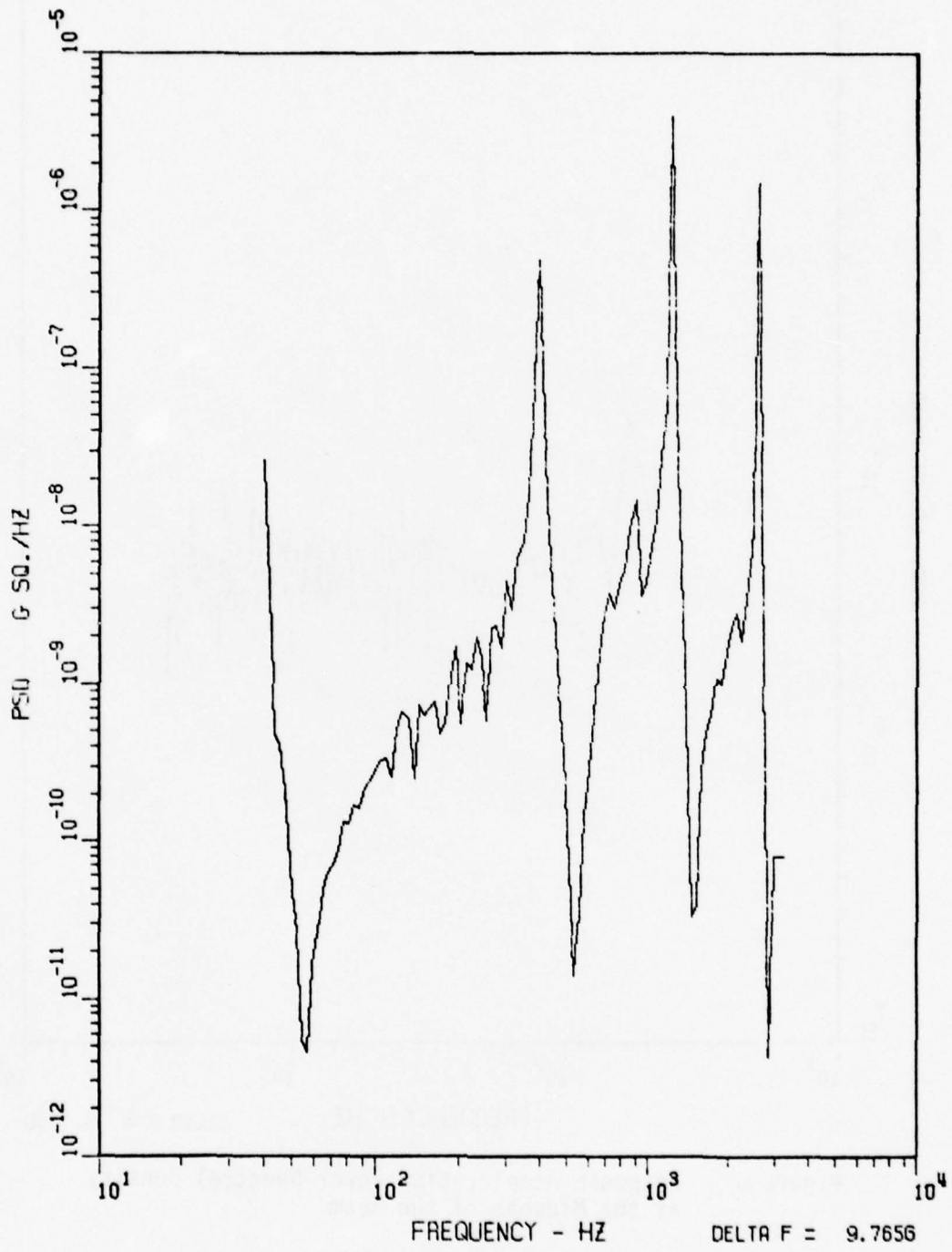


Figure A5. Typical Forcing Power Spectral Density of the NASTRAN Model at the Midspan of the Beam

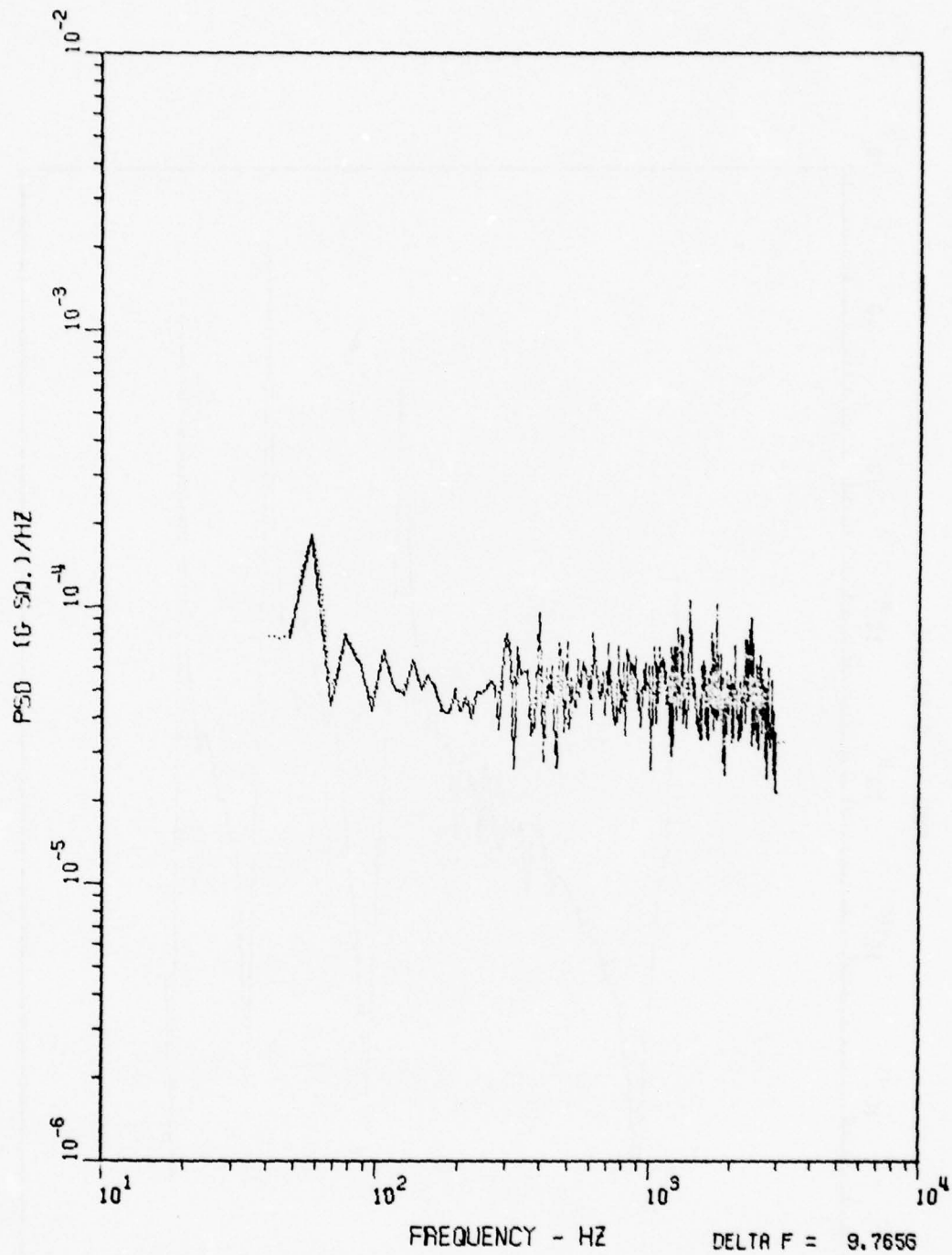


Figure A6. Response Acceleration Power Spectral Density at the Midspan of the Beam

————— Measured ;
 - - - - - NASTRAN

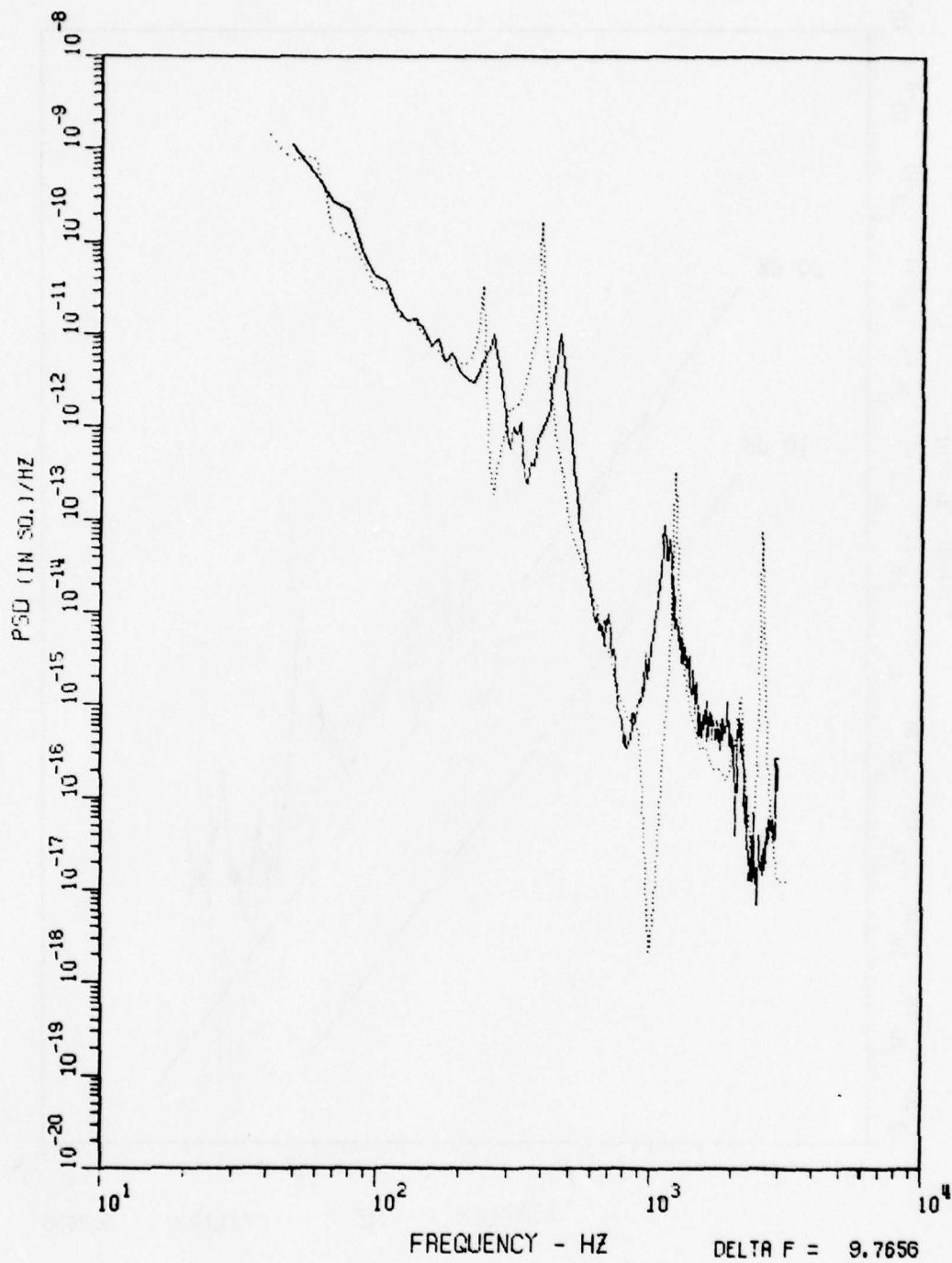


Figure A7a. Linear Power Spectral Density of Test No. 1

———— Measured ;
 - - - - - NASTRAN

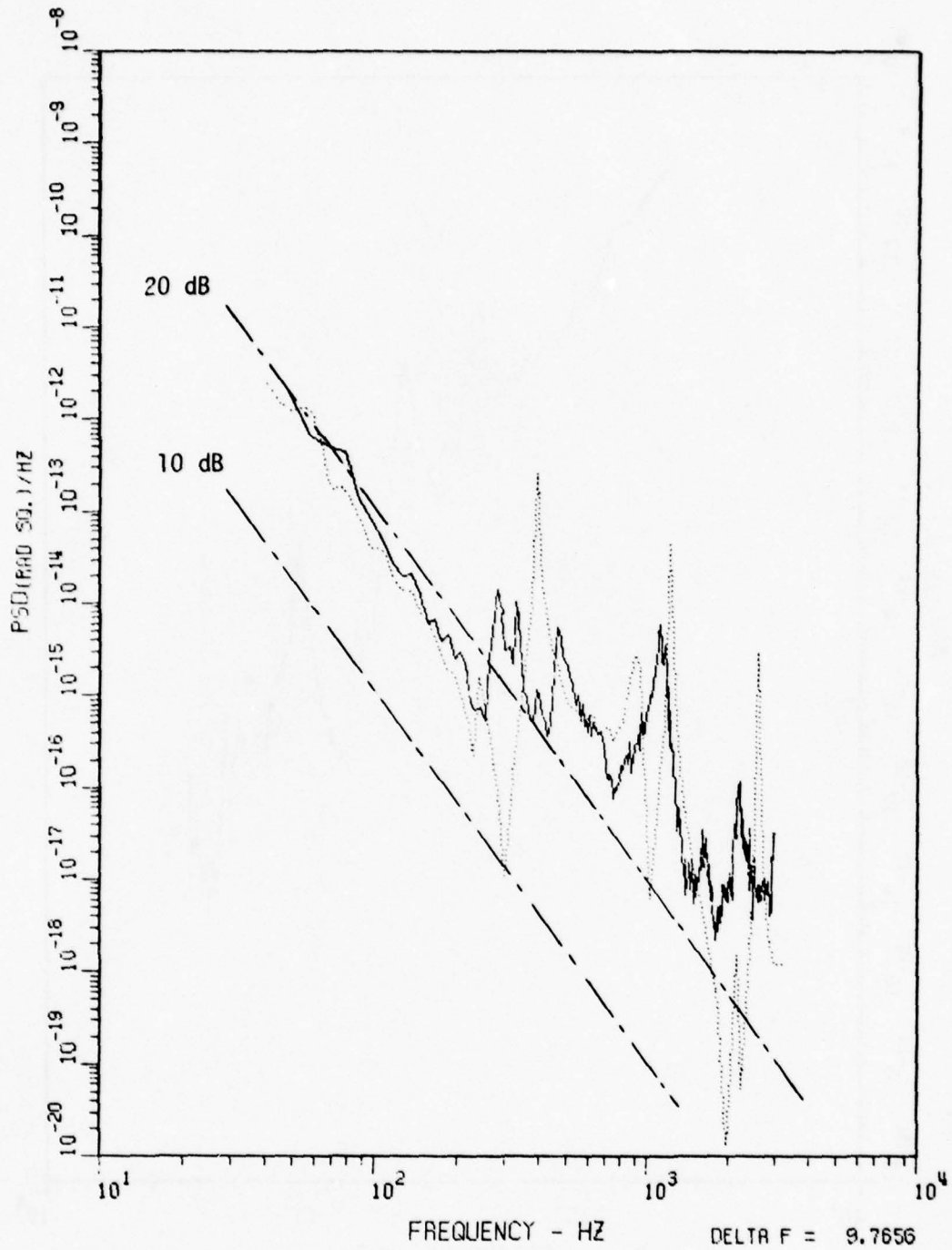


Figure A7b. Angular Power Spectral Density of Test No. 1,
 $\Delta X = 4$ in., $X_C = 19$ in.

———— Measured ;
 NASTRAN

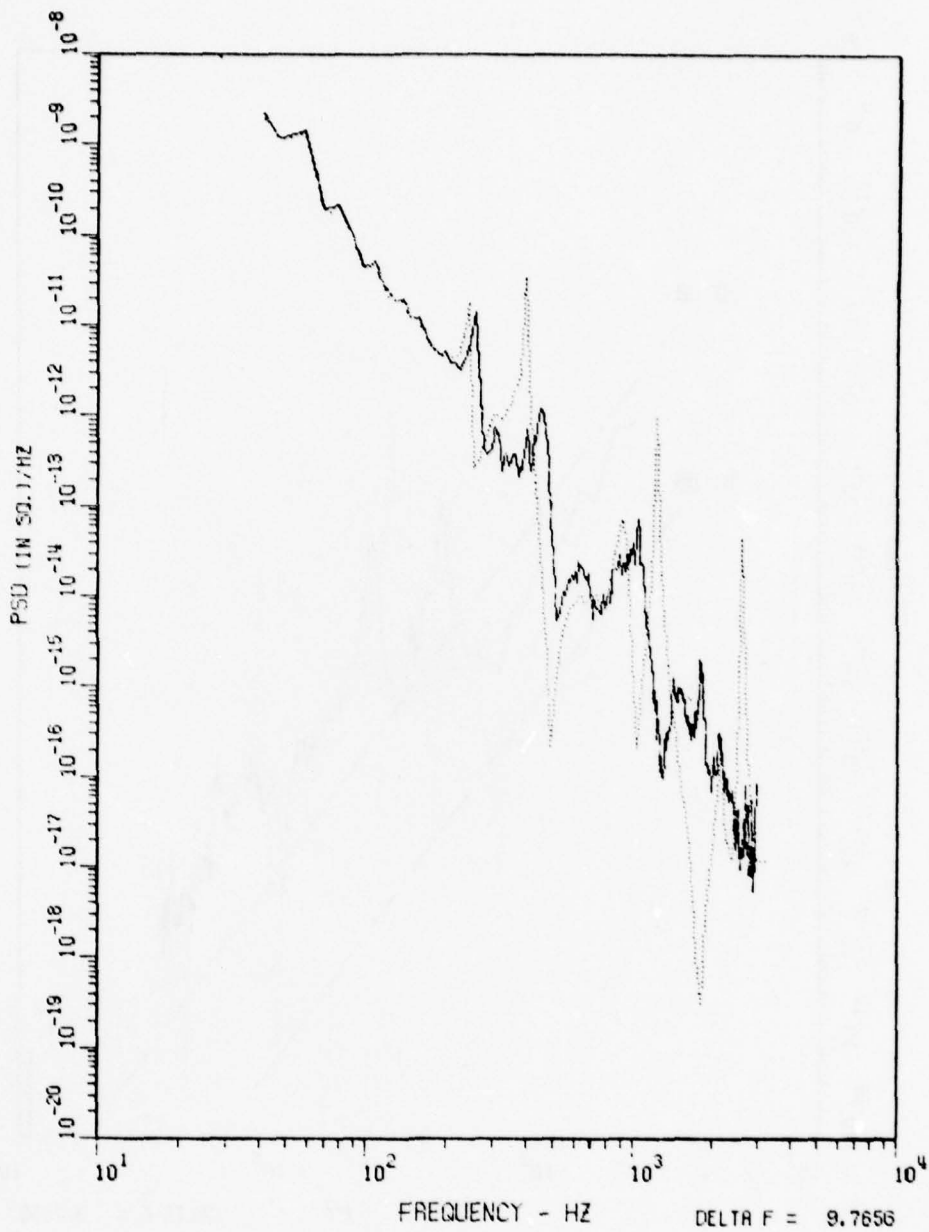


Figure A8a. Linear Power Spectral Density of Test No. 2

———— Measured ;
..... NASTRAN

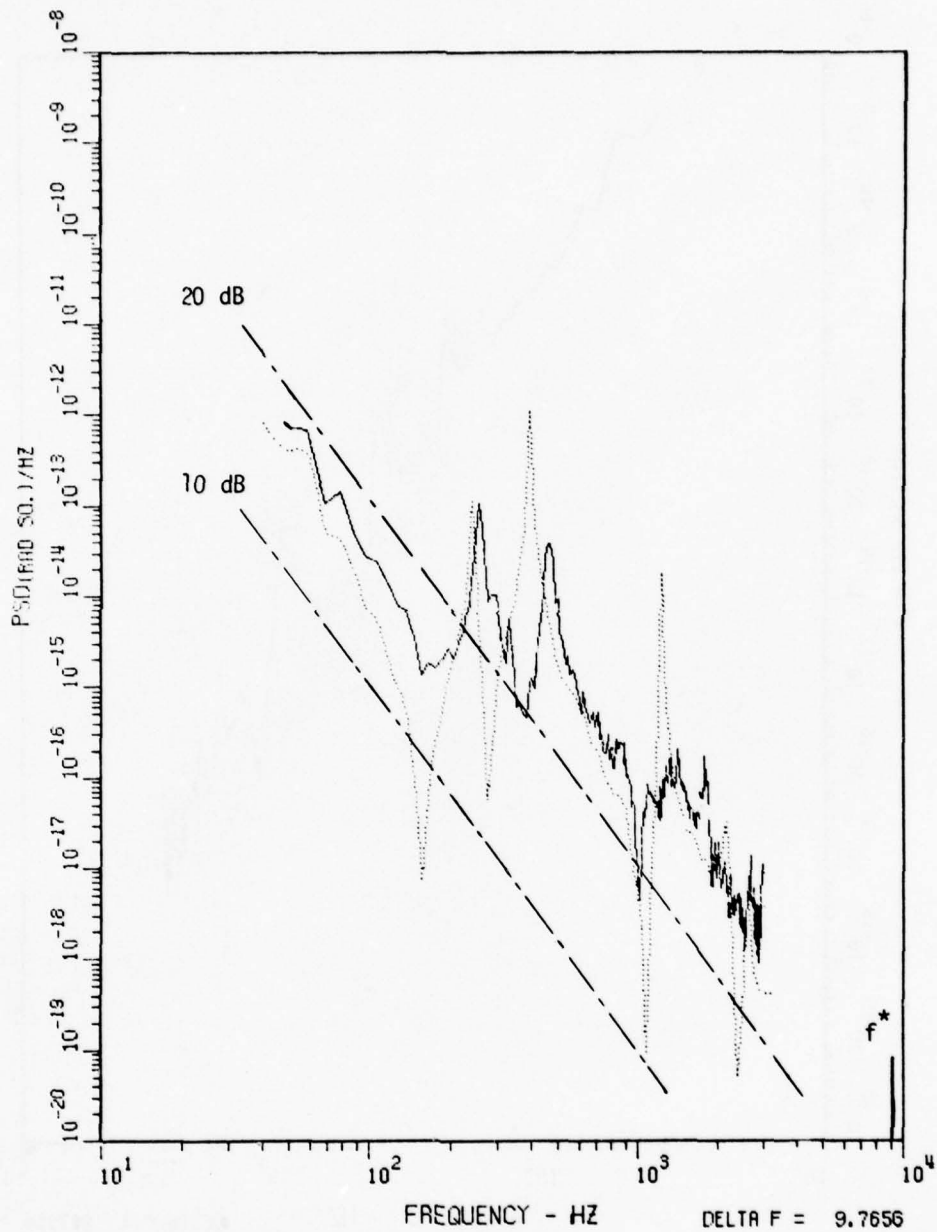


Figure A8b. Angular Power Spectral Density of
 Test No. 2, $\Delta X = 4$ in., $X_C = 27$ in.

———— Measured ;
 NASTRAN

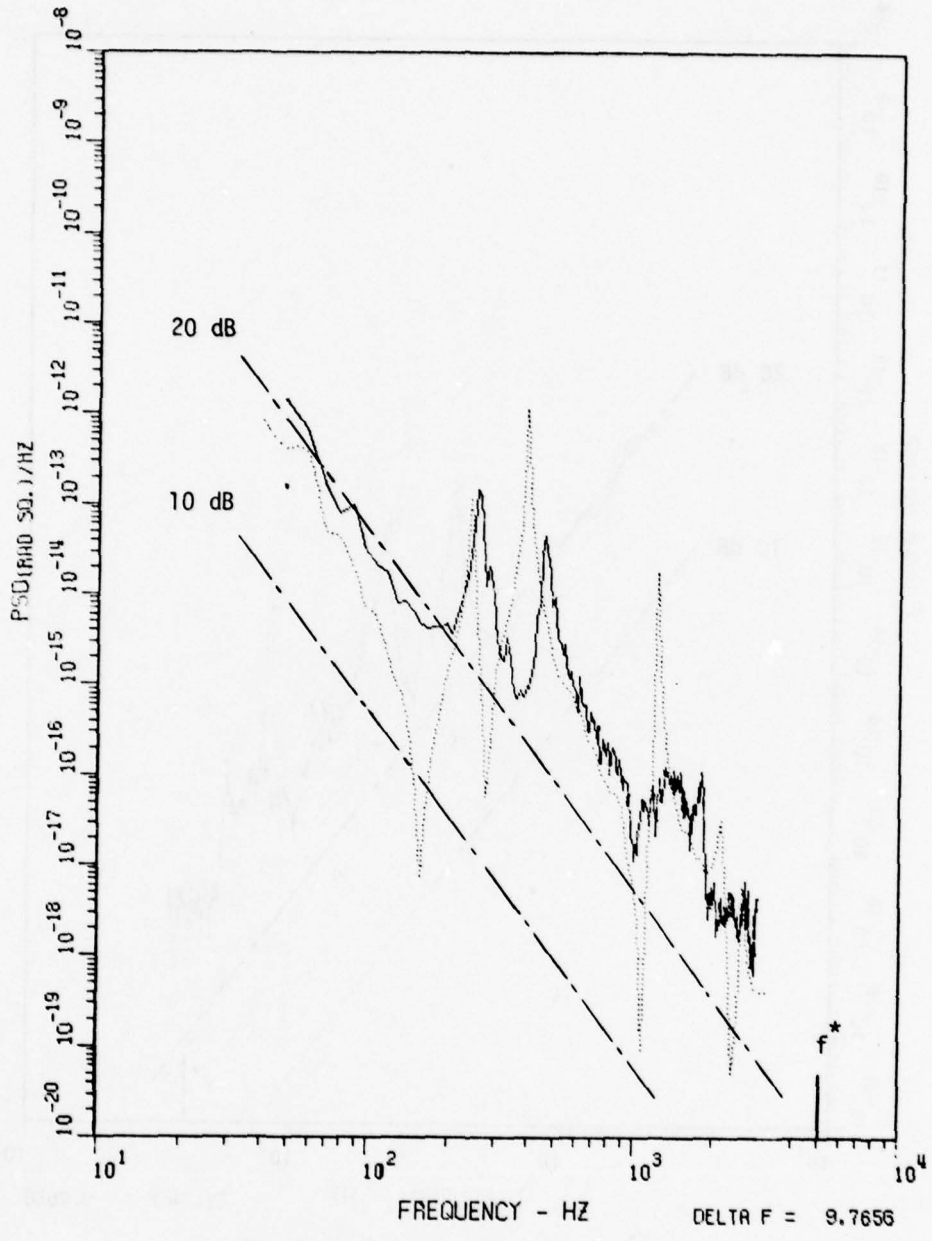


Figure ARc. Angular Power Spectral Density of
 Test No. 3, $\Delta X = 6$ in., $X_C = 27$ in.

———— Measured ;
 NASTRAN

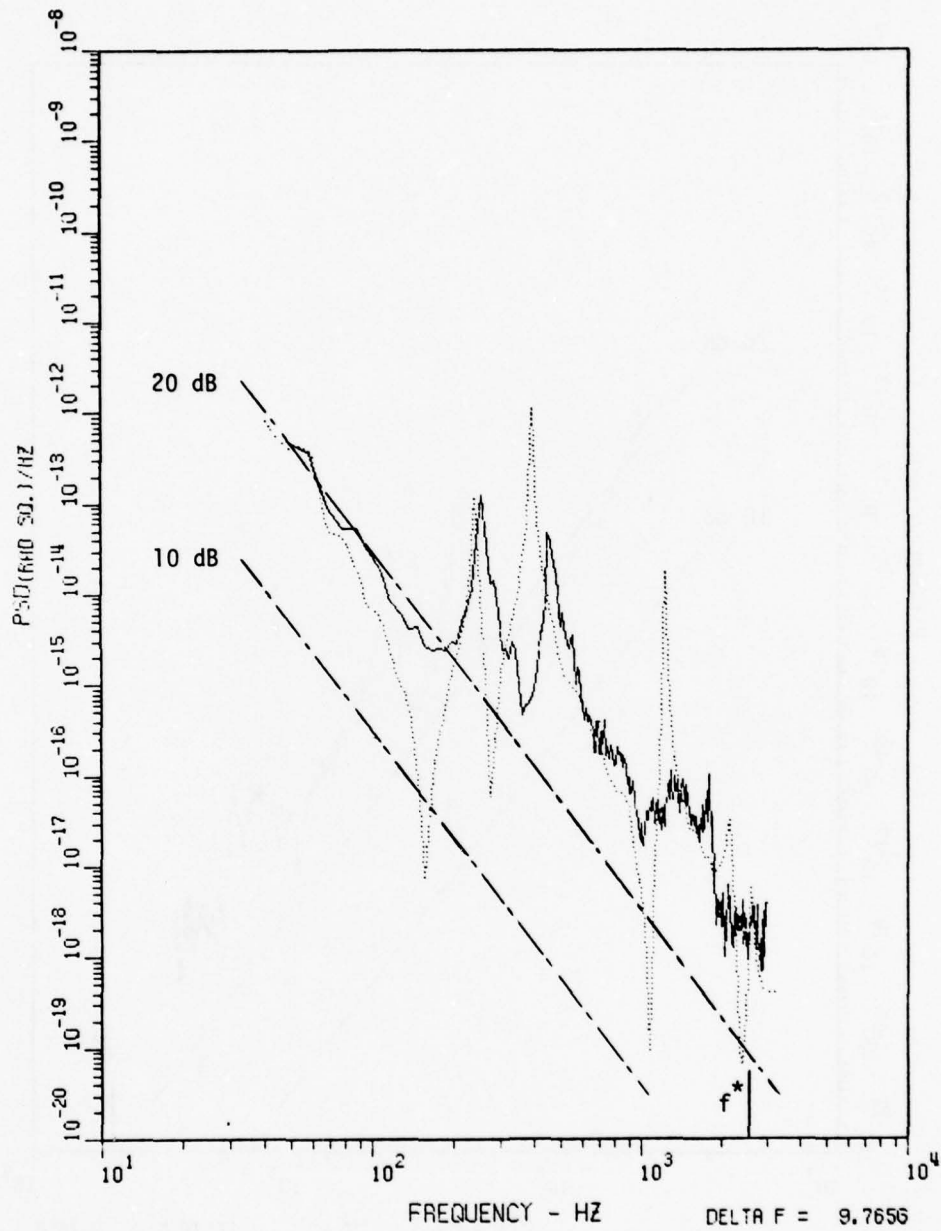


Figure A8d. Angular Power Spectral Density of
 Test No. 4, $\Delta X = 8$ in., $X_C = 27$ in.

———— Measured ;
 NASTRAN

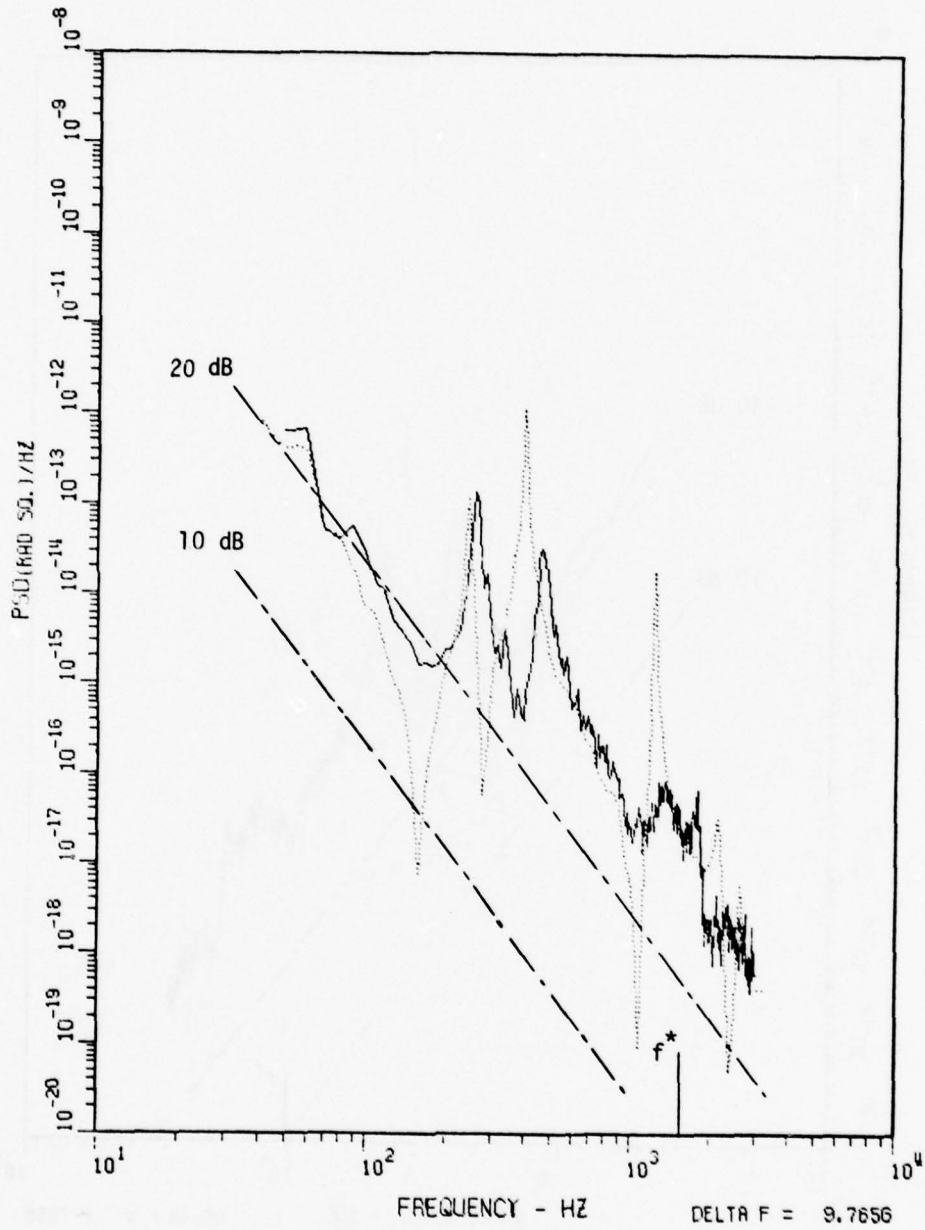


Figure A8e. Angular Power Spectral Density of
 Test No. 5, $\Delta X = 10$ in., $X_C = 27$ in.

— Measured ;
 NASTRAN

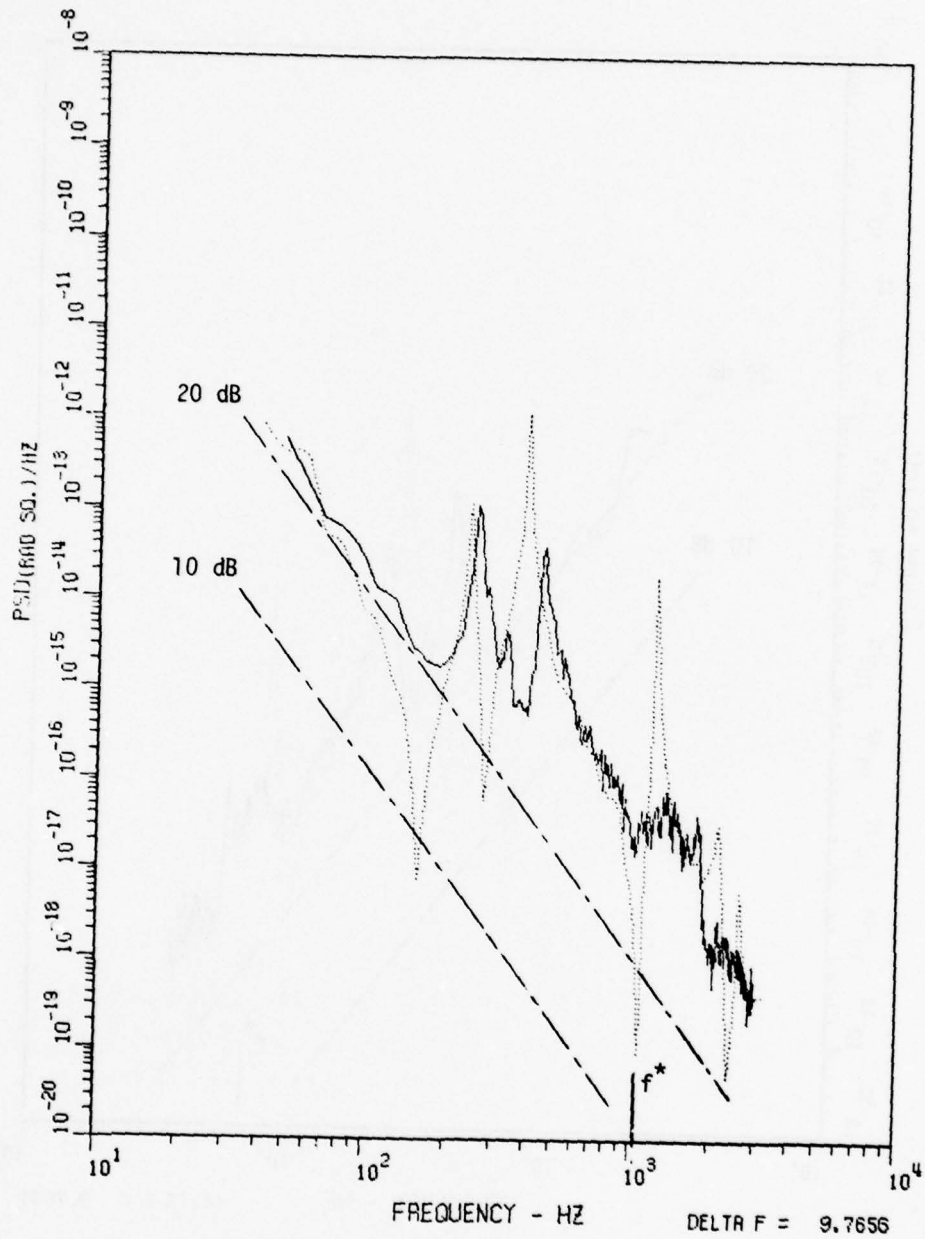


Figure A8f. Angular Power Spectral Density of
 Test No. 6, $\Delta X = 12$ in., $X_C = 27$ in.

———— Measured ;
 NASTRAN

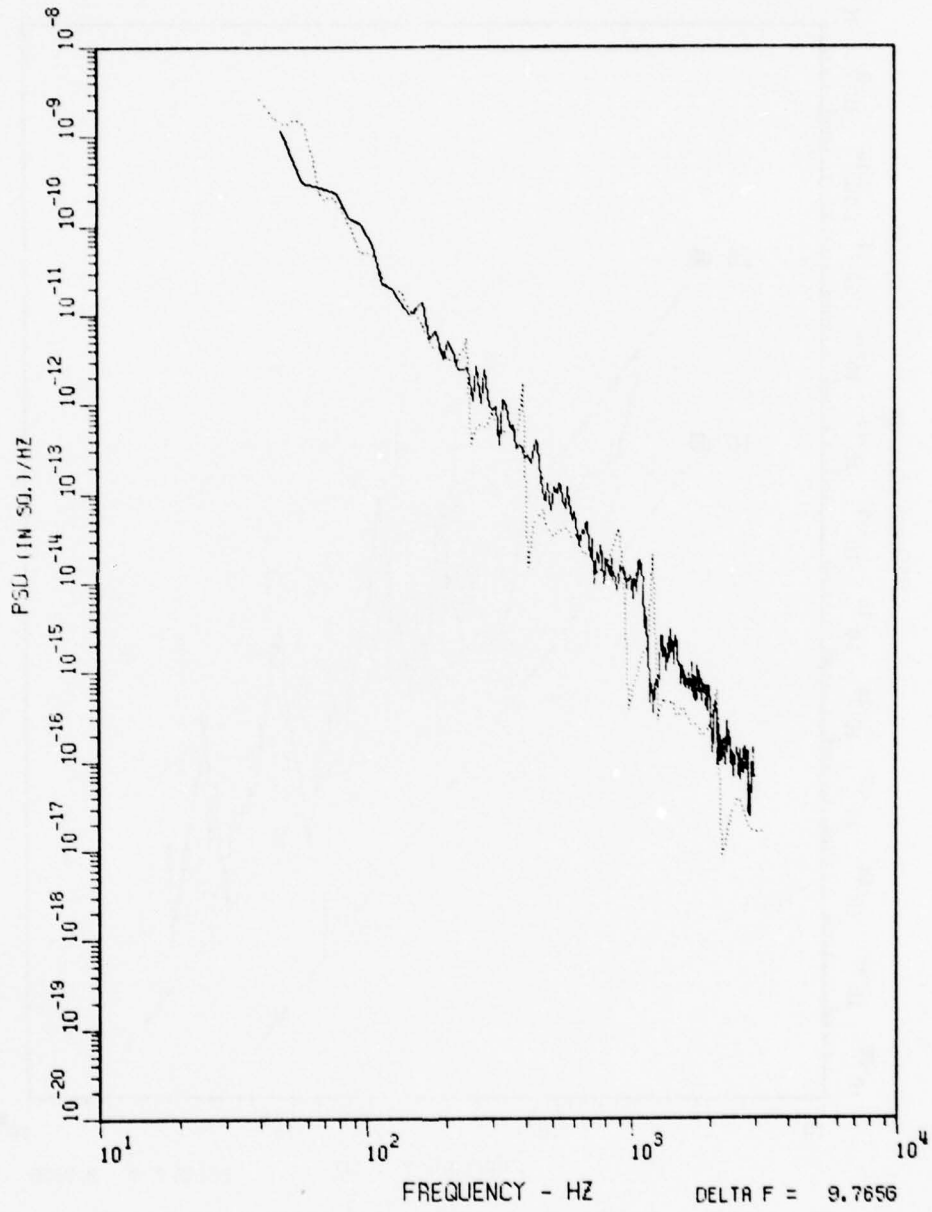


Figure A9a. Linear Power Spectral Density of Test No. 7

———— Measured ;

..... NASTRAN

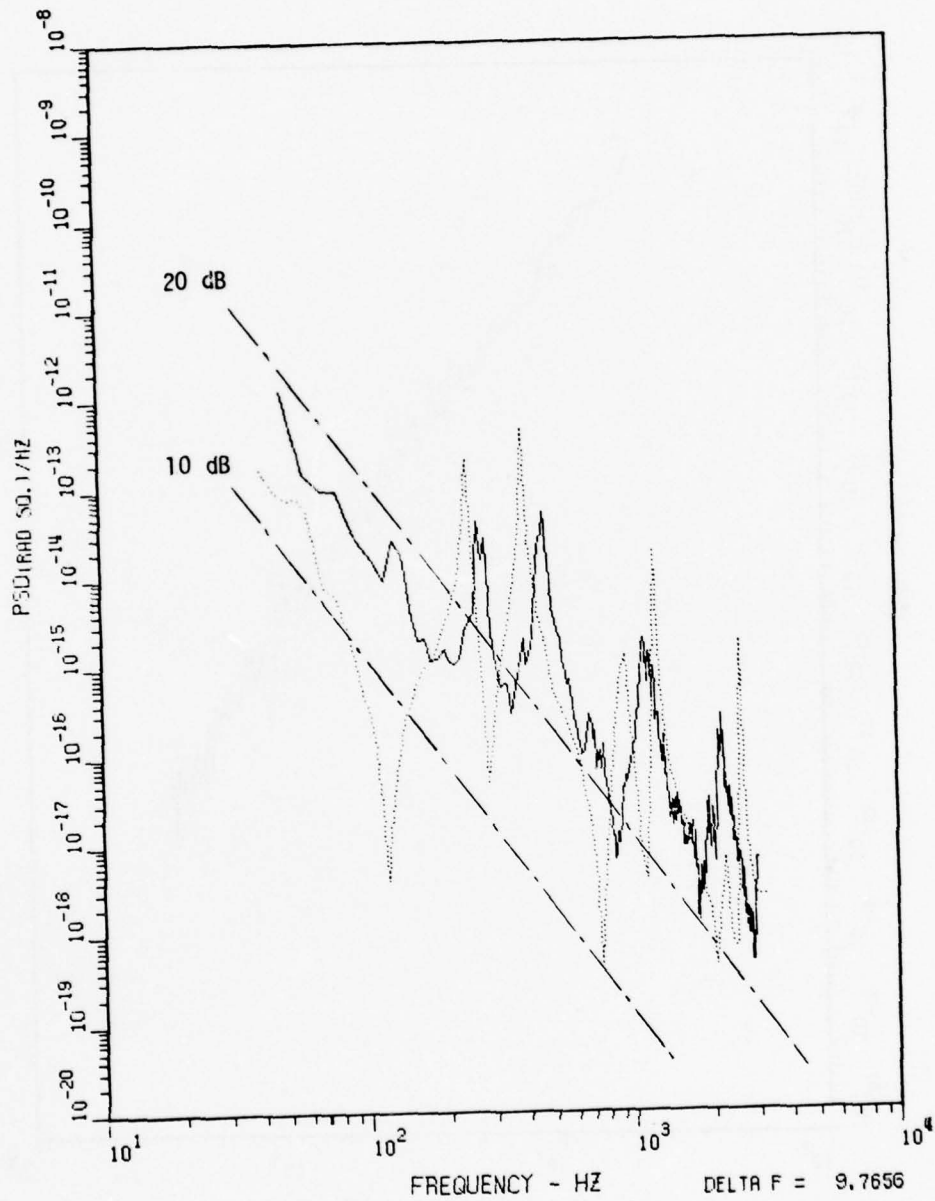


Figure A9b. Angular Power Spectral Density of
 Test No. 7, $\Delta X = 4$ in., $X_C = 32$ in.

———— Measured ;
 NASTRAN

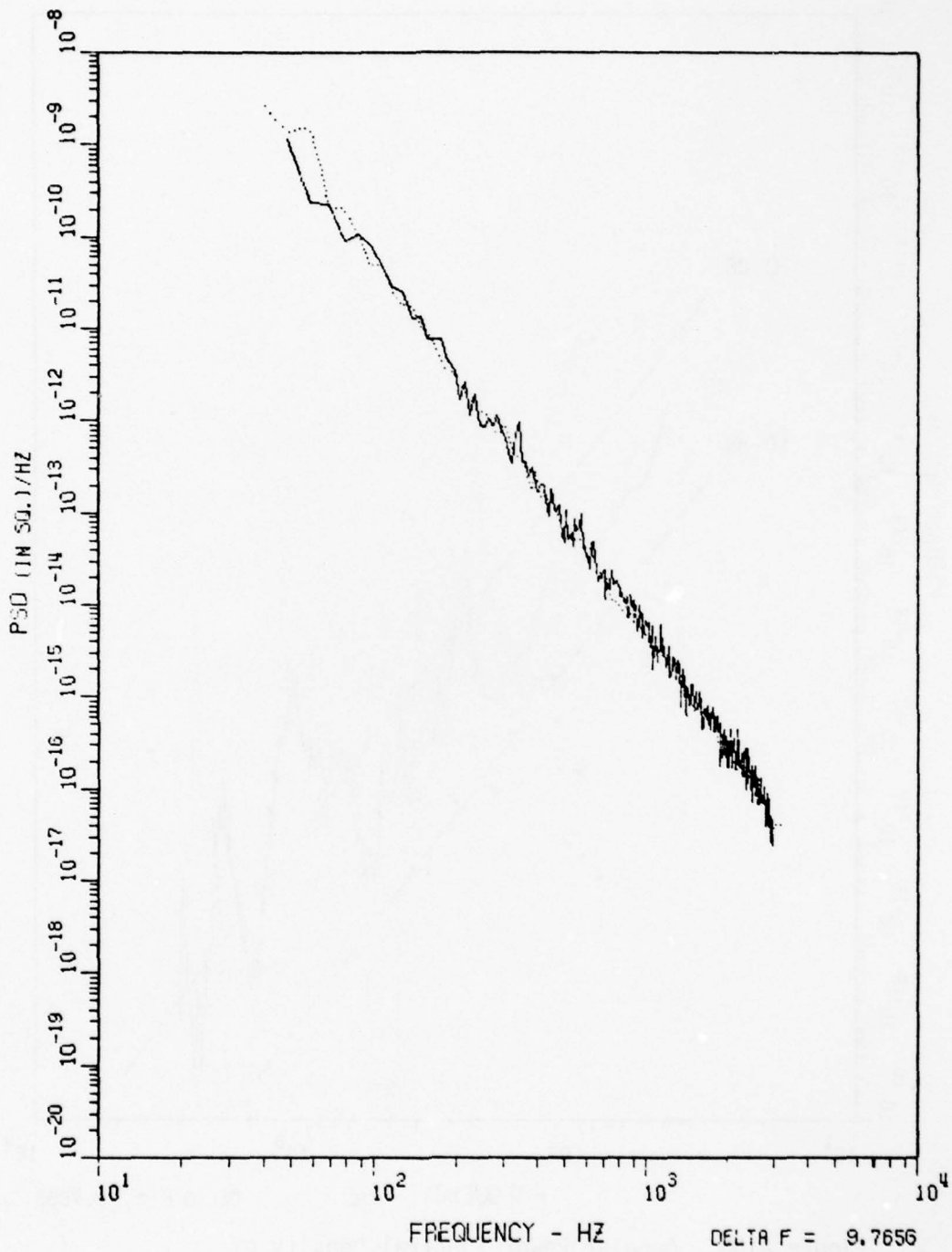


Figure A10a. Linear Power Spectral Density of Test No. 8

———— Measured ;

..... NASTRAN

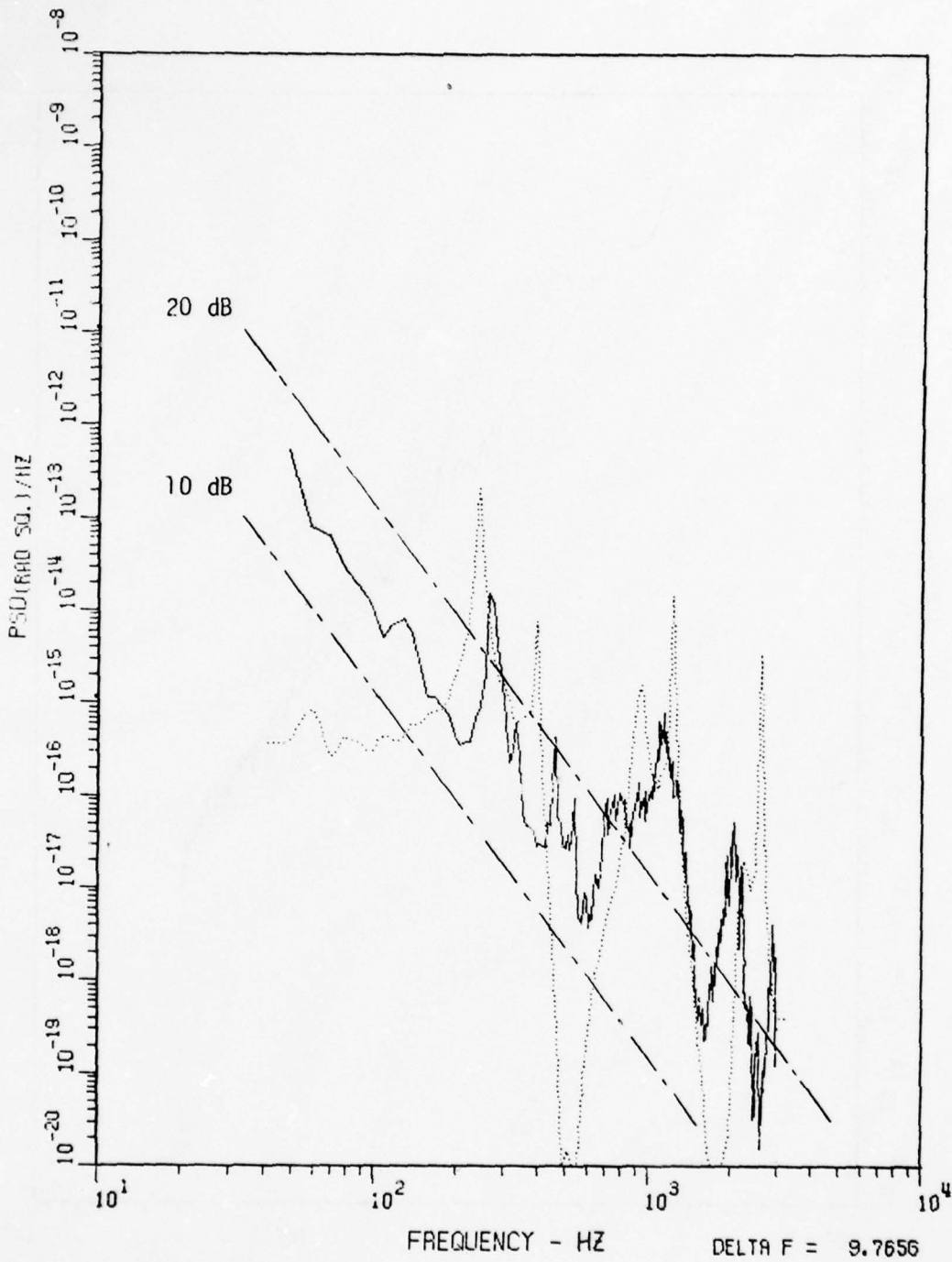


Figure A10b. Angular Power Spectral Density of
 Test No. 8, $\Delta X = 4$ in., $X_C = 36$ in.

———— Measured ;
 NASTRAN

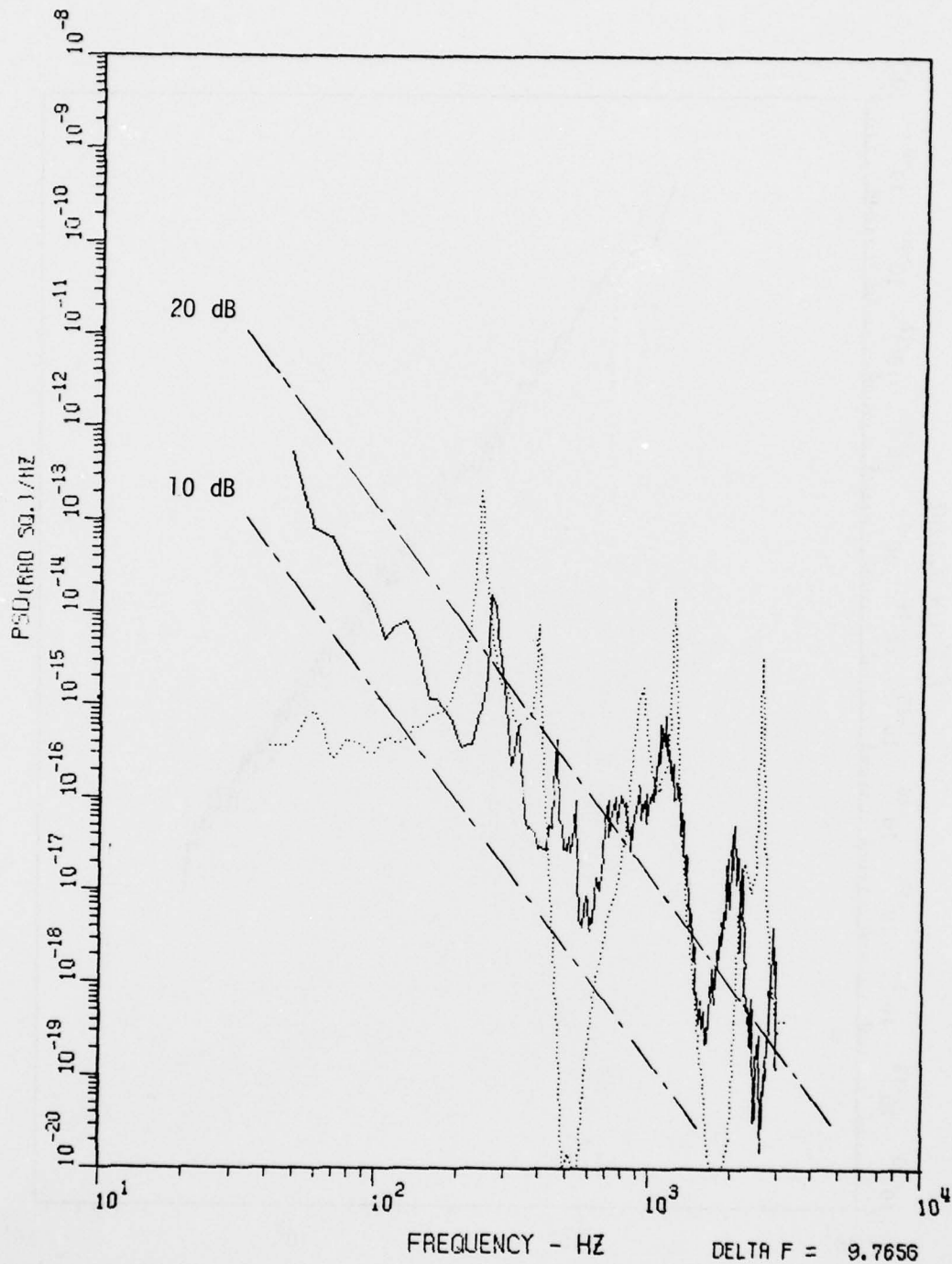


Figure A10b. Angular Power Spectral Density of
 Test No. 8, $\Delta X = 4$ in., $X_C = 36$ in.

———— Measured ;
 NASTRAN

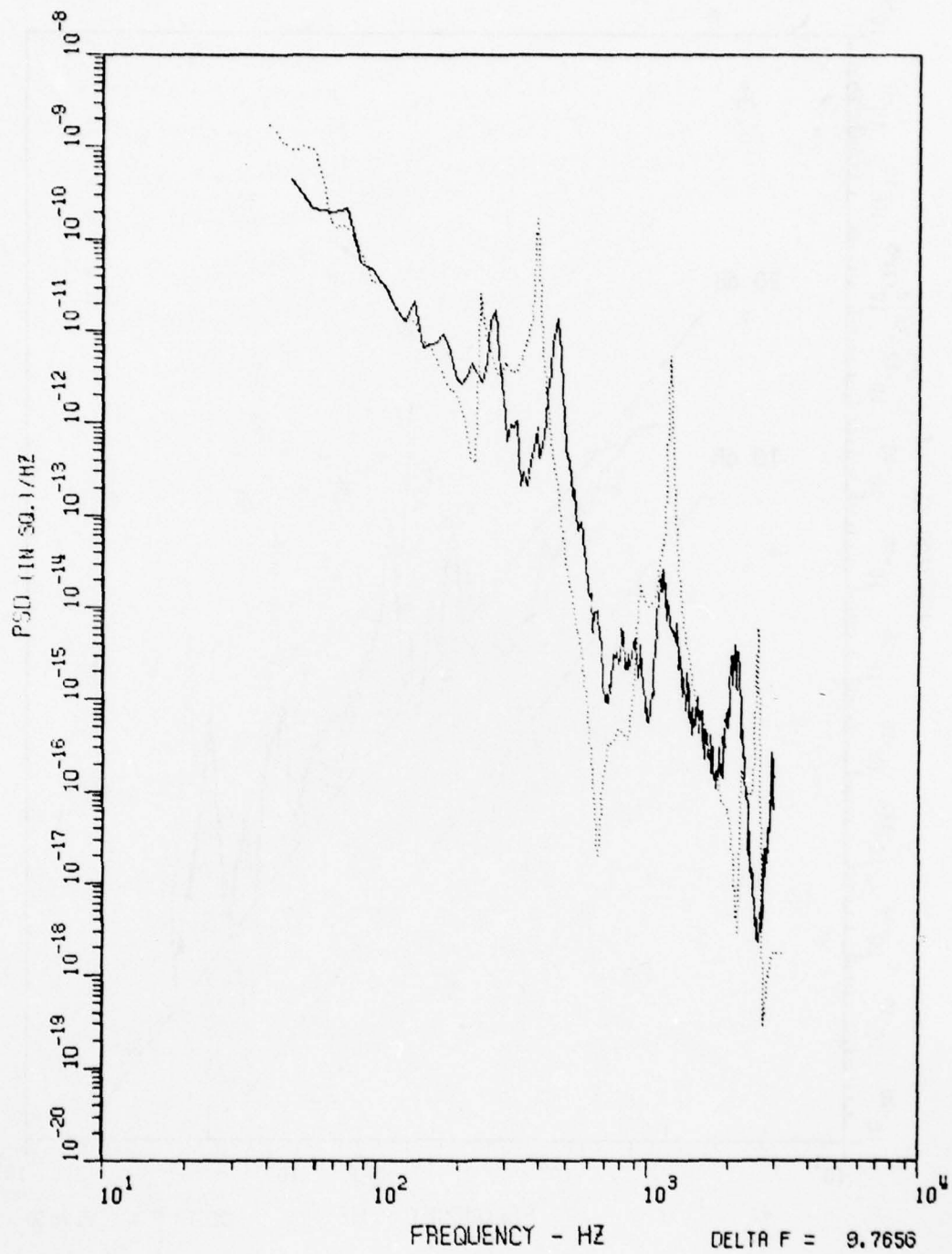


Figure All.a. Linear Power Spectral Density of Test No. 9

———— Measured ;
 NASTRAN

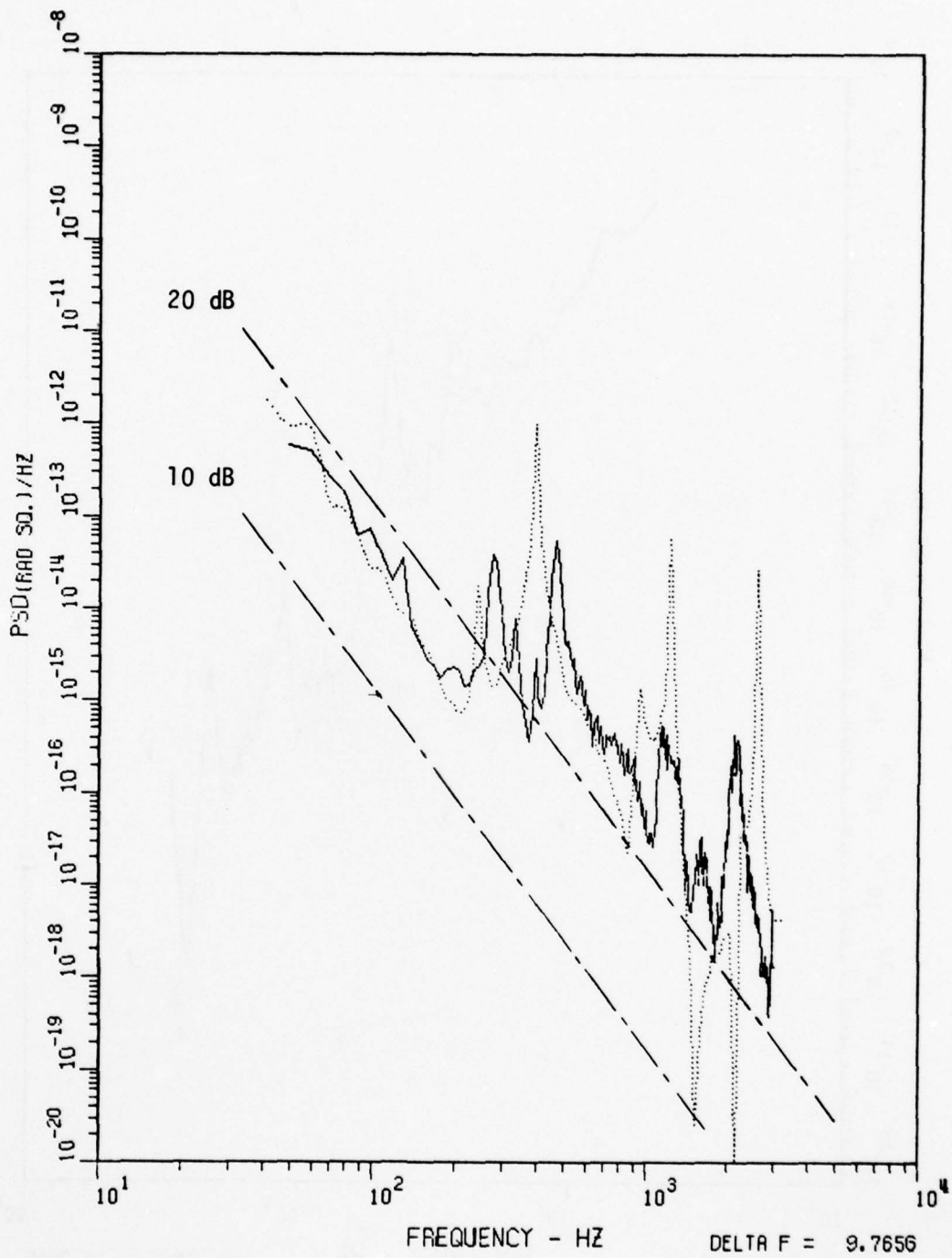


Figure A11b. Angular Power Spectral Density of
 Test No. 9, $\Delta X = 4$ in., $X_C = 50$ in.

———— Measured ;
 NASTRAN

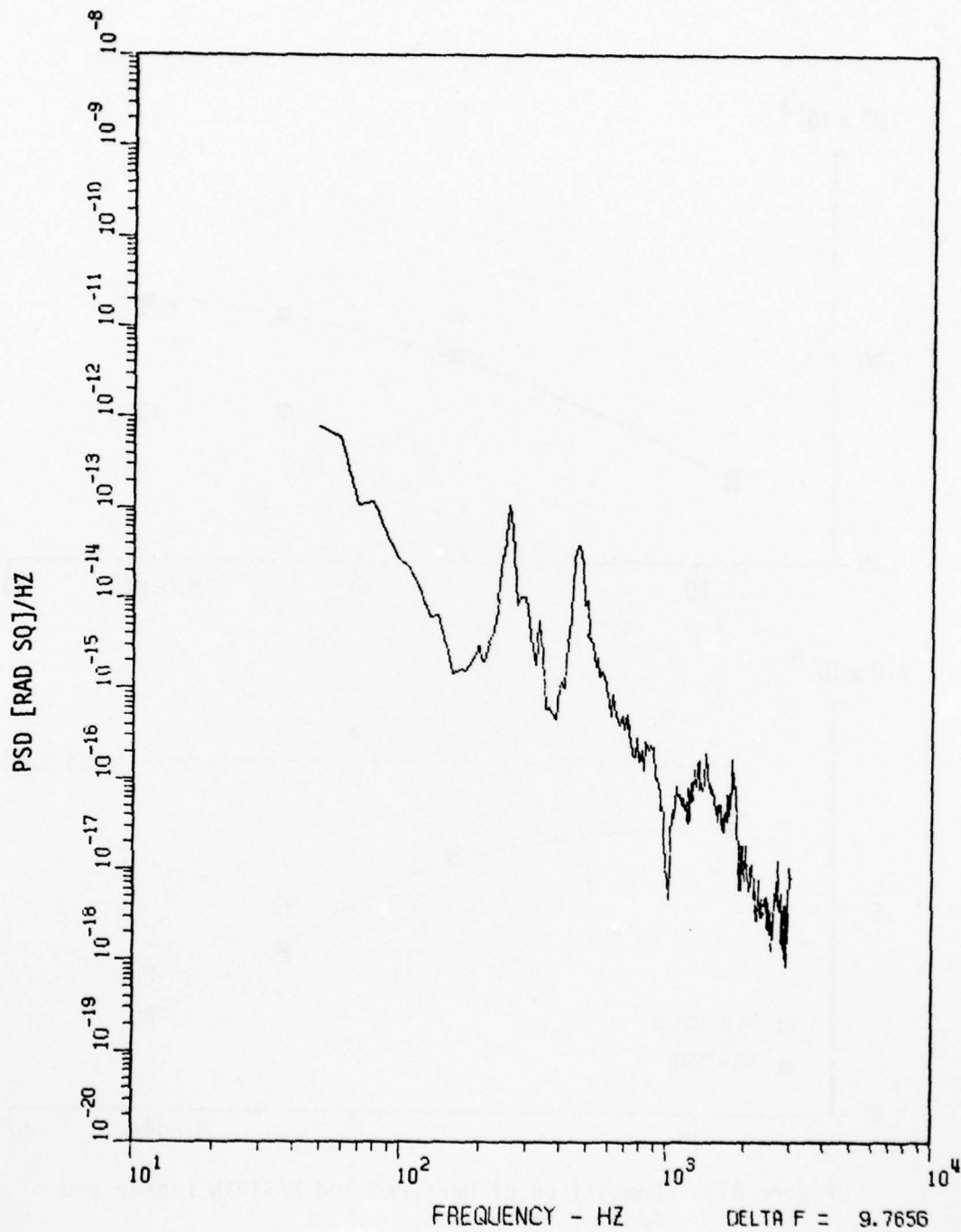


Figure A12. Digitally Differenced Angular Power Spectral Density of Test No. 2

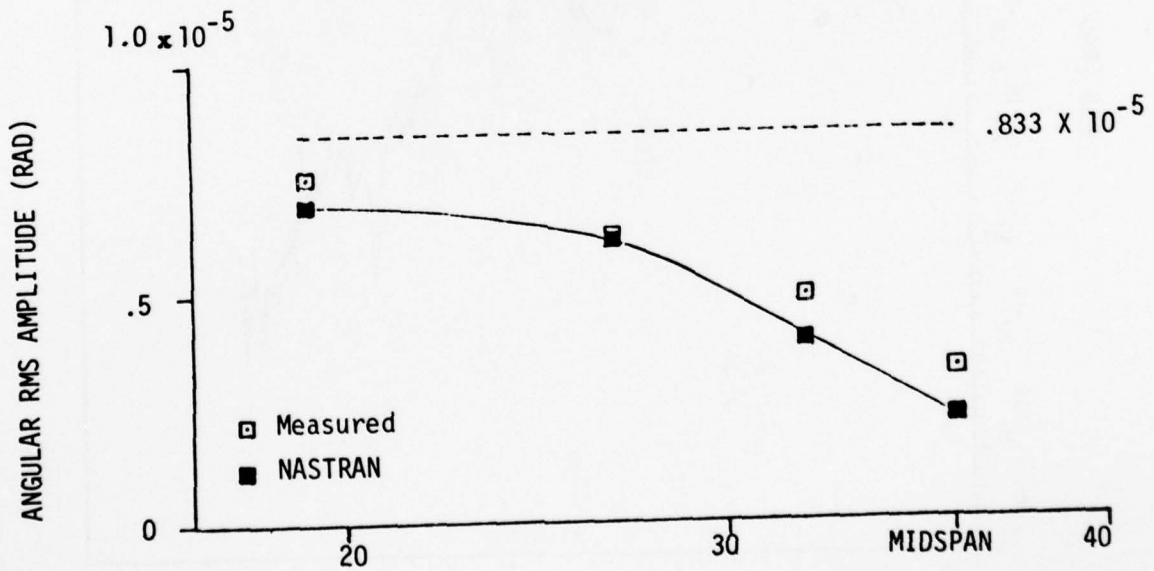
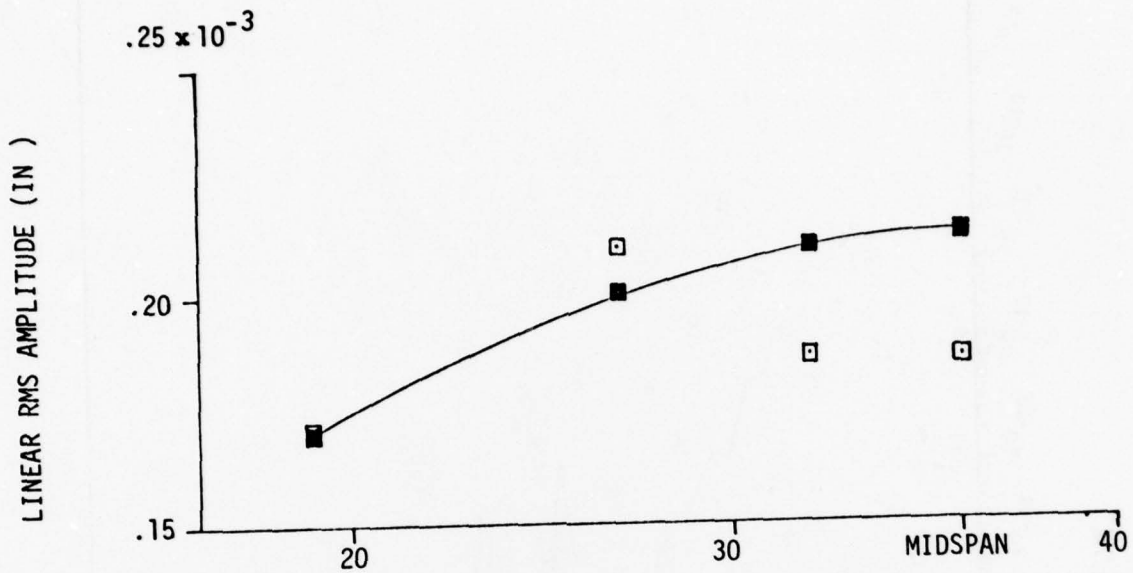


Figure A13. Comparison of Measured and NASTRAN Linear and Angular RMS Values

REFERENCES

- A1. Whaley, P. W., and Obal, M. W., "Measurement of Angular Vibration using Conventional Accelerometers," The Shock and Vibration Bulletin 47, Part 3, 97-107, September 1977.
- A2. MacNeal, R. H., Ed., The NASTRAN Theoretical Manual (Level 15), Software Management and Information Center, University of Georgia, Athens, Georgia, April 1972.
- A3. MacNeal, R. H., Ed., The NASTRAN User's Manual (Level 16.0), Software Management and Information Center, University of Georgia, Athens, Georgia, March 1976.
- A4. Johnson, C., and Gibson, W., Inputting Prescribed Accelerations in NASTRAN, ASIAC Report No. 975.1A, Anamet Laboratories, Inc., San Carlos, Calif., September 1975.

APPENDIX B

THE DETERMINATION OF STRUCTURAL DAMPING CONSTANTS

As an input to the NASTRAN code, the structural damping constants of the simply supported beam were determined by a Time/Data **Vibration Control and Analysis** computer via the Modal Analysis and Modeling Systems (MODAMS) software package. The MODAMS program extracts viscous damping information from the transfer function observed at a point on the structure subject to the impact excitation at another point. The equivalent viscous damping coefficients estimated by MODAMS for the first five resonance frequencies are listed in Table B1:

Mode No.	Resonance frequency	Viscous damping coefficient
1	76.9	0.0374
2	265	0.014
3	615	--
4	1302	0.0215
5	1421	0.00055

Table B1. Viscous damping coefficients

The MODAMS program failed to produce the damping value of the third mode and predicted the fourth resonance frequency, which is too large. A typical output of MODAMS is shown in Figure B1, which depicts a peak of the transfer function magnitude about the resonance frequency of 265 Hz.

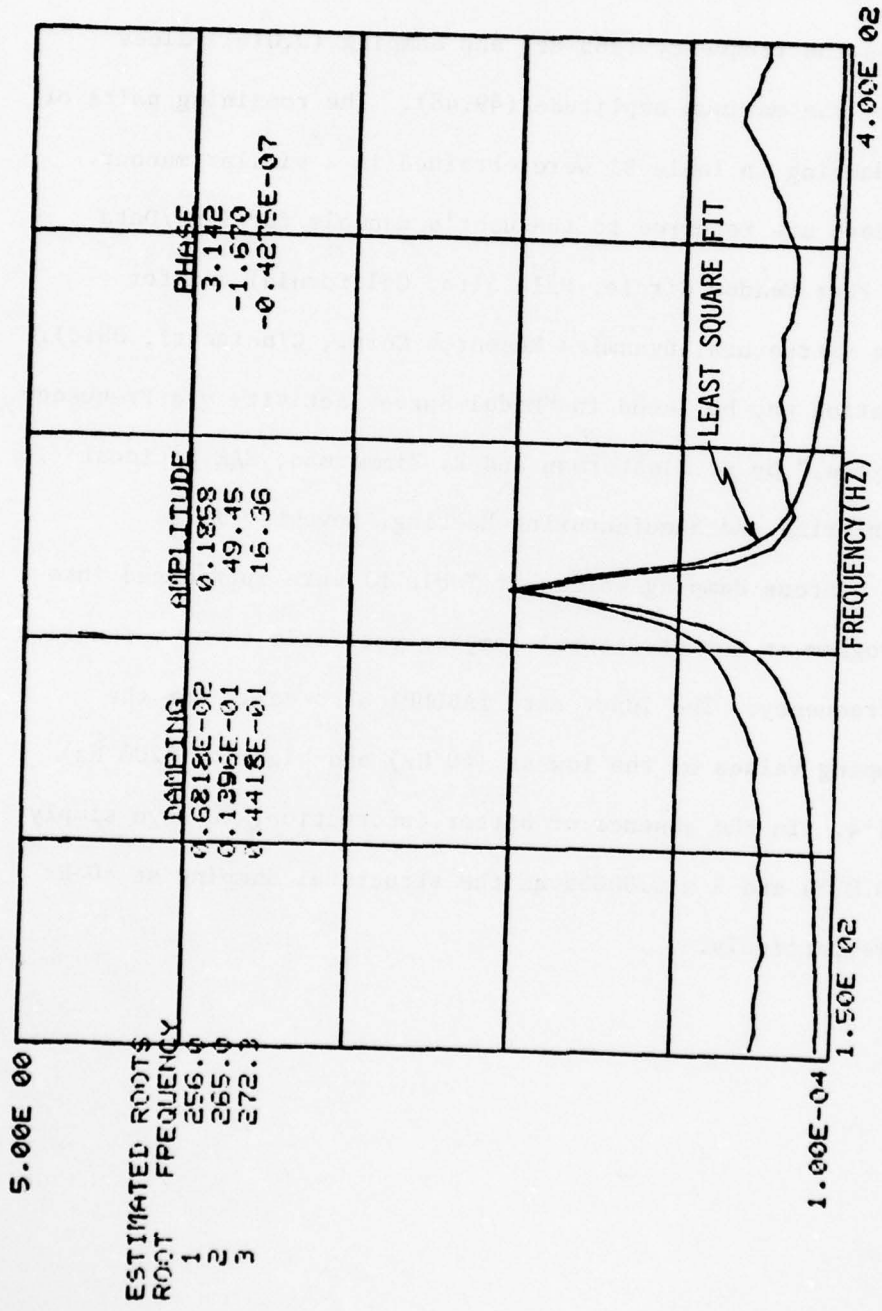


Figure B1. Transfer Function Magnitude About the 2nd Mode of the Test I-Beam

The algorithm of MODAMS generates several damping values from a least-squares fit of the transfer function magnitude as shown in the figure. One then chooses the frequency (265 Hz) and damping (0.014) values corresponding to the maximum amplitude (49.48). The remaining pairs of frequency and damping in Table B1 were obtained in a similar manner. Interested readers are referred to the user's manuals for Time/Data computer (1050 Fast Meadow Circle, Palo Alto, California) and for MODAMS software (Structural Dynamics Research Corp., Cincinnati, Ohio). Further information may be found in "Modal Survey Activity via Frequency Response Functions," by A. Klosterman and R. Zimmerman, SAE National Aerospace Engineering and Manufacturing Meeting, November 1975.

Twice the viscous damping values of Table B1 were introduced into the NASTRAN program as the structural damping coefficients as a function of resonance frequency. The input card TABDMP1 also calls for the structural damping values of the lowest (40 Hz) and highest (3200 Hz) frequency limits. In the absence of better information, we have simply assigned 2×0.0374 and 2×0.00055 as the structural damping at 40 Hz and 3200 Hz, respectively.

APPENDIX C

THE NASTRAN FINITE-ELEMENT COMPUTER PROGRAM

The NASTRAN finite-element code was used because of its extensive application in the dynamic response analyses of aircraft structures. Of the many NASTRAN solution formats, we have used the NASTRAN solution 11,0 for the present stationary random dynamic analysis. The NASTRAN computer listings of the test beam are shown in Tables C1 - C4. Tables C1 and C2 are respectively the executive and input/output controls, and Tables C3 and C4 are the finite-element model parameters and prescribed forcing psd input at the midspan of the beam, respectively.

THIS PAGE IS BEST QUALITY PRACTICABLE
FROM COPY FURNISHED TO DDC

NOVEMBER 25, 1977 NASTRAN 9416/74 PAGE 1

NASTRAN EXECUTIVE CONTROL DECK ECHO

ID 1 BEAM TEST
APP DISPLACEMENT
SOL 11.0
TIME 5
-CEND

TABLE C1. EXECUTIVE CONTROL OF FORMAL 11, 0

I BEAM S₁S₂ MODAL, PLISAFREQ_RESP NOVEMBER 25, 1977 NASTRAN 9/16/74 PAGE 2
CJAR ELEMENTS

CARD COUNT	CASE CONTROL DECK ECHO
1	JTITLE=J-AM-S ₁ S ₂ MODAL, PLISAFREQ_RESP
2	SUBTITLE= CJAR ELEMENTS
3	LABEL= POINT 13 LOADED
4	MAXLINES=100000
5	SPL=1
6	METHOD=1
7	FREQUENCY=22
8	DAMPING=08
9	RANUOH=33
10	SET 1=5,7,8,9,12
11	DISP(SORT2,PRINT,PHASE)E1
12	ULOAD=7
13	WJTEUJLXPLDII
14	P-OTTER=NASTPLT(0,1)
15	XAXIS=YES
16	YAXIS=YES
17	KLOG=YES
18	YLOG=YES
19	XGRID LINES=YES
20	YGRID LINES=YES
21	XITITLE=FREQUENCY
22	YITITLE=MAGNITUDE
23	ICURVE=THEATA 5 DISP VS FREQUENCY
24	XPLOT,XPRIINT,XPUNCH DISP PSDF /5(R3)
25	JDU=VE=THEATA 7 DISP VS FREQUENCY
26	XPLOT,XPRIINT,XPUNCH DISP PSDF /7(R3)
27	ICURVE=THEATA 8 DISP VS FREQUENCY
28	XPLOT,XPRIINT,XPUNCH DISP PSDF /9(R3)
29	ICURVE=THEATA 9 DISP VS FREQUENCY
30	XPLOT,XPRIINT,XPUNCH DISP PSDF /3(R3)
31	ICURVE=THEATA 12 DISP VS FREQUENCY
32	XPLOT,XPRIINT,XPUNCH DISP PSDF /12(R3)
33	ICURVE=VERTICAL 5 DISP VS FREQUENCY
34	XPLOT,XPRIINT,XPUNCH DISP PSDF /5(T2)
35	ICURVE=VERTICAL 7 DISP VS FREQUENCY
36	XPLOT,XPRIINT,XPUNCH DISP PSDF /7(T2)
37	ICURVE=VERTICAL 8 DISP VS FREQUENCY
38	XPLOT,XPRIINT,XPUNCH DISP PSDF /8(T2)
39	ICURVE=VERTICAL 9 DISP VS FREQUENCY
40	XPLOT,XPRIINT,XPUNCH DISP PSDF /3(T2)
41	ICURVE=VERTICAL 12 DISP VS FREQUENCY
42	XPLOT,XPRIINT,XPUNCH DISP PSDF /12(T2)
43	BEGIN BULK

USER INFORMATION MESSAGE 207. BULK DATA NOT SORTED, XSORT WILL RE-ORDER DECK.

TABLE C2. INPUT-OUTPUT CONTROL

I-BEAM-SYS, MODAL, PLIS, FREQ, RESP NOVEMBER 25, 1977 NASTRAN 9/16/74 PAGE 3
C9AR ELEMENTS

POINT 13 LOADED

SORTED BULK DATA ECHO

CARD COUNT	1	2	3	4	5	6	7	8	9	10
1-	C9AR	1	1	2	1.0	0	1.0	1		
2-	CBAR	2	1	2	3	1.0	0	1.0	1	
3-	CBAR	3	1	3	4	1.0	0	1.0	1	
4-	CBAR	4	1	4	5	1.0	0	1.0	1	
5-	CBAR	5	1	5	6	1.0	0	1.0	1	
6-	CBAR	6	1	6	7	1.0	0	1.0	1	
7-	CBAR	7	1	7	8	1.0	0	1.0	1	
8-	CBAR	8	1	8	9	1.0	0	1.0	1	
9-	CBAR	9	1	9	10	1.0	0	1.0	1	
10-	CBAR	10	1	10	11	1.0	0	1.0	1	
11-	CBAR	11	1	11	12	1.0	0	1.0	1	
12-	CBAR	12	1	12	13	1.0	0	1.0	1	
13-	CBAR	13	1	13	14	1.0	0	1.0	1	
14-	CBAR	14	1	14	15	1.0	0	1.0	1	
15-	CBAR	15	1	15	16	1.0	0	1.0	1	
16-	MASS2	1	.002034	9	2					
17-	MASS2	2	.003051	7	2					
18-	DATA	8	9	2	1.0					
19-	LOAD	66	1.0	1.0	7					
20-	EIG	41	GIV							
21-	EIG	MAX								1.0E-8 +EIG
22-	FREQ	22	40.0	3200.0	100					
23-	GRID	1	0	0	0					
24-	GRID	2	6.0	0	0					
25-	GRID	3	12.0	0	0					
26-	GRID	4	18.0	0	0					
27-	GRID	5	19.0	0	0					
28-	GRID	6	24.0	0	0					
29-	GRID	7	27.0	0	0					
30-	GRID	8	32.0	0	0					
31-	GRID	9	36.0	0	0					
32-	GRID	10	42.0	0	0					
33-	GRID	11	48.0	0	0					
34-	GRID	12	50.0	0	0					
35-	GRID	13	54.0	0	0					
36-	GRID	14	60.0	0	0					
37-	GRID	15	66.0	0	0					
38-	GRID	16	72.0	0	0					
39-	GRID	17	10.E+6	4.E+6	.00340					
40-	PARAM	COUPMASS1								
41-	PARAM	LMODES	7							
42-	PBAR	1	1.244	.357	1.835					
43-	RAJDPS	99	1	1.48996E-0	.77					
44-	LOAD1	7								
45-	SPC1	2	1.345	1	THRU	10				
46-	SPC1	3	2	1	16					
47-	SPCADD	1								
48-	TADMP1	88								
49-	DAMP	40.0	.0248	76.92	.0748	265.0	.0279	1302.0	.0430	.4DAMP
50-	DAMP1	1421.0	.00107	3200.0	.00107	ENOT				.4DAMP1

TABLE C3. I-BEAM MODEL PARAMETERS

AD-A066 141

AIR FORCE FLIGHT DYNAMICS LAB WRIGHT-PATTERSON AFB OHIO F/G 1/3
PREDICTION OF THE ANGULAR RESPONSE POWER SPECTRAL DENSITY OF AI--ETC(U)
DEC 78 J H LEE, M W OBAL, D L BROWN

UNCLASSIFIED

AFFDL-TR-78-188

NL

2 OF 2

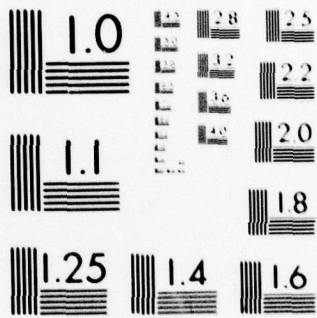
AD
A0661-1



END
DATE
FILMED

5-79

DDC



MICROCOPY RESOLUTION TEST CHART
NATIONAL BUREAU OF STANDARDS-1963-A

THIS PAGE IS BEST QUALITY PRACTICABLE
FROM COPY FURNISHED TO DDC

THIS PAGE IS BEST QUALITY PRACTICABLE
FROM COPY FURNISHED TO DDC

I BEAM S.S. MODAL PLISAFREQ RESP
CBAR ELEMENTS

NOVEMBER 25, 1977 NASTRAN 9/16/74 PAGE

POINT 13 LOADED

SORTED BULK DATA ECHO

CARD	1	2	3	4	5	6	7	8	9	10
COUNT	1.0	1.0	3200.0	1.0	3201.0	0.0	ENDT			
51-	IABE-D1 10									↑IAB
52-	↑IAB 40.0	.263E-07	41.8	.190E-07	43.7	.118E-07	45.6	.728E-08	↑IAB	
53-	IABND1 77									
54-	↑IAB 40.0	.411E-08	49.8	.228E-08	52.0	.113E-08	54.4	.417E-08	↑IAB	
55-	↑IAB 47.7	.470E-09	9.3	.138E-08	62.0	.212E-08	64.8	.281E-08	↑IAB	
56-	↑IAB 56.8	.237E-08	70.7	.317E-08	73.9	.936E-08	77.2	.725E-08	↑IAB	
57-	↑IAB 67.7	.856E-08	84.3	.916E-08	88.0	.930E-08	92.0	.916E-08	↑IAB	
58-	↑IAB 80.6	.842E-08	100.4	.100E-07	104.9	.136E-07	109.6	.153E-07	↑IAB	
59-	↑IAB 96.1	.141E-07	119.6	.134E-07	125.0	.117E-07	130.6	.161E-07	↑IAB	
60-	↑IAB 114.5	.201E-07	142.5	.184E-07	148.9	.179E-07	155.8	.205E-07	↑IAB	
61-	↑IAB 136.4	.200E-07	169.9	.187E-07	177.5	.175E-07	185.4	.182E-07	↑IAB	
62-	↑IAB 162.6	.230E-07	202.4	.222E-07	211.5	.249E-07	220.3	.260E-07	↑IAB	
63-	↑IAB 193.7	.335E-07	241.2	.373E-07	252.0	.230E-07	263.3	.320E-07	↑IAB	
64-	↑IAB 230.8	.340E-07	287.4	.409E-07	300.2	.268E-07	313.7	.778E-07	↑IAB	
65-	↑IAB 275.1	.855E-07	342.4	.142E-06	357.8	.271E-06	373.8	.503E-05	↑IAB	
66-	↑IAB 327.8	.748E-05	408.8	.235E-06	426.3	.714E-07	445.4	.202E-07	↑IAB	
67-	↑IAB 390.5	.823E-08	486.2	.195E-08	508.0	.335E-09	530.7	.398E-10	↑IAB	
68-	↑IAB 465.4	.120E-09	579.4	.548E-09	603.3	.931E-09	632.4	.194E-08	↑IAB	
69-	↑IAB 554.5	.188E-08	690.3	.271E-08	721.3	.373E-08	753.0	.299E-08	↑IAB	
70-	↑IAB 660.8	.429E-08	822.6	.530E-08	859.5	.938E-08	898.0	.146E-07	↑IAB	
71-	↑IAB 787.3	.360E-08	960.2	.441E-08	1024.1	.740E-08	1070.0	.107E-07	↑IAB	
72-	↑IAB 938.2	.271E-07	1163.0	.578E-07	1220.3	.335E-05	1275.0	.542E-07	↑IAB	
73-	↑IAB 1117.9	.566E-08	1391.8	.615E-09	1454.1	.310E-10	1519.2	.397E-10	↑IAB	
74-	↑IAB 1332.1	.285E-09	1653.4	.436E-09	1732.7	.612E-09	1810.3	.106E-08	↑IAB	
75-	↑IAB 1587.1	.980E-09	1978.1	.159E-08	2064.6	.229E-08	2157.1	.281E-08	↑IAB	
76-	↑IAB 2253.7	.166E-08	2354.7	.419E-08	2460.2	.346E-08	2571.4	.151E-05	↑IAB	
77-	↑IAB 2685.5	.186E-08	2805.9	.433E-11	2931.5	.737E-10	3062.8	.140E-09	↑IAB	
78-	↑IAB 3210.0	.214E-09	ENDI							
79-	ENDDATA									

NO ERRORS FOUND - EXECUTE NASTRAN PROGRAM

TABLE C4. FORCING POWER SPECTRAL DENSITY FUNCTION INPUT

To test the accuracy of a NASTRAN model for the experimental beam, the first six resonance frequencies are compared with the experimental values in Table C5, which shows good agreement between them.

Mode No.	NASTRAN	Experimental
1	55.52	58.54
2	243.36	253.90
3	536.95	449.21
4	939.50	1044.92
5	1478.70	1503.90
6	2207.60	2109.37

Table C5. Comparison of the NASTRAN and experimental resonance frequencies.